The Dissertation Committee for Matthew Evan Thrasher
certifies that this is the approved version of the following dissertation:

Geometry and dynamics of fluid-fluid interfaces

Committee:

Harry L. Swinney, Supervisor

Graham Carey

E. L. Florin

Larry Lake

Mark B. Mineev-Weinstein

Jack Swift

Geometry and dynamics of fluid-fluid interfaces

by

Matthew Evan Thrasher, B.A., M.A.

DISSERTATION

Presented to the Faculty of the Graduate School of

The University of Texas at Austin

in Partial Fulfillment

of the Requirements

for the Degree of

DOCTOR OF PHILOSOPHY

THE UNIVERSITY OF TEXAS AT AUSTIN

December 2007

For my mother, Cheryl.

The men bound the big logs first
with new hemp and, like ants, trundled them to a cliff
to plunge through tall nettles. The logs gathered thirst

for the sea which their own vined bodies were born with.
Now the trunks in eagerness to become canoes
ploughed into breakers of bushes, making raw holes

of boulders, feeling not death inside them, but use –
to roof the sea, to be hulls.

from *Omeros*, Derek Walcott

Acknowledgments

Harry Swinney guided me with his energetic spirit of investigation, prudence, and committed support. I learned and benefitted from his charity, storytelling, and hard work. He is a model advisor and I am a physicist because of him. Mark Mineev-Weinstein taught me to balance thought and soul. I am especially grateful for his vitality and his counsel.

I dearly value meeting so many good men and women during my time in graduate school. With fondness I remember conversations with Hepeng Zhang, Matthias Schroeter, Sunghwan Jung, and Memi Be'er. I credit years of work to those who built the experimental apparatus, advised and taught me, collected data that I used, and worked with me: Mickey Moore, Eran Sharon, Olivier Praud, W.M. McCormick, Jack Swift, E.L. Florin, Itamar Procaccia, and Joachim Mathiesen. I could not have completed a single project without the collaborative efforts of Alex Leshchiner, Sunghwan Jung, Leif Ristoph, Yee Kwong Pang, Brooks Campbell, and Chih-Piao Chuu. I am indebted to Paul Umbanhowar, who has honestly encouraged and guided me since he hosted me at UT when I was as a high school student. I would also like to thank Larry Lake and Graham Carey for their advice and watchful attention of my progress. I want to thank Olga Vera and Elena Simmons for their friendship, support, and daily assistance with managing the necessary details. Thanks to

Pinyu Wu for proofreading this dissertation.

For good humor and companionship I want to thank Robert Deegan, Ben King, Martin Kochanczyk, Jenn Kreft, Matt Lane, Paul Petersan, Erin Rericha, Bruce Rodenborn, Jori Ruppert-Felsot, and the many other members of the Center for Nonlinear Dynamics. I extend most sincere warmth and love to my family and friends: Cheryl, Blake, James, Michelle, Chris Guo, Katie Hinko, Alex Leshchiner, Brad Ortloff, Rory Rother, Aaron Snead, Tracy Wright, Pinyu Wu, Angela Chen Yarbrough, and Abe Yarbrough.

Acknowledgment is made to the Donors of the American Chemical Society Petroleum Research Fund for support of the pinch-off and the harmonic moments projects under the grant "Harmonic Moments of Viscous Fingering Structures in Thin Oil Layers." The fjords and harmonic measure research was supported by the Office of Naval Research Grant N00014-04-1-0282, the Office of Naval Research Quantum Optics Initiative Grant N00014-03-1-0639, and by the Los Alamos National Laboratory LDRD Grant "Unstable fluid/fluid interfaces."

Matthew Evan Thrasher

Center for Nonlinear Dynamics
The University of Texas at Austin
December 2007

Geometry and dynamics of fluid-fluid interfaces

Publication No. _____

Matthew Evan Thrasher, Ph.D.
The University of Texas at Austin, 2007

Supervisor: Harry L. Swinney

We observed the evolution of unstable fluid interfaces in experiments on viscous fingering, pinch-off, and bouncing jets. If we can first identify classes of universal behavior, then we can begin building a unified framework to understand nonlinear processes.

We performed the first experimental test of the harmonic moments of viscous fingering patterns, grown by injecting air into a thin layer of silicone oil, which was confined between two closely spaced plates, called a Hele-Shaw cell. We observed that the predicted decay of the moments was accurate within our measurement uncertainty, which confirmed the predicted conservation of the moments for zero surface tension. With greater forcing, the air bubble will undergo a secondary tip-splitting instability, where the fingers of air fork into two or more fingers. We discovered two selection rules for the changing base width and the nearly invariant opening angle of fjords, which are the regions of oil between the fingers of air. We then compared our experiments

on viscous fingering with diffusion-limited aggregation (DLA), a model of unstable growth. We calculated that DLA and viscous fingering have the same spectrum of singularities [called $f(\alpha)$] within measurement uncertainty. Since the spectrum is a global encapsulation of the growth dynamics and scaling properties, we say that the two processes are in the same scaling universality class. All of these results for viscous fingering are expected to apply to other physical systems which approximate Laplacian growth, a model of an interface where its growth rate is determined by the local gradient of a field ϕ obeying Laplace's equation $\nabla^2\phi = 0$.

Next we present preliminary work on the experimental test of two predictions for flows in Hele-Shaw cells: 1) soliton-like behavior of two viscous domains and 2) self-similar, universal pinch-off of an inviscid bubble in a viscous liquid. Finally, we report our observations and analysis of a liquid stream with constant viscosity (i.e. Newtonian) which rebounds from the free surface of a moving bath. The stream bounces on a thin layer of lubricating air which is replenished by the relative motion of the jet and the bath.

Table of Contents

Chapter 1

Introduction

This dissertation presents experiments on five interfacial phenomena: the geometry of fjords in viscous fingering, the singularity spectrum of viscous fingering and diffusion-limited aggregation (DLA), the evolution of the harmonic moments of viscous fingering, non-capillary pinch-off of bubbles, and the rebound of a viscous jet from a moving free surface.

The dissertation is based on work which has already been published in four papers [86, 118, 136, 137] and Chapter 4 is based on a fifth paper which is forthcoming. Because the published papers are readily available online, the papers are not reprinted here. Instead the dissertation covers additional material not in the papers, such as background material, experimental details, additional results, and discussion of the relevance of the five phenomena.

1.1 Overview of viscous fingering

Viscous fingering is an interfacial instability that occurs during the displacement of a viscous fluid by a less viscous fluid. Initially small disturbances on the interface that penetrate farther into the viscous fluid than the surrounding interface will grow faster than the surrounding interface. These

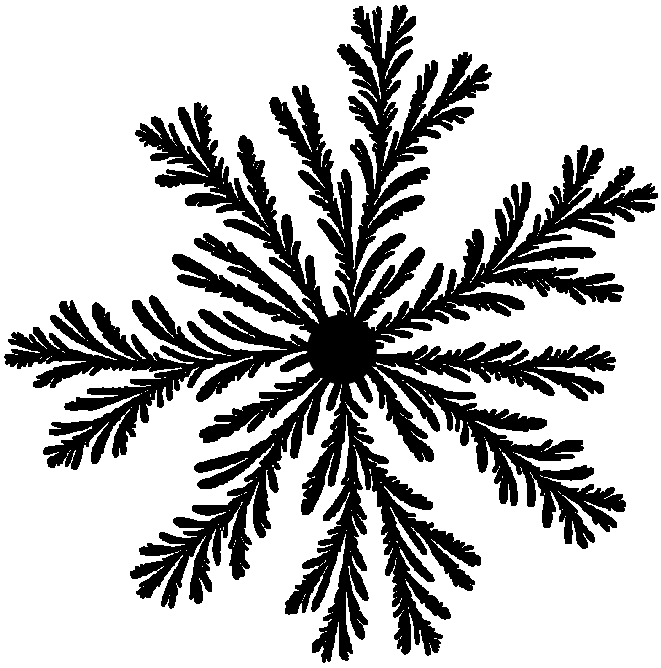

Figure 1.1: A ramified viscous fingering pattern grown in our experiments. Air is the black domain, viscous oil is the white exterior domain. The diameter of the pattern is 22 cm. The central black circle is not the air bubble, but rather an artefact from the interface extraction algorithm (see Sect.3.2). Reprinted with permission from Mathiesen, Procaccia, Swinney, and Thrasher [86].

disturbances are amplified to fingers that penetrate into the viscous fluid. A growing finger can undergo a second instability where the tip of the finger divides into two or more fingers. This tip-splitting instability can repeat to create very ornate and complicated interfacial patterns, such as in Fig. 1.1.

Since its discovery in 1958 by Saffman and Taylor [121], there have been over 700 papers published on viscous fingering. There have also been many successes in explaining the different aspects of the problem [120]. For a

survey of different experiments and an introduction to the basic mathematics of viscous fingering, see [28]. There are many variations on viscous fingering experiments. The less viscous fluid can be driven into the more viscous fluid by injection or suction [102]. The interface of the two fluids can be perpendicular or parallel to the flow [151]. The flow can happen within a porous media or a Hele-Shaw cell [57, 77]. The two fluids can be miscible or immiscible [57, 107, 145]. The experiment can be contained by different geometries, such as the rectangular [121], radial (Fig. 1.1) [102], sector [134], conical [95], spherical [100], and cylindrical geometries. The two fluids can be Newtonian liquids [121], non-Newtonian liquids [78], liquid crystals [18, 19], polymers [79, 153], liquid He [46, 155], or reactive fluids [154]. Experiments can be done with or without surfactants [79]. A variety of other parameters can be introduced, such as rotation [22], gravity [57, 87], bubbles [87], etched grids [66], wires [87], anisotropy [10], magnetic fields [44], substrate wetting effects [3], and many others [87]. In addition, there is an extensive literature of mathematics and theoretical physics that pertains to viscous fingering, such as problems in electronic physics [2], string theory [76], conformal mapping [11, 132], and integrable mathematics [68, 93].

Viscous fingering belongs to a larger class of problems called isotropic Laplacian growth, which is discussed in Chapter 4. Laplacian growth is applicable to a variety of physical situations, such as solidification [139], electrodeposition [80], bacterial colony growth [146], flame propagation [154], dielectric breakdown (e.g. lightning, streamers, and sparks) [36], ionization fronts [90],

doublets in directional solidification [67, 82], underground hydrogen storage [103], drying water films [123], viscous sintering [30, 58, 70], and oil production [71].

Viscous fingering occurs during secondary and enhanced oil recovery [71]. Underground oil is pumped out of the ground often with air or water replacing the oil. The interface between the oil and pumping fluid is unstable when the less viscous, more mobile fluid replaces the more viscous, less mobile oil from the porous rock. The less viscous fluids finger into the oil reservoir, and once one reaches the extraction pump, the oil yield drops off quickly. A better understanding of this mechanism that traps oil in porous media could aid in developing procedures to increase the productivity and efficiency of oil recovery from a reservoir. However, there is a large and controversial gap between the real oil recovery procedures and the theoretical descriptions of the physical processes. One step to bridge the two is to experimentally test the assumptions and results of the theoretical literature. In this respect, the Hele-Shaw cell is a useful tool as a laboratory model for porous rock, because both flows are governed by Darcy's law [53] (see Sect.4.1.1).

1.2 Apparatus

We conduct viscous fingering in two Hele-Shaw cells consisting of closely spaced parallel flats; one has a radial geometry and one has a rectangular geometry. These were built by Mitchell Moore and Eran Sharon and modified by Olivier Praud. Details and machine drawings for these cells are available

in Moore's dissertation [96].

Figure 1.2 is a diagram of the rectangular cell with dimensions of 254 cm by 25 cm. The gap thickness was typically 0.0508 cm. For our experiments in this geometry, the mirror was held fast and the camera viewed the center of the channel's length. Silicone oil and air were used as the working fluids. The oil and air buffers equilibrated the pressure along the open edges of the cell. The oil was withdrawn from the oil buffer with a syringe pump to keep the injection rate of air constant. This boundary condition maintained a constant average tip velocity during our experiments. Fluorescent bulbs were positioned behind diffusive translucent plastic and below the rectangular cell to provide uniform lighting for the experiments (Fig. 1.3). The oil-air interfaces were imaged from above with a monochrome camera using a resolution of 1300 by 1030 pixels and a maximum frame rate of 12 frames per second. With this lighting, the interface was a dark line on a bright background because of the refraction of the interface.

Figure 1.4 is a drawing of radial cell with a diameter of 30 cm. It essentially consists of two 6 cm thick telescope blanks separated by metal shims, typically 0.0127 cm thick. The glass plates were clamped between an aluminum vessel and an acrylic top plate. The aluminum vessel also served as the container for the oil reservoir, which surrounds the plates and equilibrates the pressure around the edge of the gap. A hole is drilled through the bottom plate to allow the injection and withdrawal of fluid between the plates. Other inlets were located in the reservoir at halfway up the height of the reservoir

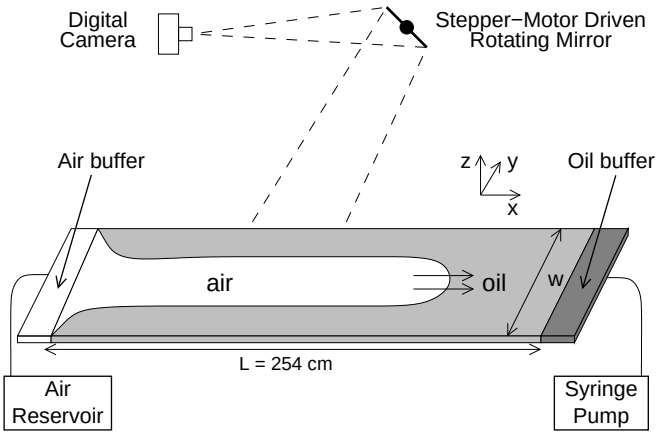

Figure 1.2: An overview of the rectangular Hele-Shaw cell. Reprinted from the dissertation of Mitchell Moore [96].

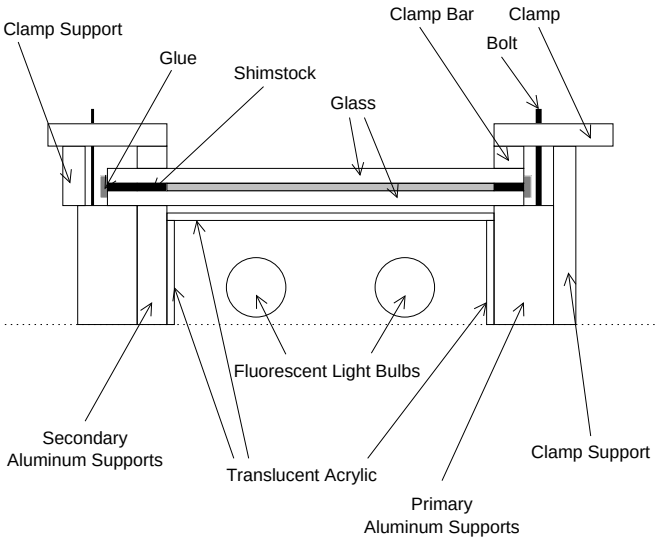

Figure 1.3: A cross-section of the rectangular Hele-Shaw cell. Reprinted from the dissertation of Mitchell Moore [96].

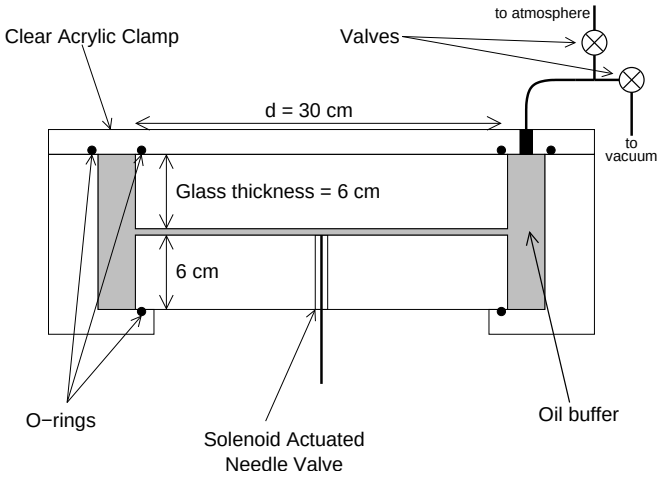

Figure 1.4: A cross-section of the radial Hele-Shaw cell. Reprinted from the dissertation of Mitchell Moore [96].

(not shown in Fig. 1.4) and at the top of the reservoir.

An array of circular fluorescent bulbs were positioned above the radial cell and provided lighting for the experiments. To make the illumination uniform, a tall cylinder of translucent plastic covered the experiment (Fig. 1.5). The cylinder has a hole in the very top for a camera to view the cell. Two cylinders were made by Moore and Sharon, one with a large diameter and a large hole for the camera and one with a smaller diameter and a smaller hole for the camera. The larger hole allowed for more flexibility in positioning the camera, while the smaller hole cast a smaller shadow onto the middle of the cell.

A third Hele-Shaw cell with a square geometry and four inlets was used in pinch-off experiments. It was designed by Brooks Campbell and me and

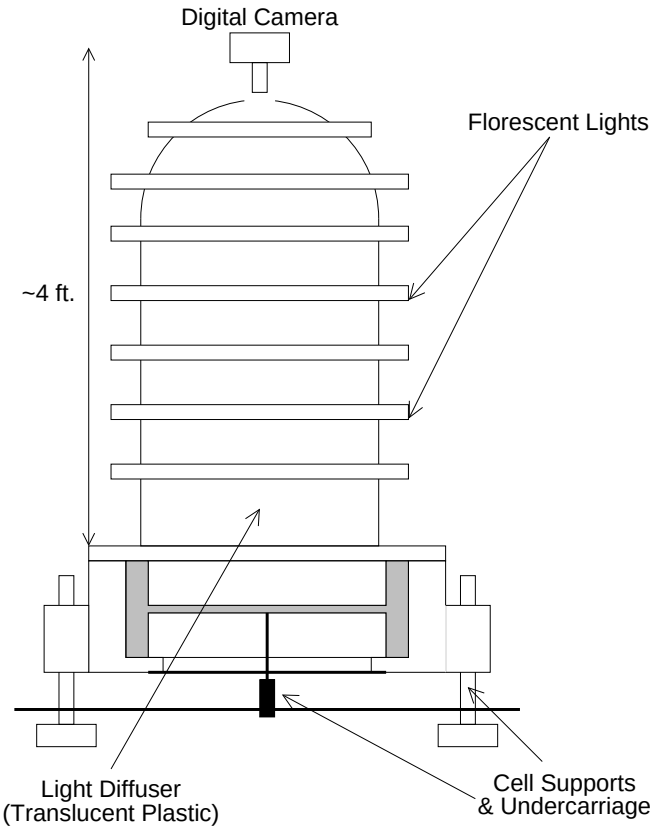

Figure 1.5: An overview of the radial Hele-Shaw cell with the lighting and plastic cylinder in place. Reprinted from the dissertation of Mitchell Moore [96].

was built by Brooks. The square cell is described in Sect. 5.2.

1.3 Fjords in viscous fingering

We describe our experiments on viscous fingering of air into oil contained in the radial and rectangular geometry. We concentrated on the fjords of oil that separate fingers of air (Chapter 2).[1] The experiments were motivated by theoretical work on zero surface tension Laplacian growth, which identified the fjords as the fundamental unit of solutions for this highly unstable, nonlinear problem. Two robust selection rules were found for the properties of fjords: their changing widths and their invariant opening angles. Mark Mineev-Weinstein developed the theory. Leif Ristroph and I conducted the experiments. Leif wrote a undergraduate honor thesis with Harry Swinney [117], which we used as the basis for our paper [118].

1.4 Harmonic measure of viscous fingering and diffusion limited aggregation

Viscous fingering and diffusion-limited aggregation (DLA) are nonlinear growth processes in a radial geometry that produce visually similar fractals patterns. Since it is best not to trust our intuition in these often counter-intuitive systems, we are interested in whether the visual similarity can be

[1]This section and Chapter 2 are based on an article in *Physical Review E* titled "Fjords in viscous fingering: selection of width and opening angle" written by Leif Ristroph, me, Mark Mineev-Weinstein, and Harry L. Swinney [118]. The paper can be downloaded from `http://link.aps.org/abstract/PRE/v74/e015201`.

confirmed quantitatively in a way that will address whether or not the physical mechanisms of growth are also similar (Chapter 3). Some have argued that because the viscous fingering interface grows in parallel and the DLA cluster grows serially, the two patterns should have fundamentally different properties [6]. Using data previously collected by Olivier Praud and his modifications to the radial cell, I grew more fractal viscous fingering patterns. Mathiesen and Proccacia measured the patterns' harmonic measures (probabilities or velocities of growth for each point on the interface), fractal dimensions, and singularity spectra by constructing conformal maps of the final stage of growth. This analysis resulted in strong evidence that the two growth patterns have the same global geometric properties.[2]

1.5 Harmonic moments of viscous fingering

S. Richardson predicted that there are an infinite number of conserved quantities for Laplacian growth with zero surface tension [94, 114]. Those conserved quantities are harmonic moments, which are integrals over the viscous domain of integer powers of $z = x + iy$, where x and y are Cartesian coordinates in the complex plane. The harmonic moments are also called analytic moments in other literature. The harmonic moments yield a special decomposition of the potential field that is time invariant for the zero surface tension

[2]This section and Chapter 3 are based on a paper in *Europhysics Letters* entitled "The Universality Class of Diffusion Limited Aggregation and Viscous Fingering" written by Joachim Mathiesen, Itamar Procaccia, Harry L. Swinney, and me [86]. It can be downloaded from `http://chaos.utexas.edu/manuscripts/1161977332.pdf`.

problem. The time invariance has not yet been observed in experiments. Our collaborator, Mark Mineev-Weinstein, has extended the theory of harmonic moments to include the effect of surface tension (Chapter 4). He has calculated that the harmonic moments should decay at a rate which depends on the shape of the interface. This powerful technique describes the dynamics of the shape completely.

If we use viscous fingering as an example of Laplacian growth, this law of motion for a viscous domain can be tested by tracking the interface evolution of viscous fingering patterns in a Hele-Shaw cell.[3] This requires accounting for the oil wetting the plates of the Hele-Shaw cell and measuring the velocities of each piece of each interface. After Alex Leshchiner, Harry Swinney, and I conducted the experiments and analyzed the data, we successfully confirmed Mark Mineev-Weinstein's theory. This work determined that the harmonic moment description of viscous fingering growth is physically realizable, robust, and powerful.

The point of common interest is that the complicated nonlinear dynamics in growth problems are difficult to describe and predict because of their instabilities and singularities. Our method can describe the full dynamics and predict the instantaneous change in moments given an interface with negligible wetting. We used viscous fingering as a scenario to demonstrate the validity of

[3]This section and Chapter 4 are based on work that is in preparation as "Harmonic moment dynamics in Laplacian growth" to be submitted to *Physical Review E*. The work is being written by Alexander Leshchiner, me, Mark B. Mineev-Weinstein, and Harry L. Swinney.

the technique (a proof of principle) to completely describe a growth problem. The law of dynamics for harmonic moments could also be applied to Laplacian growth processes other than viscous fingering.

1.6 Pinch-off in a Hele-Shaw cell

In Chapter 5, we present our attempts to test two predictions from the theoretical work on pinch-off problems.[4] First, S. Richardson predicted that after an expanding annulus of viscous liquid merges with a stationary liquid drop, an identical drop will be deposited in the same place after the annulus moves past the original location of the drop (Sect. 5.4) [116]. He calculated that the viscous domains could pass through each other and that their final shapes would not change if certain criteria are met. Second, Lee *et al.* predicted that without surface tension an inviscid bubble surrounded by a viscous liquid breaks into two bubbles in a manner such that the shape of the interface near the breaking point is self-similar and universal (Sect. 5.3) [76].

Brooks Campbell built an experimental apparatus with only design help from me, and he conducted experiments designed to test these predictions (Sect. 5.2). These tests were motivated by the connections that would open between physics and a large literature of existing theory, which has not been verified experimentally. Moreover these tests can provide useful understanding for applications to the extraction of oil from underground reservoirs, which is

[4]This section and Chapter 5 is based on work with Brooks Campbell. His thesis can be downloaded from `http://chaos.utexas.edu/manuscripts/1196733333.pdf`.

an industrial problem of great power and effect (Sect. 5.3 and 5.4). Pinch-off occurs during the recovery of oil from wells. If the predicted phenomena exist, another possible mechanism responsible for the trapping of oil in porous rock will be observed.

1.7 Bouncing jet

The collision of two fluid bodies most commonly results in the two bodies merging together. However, I discovered that a falling viscous liquid stream can bounce off the free surface of a bath of the same liquid if the bath is moving horizontally with respect to the falling stream (Chapter 6).[5] A good introduction to the bouncing jet phenomenon is [137]. Movies of the phenomena are available at `http://pof.aip.org/pof/gallery/2007toc.jsp`.

Similar falling streams have been seen to bounce off a bath but only with non-Newtonian liquids (i.e. for fluids with viscosities that depend on shear rate) [64, 142], while the phenomenon we report occurs for Newtonian liquids. Sunghwan Jung, Yee Kwong Pang, Chih-Piao Chuu, Harry Swinney and I used silicone oil in our experiments; mineral oil and cooking oil also

[5]This section is based on my previously published paper "Bouncing of a jet off a Newtonian liquid surface" *Phys. Fluids* **19**, 091110 (2007) written with Sunghwan Jung and Yee Kwong Pang and Harry L. Swinney [137]. This paper can be downloaded from `http://link.aip.org/link/?PHFLE6/19/091110/1`. I have also published an article "Bouncing jet: A Newtonian liquid rebounding off a free surface" with Sunghwan Jung, Yee Kwong Pang, Chih-Piao Chuu, and Harry L. Swinney in *Physical Review E* [136]. This paper can be downloaded from `http://link.aps.org/abstract/PRE/v76/e056319`. In 2005, I wrote a Master's thesis on the bouncing jet "A Liquid Stream Bouncing off a Moving Liquid Bath [135]." This thesis can be downloaded from `http://chaos.utexas.edu/manuscripts/1193518381.pdf`.

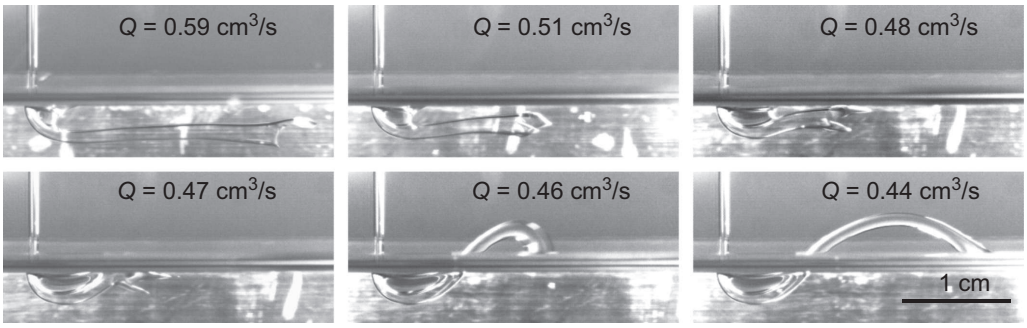

Figure 1.6: Jet bouncing spontaneously as the flow rate Q rapidly decreases. Conditions: $\mu = 361$ mPa s, $H = 4.2$ cm, and $V_{bath} = 5.2$ cm/s. The relative times of each image are 0, 0.46, 0.66, 0.71, 0.82, and 0.90 s. The white splotches below the surface are bright reflections from the aluminum background. Reprinted with permission from Thrasher, Jung, Pang, and Swinney [137].

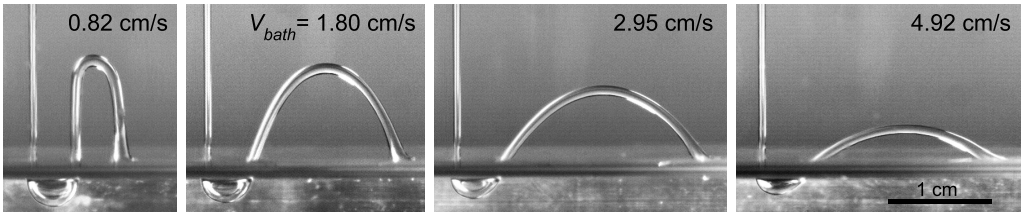

Figure 1.7: Jet's dependence on bath velocity V_{bath}. Conditions: $\mu = 361$ mPa s, $Q = 0.24$ cm^3/s, and $H = 4.2$ cm. Reprinted with permission from Thrasher, Jung, Pang, and Swinney [137].

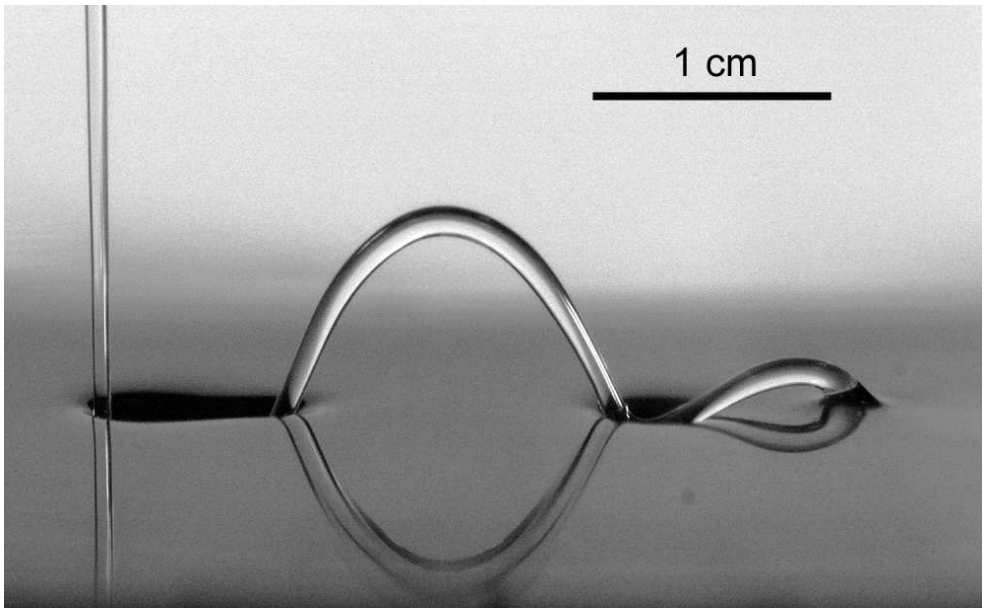

Figure 1.8: Double bouncing jet. Conditions: $\mu = 106$ mPa s, $Q = 0.35$ cm^3/s, $H = 5.0$ cm, and $V_{bath} = 15.7$ cm/s. Picture taken by me. Reprinted with permission from Thrasher, Jung, Pang, and Swinney [137].

bounce. The enabling mechanism for the bouncing is a thin, lubricating layer of air that separates the bouncing jet from the bath. The shear between the jet and the bath replenishes the film of air. The jet and the bath do not mix while bouncing, and the bouncing jet can be unsteady and stable. In Figs. 1.6 to 1.8, a stream of silicone oil with a flow rate Q and a viscosity μ falls from height H to a bath of the same liquid, which is moving to the right with velocity V_{bath}. Figure 1.6 shows a stream spontaneously begin to bounce after a decrease in the flow rate. The fluid above and below the surface is visible with the surface being the dark, horizontal line. Before the jet bounces, it entrains a cylindrical film of air into the bath. The contrast in the image is provided by the refraction at the surfaces of the air film. As the flow rate decreases, the length of the entrained film decreases until the jet bounces. Figure 1.7 shows a nearly vertical rebound at a small bath velocity and more oblique rebound at a larger bath velocity. Figure 1.8 shows a jet bouncing twice. Liquid streams are able to bounce in a broad range of experimental parameters. This makes the experiment simple to reproduce at home by pouring mineral oil into a pan of mineral oil.

Chapter 2

Selection rules for fjord geometry

The first selection rule for viscous fingering was reported by Saffman and Taylor in 1958 [121]. In their experiments, a channel consisting of two horizontal plates was filled with a viscous oil and then air was injected between the plates. In this way, a viscous finger was grown in a Hele-Saw cell. At very low injection rates, the finger was almost the entire width of the channel; nearly all the oil was replaced by air. As the injection rate increased, the width of the finger decreased. Asymptotically, the width of the finger approached about one-half of the channel width. Saffman and Taylor carried out a complementary analysis to attempt to explain why the width was one-half. Making several approximations, they arrived at a family of curves for the finger shape with a continuous parameter for the finger width relative to the channel width ranging from 0 to 1. One of the curves was the asymptotic shape observed in experiment, but they didn't know why it was that particular curve. This proved to be a difficult problem; it was twenty-three years until Saffman and McLean used computations to isolate that it was the introduction of surface tension, taken to be zero in the original Saffman-Taylor analysis, that selected for the one-half width [88]. Another ten years of detailed studies confirmed this result theoretically [126].

This chapter reports the search and discovery of two more selection rules. The new rules are simple, applicable to nearly every viscous fingering pattern, and can be tested in many other systems.

2.1 Geometric selection rules

Selection is a recurring theme in the study of the growth of interfaces in nonlinear pattern formation. Selection arises when a physical situation is represented by a set of simplified growth equations and several different solutions exist where in experiments only one of the solutions is observed. Why is this one solution observed, while the other, equally plausible solutions are not? The influence that breaks this degeneracy is called the selection rule. For instance, electromagnetic dipole transitions follow a set of selection rules, which conserve angular momentum [122]. Phonons in crystals obey a set of selection rules because of symmetry [105]. There are selection rules for nuclear spin transitions [140] and the size distribution function of the minority phase in two-phase mixtures (Ostwald ripening) [89]. We can ask, "Why does plant growth often exhibit numbers from the Fibonacci sequence?" But we do not mean to imply that nature has a choice. Instead in our simplifications we have overlooked a crucial piece. Usually this rule comes from the wavelength of the fastest growing mode, the conservation of some relevant physical quantity, a minimization of an energy, a maximization of a relevant quantity (such as density), a principle of least action, or a stability criterion, such as in the parabolic tip of solidification [14, 74].

Some selection rules are rigid, while others are only rules of thumb. For example in simulations and analysis, the effects of surface tension cause a finger of half-width to be chosen from fingers of all widths, but in experiments of increasing injection rate, the observed width overshoots the half-width solution to about 0.43 of the channel width, because of another factor: the wetting film left on the plates [131].

We are concerned with selection rules that dictate how shapes develop during viscous fingering. Specifically, we searched for selection rules not in the well studied fingers but in the less studied fjords (Fig. 2.1). Fingers are the intrusions of less viscous fluid into the more viscous fluid, and fjords are the complementary strips of more viscous fluid left behind the growing front. Of the hundreds of papers on viscous fingering, only a few address fjords. The fjords can be seen as fingers of the more viscous liquid. These features are named after the flooded, glacial valleys in Norway that are long, narrow inlets of water with steep walls.

Two selection rules were found for the fjords. The fjord base width was measured to be one-half of the most unstable wavelength on the growing interface. This selection rule was predicted and explained. The fjord's opening angle was measured to be $8.0^\circ \pm 1.0^\circ$ for a wide range of experimental conditions. This was unexpected and is a challenge for theoretical physics as no explanation has been found so far. This research appears as "Fjords in viscous fingering: selection of width and opening angle" in *Physical Review E* [118]. The paper can be downloaded from `http://link.aps.org/abstract/`

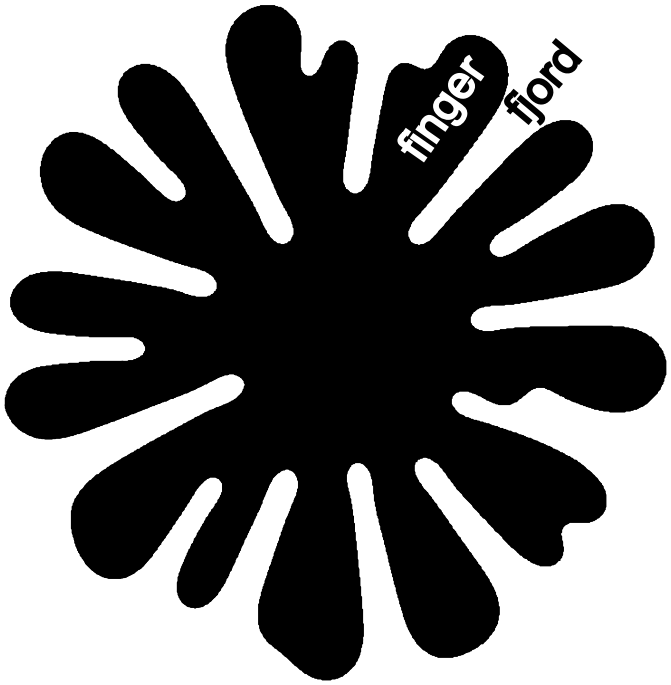

Figure 2.1: A finger and a fjord is labeled on a viscous fingering pattern grown at low forcing in our radial Hele-Shaw cell. Air is the black domain, viscous oil is the white exterior domain. The diameter of the pattern is 18 cm.

PRE/v74/e015201.[1]

2.2 Relevance

These selection rules are the first to be reported for viscous fingering patterns since Saffman and Taylor's original paper in 1958 [121]. They are simple, counter-intuitive, and hold for a wide range of parameters. Previous studies have grown ramified patterns but examined different properties, such as the pattern densities and the scaling between different measures [148].

The possible applications of these new selection rules to other growth problems should be explored, especially if the problem can be modeled as Laplacian growth. For example, consider the multibranched structures of a crystal in a material with low anisotropy (Fig. 2.2) and the structures that evolve in a reaction-diffusion system (Fig. 2.3). Our discovery of two new selection rules provides strong motivation for precision experiments and theoretical analyses to characterize a broad variety of systems and to determine similarities and differences in the growth processes.

[1]Leif Ristroph also wrote an undergraduate Honors thesis entitled "Fjord geometry in viscous fingering [117]."

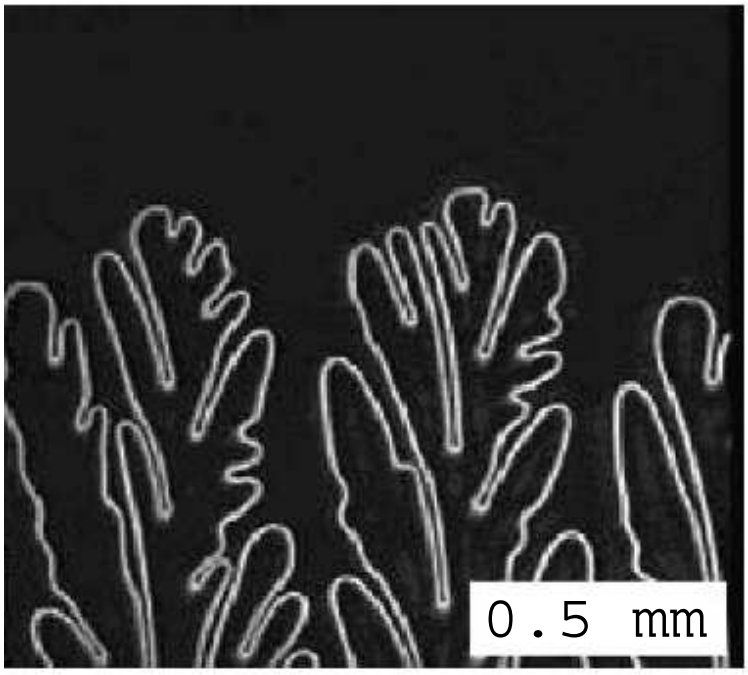

Figure 2.2: Consider the possible opening angle and fjord width for this seaweed structure grown along a crystalline orientation with low surface tension anisotropy. The white line indicates the solid-liquid interface. The solid grows upwards into the undercooled melt. The thermal gradient is 18 K/cm, the concentration is 0.25% succinonitrile-poly(ethylene oxide), and the growth velocity is 2.71 μm/s. Reprinted with permission from Utter and Bodenschatz [138] Fig. 2(b). Copyright 2002 by the American Physical Society.

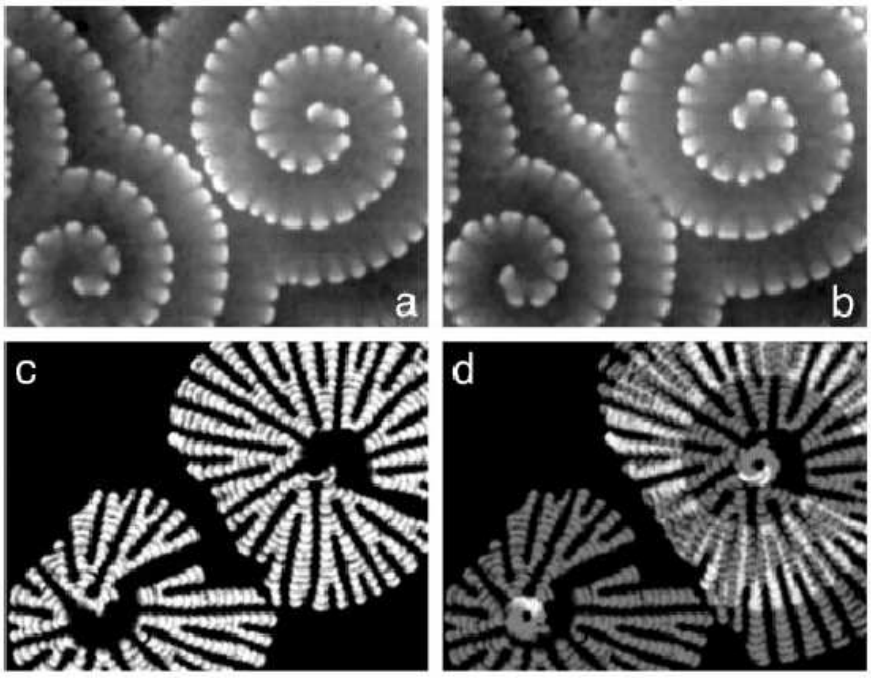

Figure 2.3: Another system to search for corresponding selection rules. Segmented spirals in a BZ-AOT ME. Stroboscopic composites (c and d) show trajectories built from spiral segments (a and b). (c) Superposition of snapshots taken every 50 s of segments of spiral turns initially closest to the cores. (d) Summation of c and trajectories of segments of the second turn of the spiral at the upper right. White corresponds to higher concentration of bathoferriin in (a) and (b), and marks overlapping trajectories in (c) and (d). Frame size 3.72 mm by 4.82 mm. Time between (a) and (b) is 66 s. Reprinted with permission from Vanag and Epstein [141].

Chapter 3

Harmonic measure of viscous fingering and diffusion-limited aggregation

This chapter compares the singularity spectrum of two growth processes: viscous fingering and diffusion-limited aggregation. It is also a demonstration of a computational technique to determine the singularity spectrum for large interfacial patterns. While similar experiments have been conducted before and the analysis technique is not new, the coupling of the powerful analysis tool and the unprecedented scale of the experiments is new. The technique constructs the conformal map from the exterior of the unit circle to the exterior of a highly complex, experimental interface. Most other methods, including the Schwartz-Christoffel transformation [127], cannot match the convergence of our method or the size of patterns that can be analyzed using our method. Many systems produce complex interfaces during their evolution, and this technique could be applied to most of these interfaces.

The details are presented in a previously published paper entitled "The universality class of diffusion limited aggregation and viscous fingering," which appeared in *Europhysics Letters* [86]. This chapter presents background material needed to understand the main points of the paper and some related

preliminary experiments.

3.1 Background

3.1.1 Diffusion-limited aggregation

Diffusion-limited aggregation (DLA) is a simple procedure to assemble a collection of particles. A particle, released far from the origin, undergoes a Brownian walk until it collides with a fixed seed particle at the origin and becomes immobile. In the same way, particles are released one at a time and stick to the growing aggregation, producing a branching, dendritic scaffolding (Fig. 3.1).

Originally this model was created to mimic the condensation of a metal vapor onto a substrate [149], but it also simulates the basic mechanisms of many unstable physical situations, including electrodeposition [69], dielectric breakdown [97], bacterial growth [45], sputter-deposition of thin films [41], and reactive erosion [32]. DLA has also simulated *stable* displacement in porous media by using an anti-DLA process, where random walker annihilates the pattern at the place of sticking [104]. Exact physical analogues of DLA have been proposed, including thin gap electrodeposition [69] and viscous fingering in a Hele-Shaw cell (with the appropriate averaging of the aggregate to smooth the skeletal patterns into continuous interface) [4, 15]. The relationship between DLA and viscous fingering in a Hele-Shaw cell is the subject of this chapter, and several tools for analyzing these patterns are presented next.

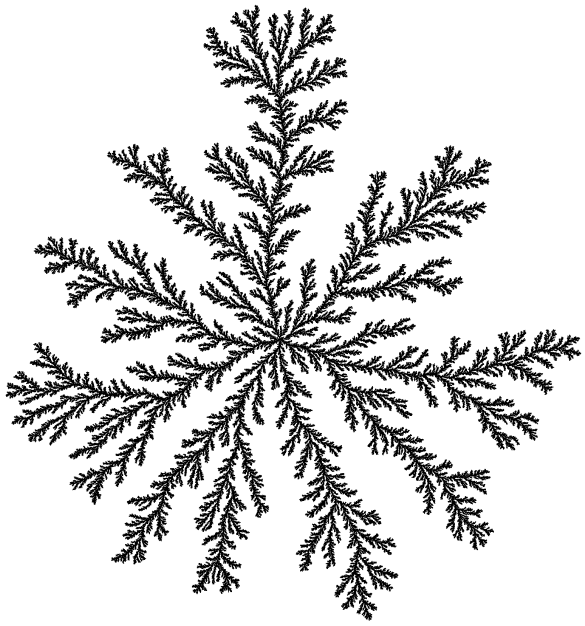

Figure 3.1: A diffusion-limited aggregate with 5×10^7 particles. Made by Ellak Somfai and appearing in Mathiesen, Procaccia, Swinney, and Thrasher [86], used with permission.

3.1.2 Harmonic measure and conformal mapping

For DLA, the harmonic measure is the probability of a random walker to diffuse from infinite distance and collide with a location on the existing aggregate [61]. For viscous fingering, the harmonic measure is the velocity (up to a normalization factor) that a piece of the interface will grow, or equivalently, it is the probability measure of the pressure gradient field surrounding a viscous fingering pattern. Large DLA clusters and viscous fingering patterns can have regions of very small harmonic measure. For a DLA cluster of 3×10^4 particles, the harmonic measure can be 10^{25} times smaller at the back of deep fjords compared to the tips of fingers [85]. For a DLA cluster of 5×10^7, the probability to hit the back of a fjord can be as small as 10^{-70} [109].

For the present work, we calculate the harmonic measure from the conformal map of the growth pattern. Most simply, a conformal map is a mathematical function which preserves angles. The construction of a conformal map from the exterior of the unit circle to the exterior of an arbitrarily complicated line was developed by Bouchbinder, Mathiesen, and Procaccia [16]. It involves first modifying the unit circle with a semicircular bump and then mapping this back to the exterior of the unit circle. These semicircular bumps are incorporated repeatedly in this fashion to build up the arbitrary viscous fingering pattern. The method we used was developed by J. Mathieson and I. Proccacia and the details of the calculation of the harmonic measure and conformal map are in our *Europhysics Letter* [86].

3.1.3 Box-counting dimension

Another property of our growth patterns is the fractal dimension. There are many kinds of dimensions which can be calculated [56]. The simplest of the methods will be presented here. Fractal objects have non-integer values of dimension. Often we know that an object's dimensionality lies between two integers. For example, the Sierpinski gasket (Fig. 3.2) has more dimensions than a line but it does not fill the entire plane; the dimension is somewhere between 1 and 2.

One method to quantify the dimension more accurately is the box-counting method. The first step is to count the minimum number of boxes with side length R needed to entirely cover the object in question (Fig. 3.3). If the object has a dimension between 0 and 1, then the boxes are line segments. If the object has a dimension between 1 and 2, then the boxes are squares, etc. Then the side length is changed and the number of boxes counted again. If the number of boxes $N(R)$ as a function of R scales as a power law

$$N(R) \propto \lim_{R \to 0} R^{-D_0}, \tag{3.1}$$

then D_0 is the object's dimension. For real data, the limit $R \to 0$ can only be approximated because of the presence of noise and the limits of resolution. Therefore to measure D_0 a range of box sizes must be chosen to calculate the slope of $log(N(R))$. The choice of the range can introduce error into the measurement of D_0.

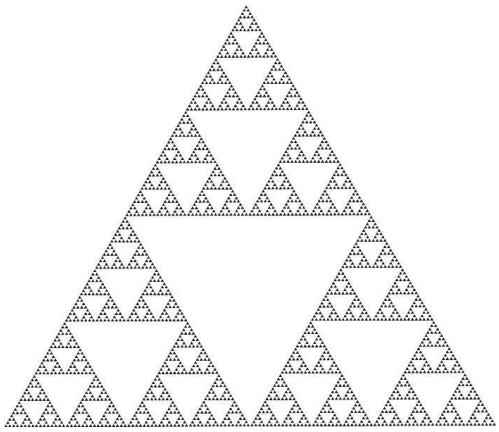

Figure 3.2: Sierpinski gasket, a fractal object created by successively removing the inner triangle formed by the connection of the midpoints of the closest line segments. The subunits of the fractal are the same as the original pattern.

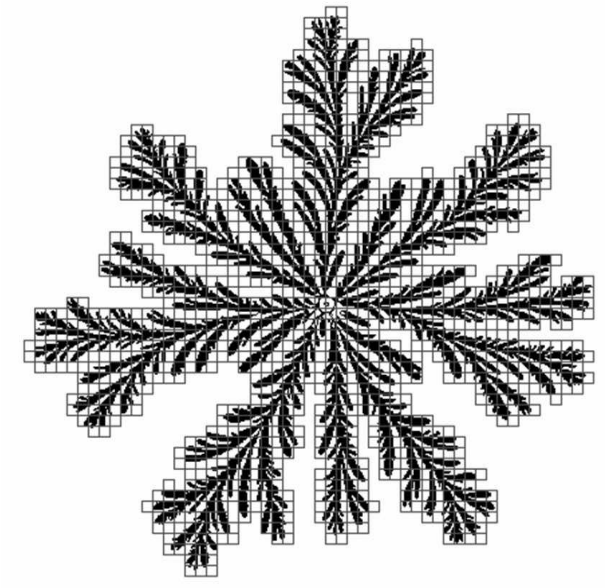

Figure 3.3: A viscous fingering pattern subdivided by a grid of boxes, used in the box-counting method of calculating fractal properties. This image was created by Harry Swinney and Olivier Praud, used with permission.

3.1.4 Long time asymptotics and the dense branching morphology

The fractal dimensions of DLA and viscous fingering patterns have been studied before [108], and it appeared at first that the dimensions depended on the size of the cluster and the geometry in which it was grown [33]. The argument was that DLA is not really a fractal, because the lengths scale differently depending on the size of the cluster. But Somfai, Sander and Ball presented evidence that scaling of lengths in DLA is due to a slow crossover with increasing cluster size which can account for the observed differences [130]. And it was later shown that the dimension of DLA is the same for both the channel and the radial geometries [129].

The long term asymptotics of viscous fingering patterns has also been a puzzle, though for different reasons. For a growing pattern, surface tension stabilizes the interface and smooths out regions of high curvature. At the same time, the interface is unstable and some noise on the interface is amplified to macroscopic features. The question is "Will the instability win or will surface tension win?" For constant pressure boundary conditions, the velocity of the farthest tip is a constant until the tip approaches the edge of the experimental cell [108]. Under these conditions, the patterns are asymptotically fractal by several measures, including the box-counting dimension and an angular measure of the growth regions [108]. However, Yeung and Jasnow claimed that for constant pumping rate boundary conditions in a circular geometry, the growing pattern will not be a fractal at long times [150]. For constant flux, the farthest tips are slowing down as the average radius of the pattern grows.

The experimental patterns that the two authors present are from Ben-Jacob *et al.* and demonstrate what is called the "dense branching morphology" (left image in Fig. 3.4) [9]. In fact, Ben-Jacob *et al.* observed the dense branching morphology for viscous fingering patterns grown with both constant pumping rate and constant pressure [9]. From my estimates based on the description of their experimental apparatus, the deflection of the Hele-Shaw plates was comparable to the gap between the plates. Mickey Moore saw similar dense branching patterns in experiments conducted with an early Hele-Shaw cell that bowed greatly under the pressure of the injected fluid. In a more rigid apparatus where the gap thickness changes less than a few percent under the maximum pressures tested, dense branching morphology was not observed, which suggests that the changing gap thickness could account for the different morphology between the two patterns in Fig. 3.4. The right image in Figure 3.4 shows a typical pattern grown at constant pumping rate in our radial Hele-Shaw cell with very little plate bending.

3.1.5 Singularity spectrum $f(\alpha)$

A multifractal can be thought of as the intersection of many fractals of different dimensions that creates a single pattern [56]. To extract all the scalings from such a pattern, the previous box-counting procedure for calculating D_0 needs to be modified [52, 54].

If an object is divided into boxes of size L, the fractional area (or probability) that is filled in each box i is $p_i(L) = A_i/A$, where A_i is the area

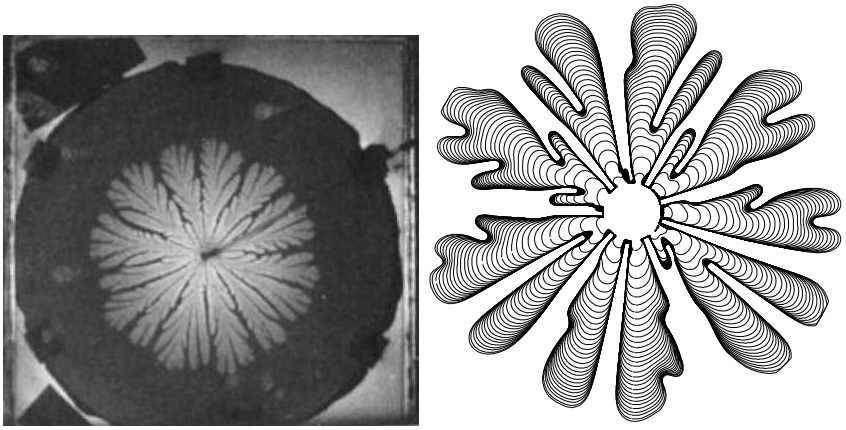

Figure 3.4: Left: The dense-branching morphology of air into glycerol at a pressure of 100 mm of Hg and a plate spacing of 0.5 mm. The Hele-Shaw plates are 58 cm in diameter. Right: A typical viscous fingering pattern grown in our radial cell with a nominally constant pump rate of 1/30 cm^3/s and a diameter of 19 cm. The figure on the left was reprinted with permission from Fig. 1(a) of Ben-Jacob *et al.* [9]. Copyright 1986 by the American Physical Society.

that the pattern occupies inside of the box i and A is the total area of the box. Then centered on the same point, we can measure how p_i scales with the box size,

$$\lim_{L\to 0} p_i(L) \propto L^{\alpha_i}, \tag{3.2}$$

where α_i is the scaling exponent for that point (also called the singularity strength). Next we count the number of boxes with a scaling exponent between α and $\alpha + d\alpha$ and call it $F(\alpha)d\alpha$. Assuming that $F(\alpha)d\alpha$ scales with L, the singularity spectrum can be defined as $f(\alpha)$, where

$$F(\alpha) \propto L^{-f(\alpha)}. \tag{3.3}$$

This definition follows Halsey *et al.* and Hilborn [52, 56]. The maximum of the $f(\alpha)$ spectrum is the box-counting dimension D_0 [56]. A discontinuity in $f(\alpha)$ indicates a "phase transition," analogous to thermodynamics, where a distinct change in the dynamics is observed [25, 50].

To calculate the singularity spectrum, we are performing two box-counting steps. First we count to find the local scaling of each point, then we count to find the dimension of all points which share the same local scaling exponent [48]. For viscous fingering, large α exponents correspond to the fjords (low growth probability), and small α exponents correspond to the tips (high growth probability).

Figure 3.5: An unprocessed image of a typical fractal growth pattern. The bubble is 22 cm in diameter.

3.2 Experimental notes

Experiments growing fractal viscous fingering patterns were performed in the radial Hele-Shaw cell described in the Introduction (Chapter 1) with a gap thickness of 0.127 mm $\pm$ 0.13 μm. The radial cell was modified by Olivier Praud to maintain a constant pressure difference between the center of the air bubble and the surrounding oil reservoir. The gap was carefully leveled by recording the slow drift of air bubbles between the plates. Data existed from a previous study by Olivier Praud and Harry L. Swinney reported in [108] with a viscosity of 345 mPa s and a pressure difference from 0.1 to 1.25 atm. I performed additional experiments with oil of a viscosity of 50.8 mPa s and pressure differences ranging from 0.1 to 0.6 atm.

Figure 3.5 is a raw image showing a viscous fingering pattern growing

in the radial Hele-Shaw cell. The air is the light region and the oil is the dark region. The white exterior is the cylindrical light diffuser covering the experiment. High resolution images were desired, so the camera's lens was zoomed so that the largest bubble size took up as much as possible of the camera's field of view. Care was taken that the images were not blurred by the fast motion of the interface, especially at the tips of the fingers. Determining the location of the interface is less accurate and more difficult for blurred tips. To accomplish this, the camera's settings were adjusted for each particular experiment, depending on the interface speed. The lens focus and aperture were set manually for the best contrast between the oil and air regions. Using the DVC Camera Control Panel program, the exposure time was set as short as possible (to allow for the greatest frame rate and the sharpest interfaces) with a light level still adequate for proper contrast. The narrow diffuser cylinder had a small hole for the lens which caused a small dark spot in the center of the cell. The area within the dark spot had little contrast at the interface and had to be discarded before extracting the location of the interface. The scale of the image was measured from the size of the white central needle valve, which is 0.618 cm and ranged from 29 to 70 pixels. The measurement was accurate within $\pm$ 1 pixel.

The interface was the dividing line between air and oil (Fig. 3.6). The radii of the patterns were grown as large as possible in our experimental cell. However, we restricted our study to patterns with no instances of pinch-off (Fig. 3.7) [148], because the effect of pinch-offs on the fractal dimension is

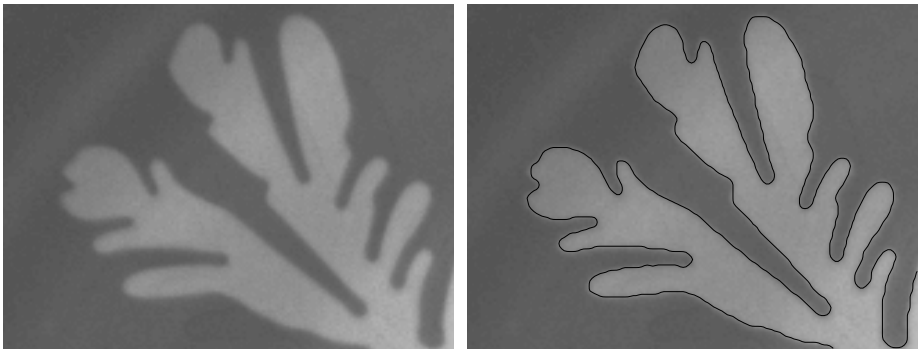

Figure 3.6: The line of the interface was extracted from the images by locating the steep change in intensity between air (light area) and oil (dark area). The image is a closeup of the upper left corner of Fig. 3.5.

unknown. For the same experimental conditions, some growth series would have pinch-off events, while others would not; the occurrence of this process depended sensitively on the initial noise conditions. No differences were observed between patterns far from pinch-off and patterns with no pinch-off events that were nonetheless close to pinch-off [108, 144].

As a consistency check, the fractal dimension for 50.8 mPa s and 345 mPa s viscous fingering patterns was measured to be 1.71 ± 0.02, consistent with the previously found $D_0 = 1.70 \pm 0.02$ [108]. The box-counting method was also confirmed on a Sierpinski gasket, which has an exact solution for the fractal dimension of $log(3)/log(2) \approx 1.58496$. The dimension of the gasket was measured to be 1.50 to 1.58, depending the exact range of box sizes over which the scaling was calculated. As in previous studies, the box-counting dimension was consistently below the real value.

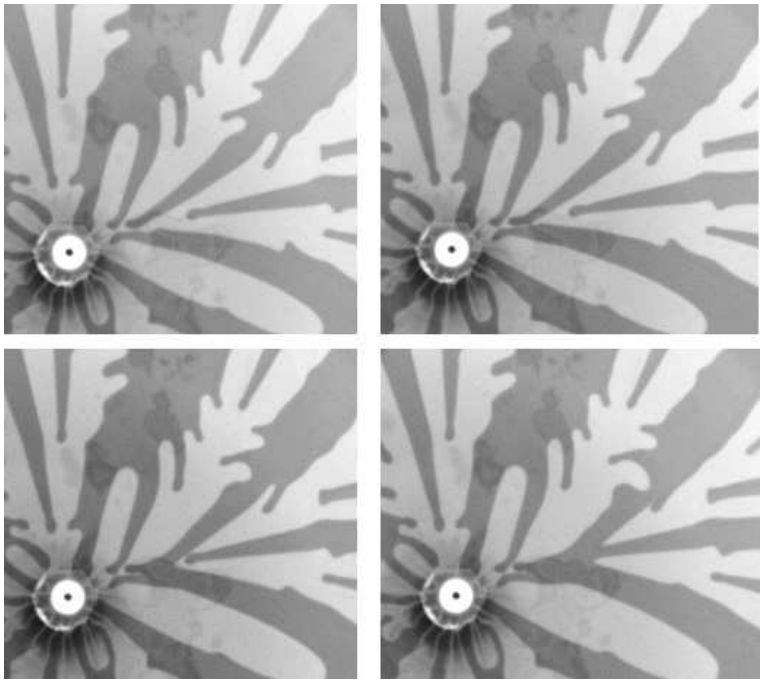

Figure 3.7: Image sequence of pinch-off occurring to the right of the needle valve. Successive frames are separated by 1/12 s. The circular white needle valve is 0.618 cm in diameter. The faint, irregular spots are oil films on the top of the acrylic window.

3.3 Summary of results

Figure 3.8 summarizes the results of this study. The singularity spectra for viscous fingering patterns and DLA are the same within the uncertainty. The curves are averages of the $f(\alpha)$ curve calculated for many realizations of growth patterns. The large α exponents correspond to regions of slow growth (i.e. the fjords), and small α exponents correspond to regions of high growth (i.e. the finger tips). The spectra were measured for two sets of viscous fingering patterns. One set of patterns were grown in a silicone oil of viscosity $\mu = 50.8$ mPa s and the other set was grown with $\mu = 345$ mPa s. To confirm the spectra of viscous fingers, 10^6 random walkers were released and where they struck the pattern's interface were tallied. This sampled the most probable regions of the interface and confirmed our calculations for the singularity spectrum of the harmonic measure near the tips of the fingers. For more details, see Mathiesen, Procaccia, Swinney, and Thrasher [86].

3.4 Scaling of area with perimeter

We performed another series of experiments to observe if different boundary conditions affect the growth properties of fractal viscous fingering patterns. The two most common boundary conditions are constant pressure difference and constant pumping rate. The experiments described above were conducted at constant pressure difference Δp from 0.1 atm to 1.25 atm. More experiments were completed at constant pumping rates Q, using a syringe pump to extract oil at a particular rate from the buffer. In the constant

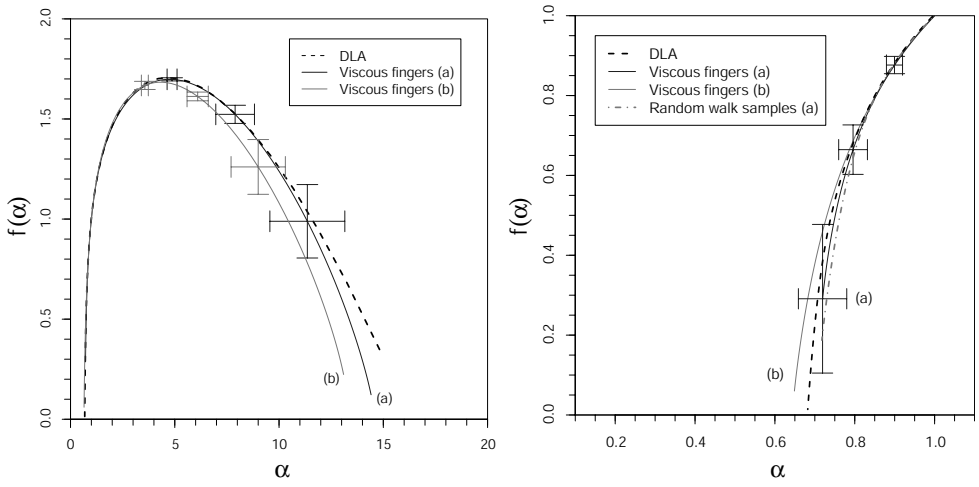

Figure 3.8: Left: Singularity spectra $f(\alpha)$ for the harmonic measure of the viscous fingering patterns and DLA. The spectra are averages over many patterns. Curve (a) is for 15 bubbles of viscosity $\mu = 345$ mPa s. Curve (b) is for 15 bubbles of viscosity $\mu = 50.8$ mPa s. Curve (c) is the $f(\alpha)$ spectrum for DLA clusters with more than 5×10^7 particles. Left: A close-up of the left-hand side of the spectra, where the probability of growth is largest (i.e. on the finger tips). The spectra are consistent with results obtained by releasing 10^6 random walkers and averaging where they strike the experimental viscous fingering patterns. The error bars are for viscous fingering data labeled (a). Reprinted with permission from Mathiesen, Procaccia, Swinney, and Thrasher [86].

pumping rate experiment, the radial cell was filled with silicone oil of viscosity of 50.1 mPa s and the gap thickness was 0.127 mm.

We decided to measure the scaling of area A of the bubble versus the perimeter P of the bubble ($A \propto P^{\beta}$). Many other studies have measured the different scalings of DLA and viscous fingering growth patterns [43, 124, 148]. Wiggert and Maxworthy measured the scaling of area with perimeter for rectangular viscosity fingering experiments to be between 1.26 to 1.42 [148]. Fast and Shelley measured the scaling of area with perimeter of a simulated viscous fingering pattern to be $\beta \simeq 1.45$ for large clusters. When the scaling stabilized, they decided it was asymptotic; however, there does not appear to be any agreement on how to measure whether or not a viscous fingering pattern is asymptotic. At least three different methods have been proposed:

1. the unscreened angle approaching a constant distribution [108]
2. the fraction of air in a small annular section at some radius starts high and approaches 0.6 [134]
3. the scaling of area with perimeter becomes 1.45 [43].

My preliminary results show a difference between the two conditions, which implies that asymptotic conditions are different for each boundary condition. Figure 3.9 shows two typical growth series for constant pressure difference and constant pumping rate. Figure 3.10 shows the measured scaling exponent as a function of forcing. For the constant pressure difference experiments, the

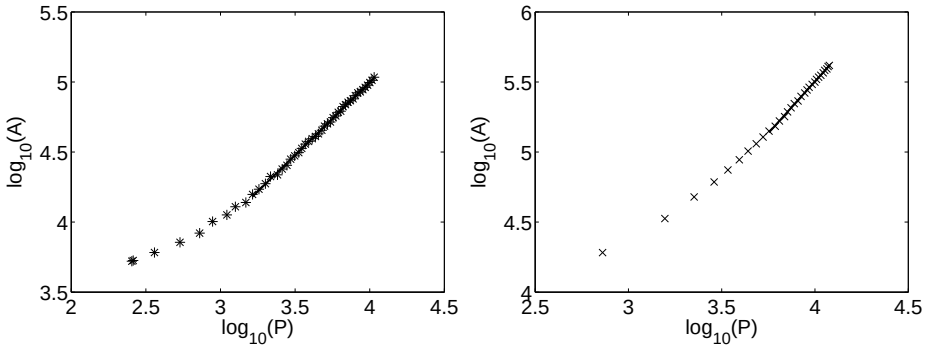

Figure 3.9: Area A scales with perimeter P as a power-law. Left: A typical growth series for constant pressure difference, $\beta = 1.04$. The straight line plotted over the data shows the range over which the slope is computed. Right: A typical growth series for constant pumping rate, $\beta = 1.48$.

forcing parameter is the capillary number, where the velocity is measured from the farthest tip. To facilitate a comparison with Fast and Shelley, the capillary numbers were calculated in the same way as in [43], $\mathrm{Ca} = (12\mu/b^2)(V/\sigma)R_0^2$, where R_0 was the radius of the slightly perturbed initial bubble in the simulation. To compare their simulations with our experiments, the velocity V of the farthest point of the experimental interface was measured when the average radius of the bubble R_0 was 2 cm. For the constant pumping rate experiments, the forcing parameter is the pumping rate. As the figures show, the scaling exponents for the constant pressure difference experiments are constant within uncertainty for different forcing, while the scaling exponents for the constant pumping rate experiments decreases as forcing increases. If to compare the scaling exponents of high forcing for two boundary conditions with each other, they are within uncertainty the same. The data at low pumping rate had a

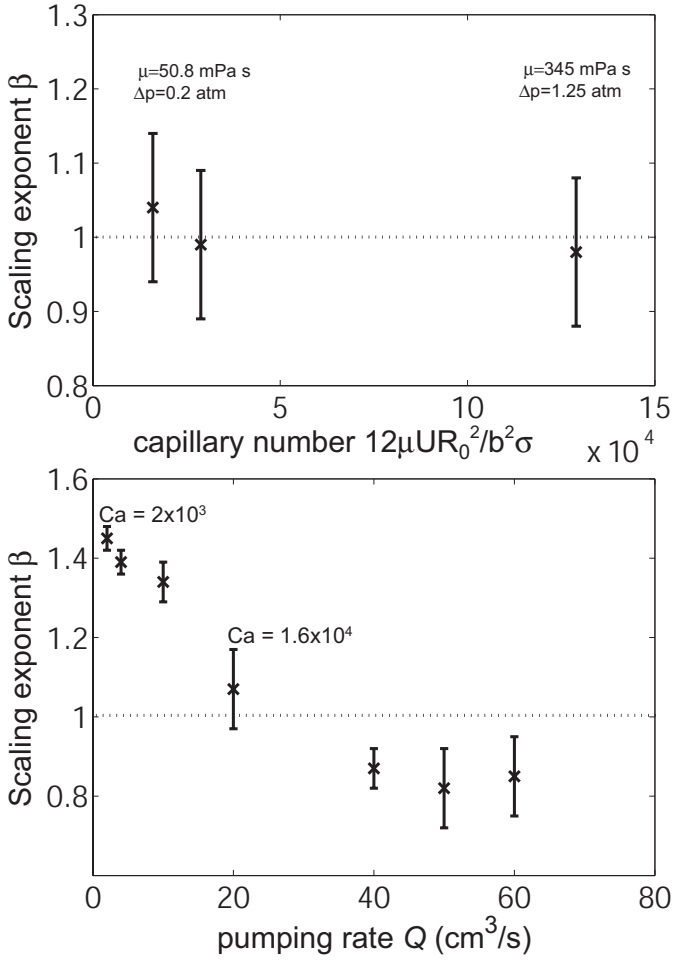

Figure 3.10: The scaling exponents for different boundary conditions. Top: The patterns grown at a constant pressure difference have the same scaling independent of the magnitude of the forcing within uncertainty. A scaling exponent of one would be a linear relationship between the capillary number and the perimeter. The uncertainty is mostly from the measurement sensitivity of the scaling exponent with the range over which the slope is computed (see Fig. 3.9). The data points on the left are from different bubbles but the same viscosity and pressure difference (μ = 50.8 mPa s and Δp=0.2 atm). The difference in the capillary number for two experiments at the same conditions is most likely because the pressure gauge was not accurate at lower pressure. Bottom: Patterns grown at a constant pumping rate have different scaling exponents, depending on the level of the forcing. Capillary numbers are measured when the bubble had a radius of $R_0 = 2$ cm.

particularly high scaling exponent, but this regime of low capillary number is not represented in the data taken at a constant pressure difference.

However, these are preliminary results. Without a thorough and systematic study, it is not possible to rule out other factors that might contribute to the apparent difference between constant pressure difference and constant pumping rate. For example, the pumping rate of the syringe pump and the actual pumping rate in between the plates might be different because of air bubbles in the cell or flexibility of the pipes.

Chapter 4

Dynamics of harmonic moments in Laplacian growth

4.1 Introduction

The different patterns created by non-equilibrium interfacial processes exhibit a rich variety of geometric properties [29, 49].[1] Their growth is often unstable. Examples include crack propagation, fluid-fluid interface dynamics, and crystal and biological growth. Despite the very different growth mechanisms, these systems often display similar behaviors, such as fractal interfaces, power-law scaling, and selection rules. These universal features inspire the hope that there is a common description which can account for the similarities. Significant discoveries in physics, new mathematical methods, and even new branches of science (e.g. fractal geometry [84]) have resulted from the study of these universal features, which have attracted a great deal of attention particularly during last 30 years [29, 49].

[1] This section is in preparation by Alexander Leshchiner, me, Mark B. Mineev-Weinstein, and Harry L. Swinney as "Harmonic moment dynamics in Laplacian growth" to be submitted to *Physical Review E*. Mark Mineev-Weinstein developed the theory, I modified the experimental apparatus, Alex and I ran the experiments, Alex and I wrote the Matlab code for the analysis, all four of us discussed the data and wrote the paper.

4.1.1 Laplacian growth in viscous fingering

The simplest process leading to unstable universal patterns is Laplacian growth, which is the growth of an interface driven by the local gradient of a potential field ϕ that obeys Laplace's equation $\nabla^2\phi = 0$. The simplest example of the Laplacian growth is viscous fingering in the Hele-Shaw cell. We will use viscous fingering as an archetype of Laplacian growth to experimentally test a theoretical prediction of Mark Mineev-Weinstein. Figure 4.1 shows four viscous fingering patterns grown in the radial Hele-Shaw cell described in Sect. 1.2, where viscous silicone oil is displaced by air between two closely spaced parallel plates. As oil is removed from a buffer surrounding the plates, air enters between the plates through a central hole in the bottom plate.

As the air bubble expands, its interface is unstable. The depth-averaged velocity $\mathbf{v}$ and pressure p are related via Darcy's law [72]

$$\mathbf{v} = -\frac{b^2}{12\mu}\nabla p \qquad \text{(in oil)}, \tag{4.1}$$

where b is the spacing between the plates and μ is the oil's dynamic viscosity. The velocity in the air domain also obeys Darcy's law, but since the viscosity contrast between the oil and air is so large, the air is almost inviscid and any small pressure drop in the air is neglected. The velocity components normal to the interface of the two fluids coincide [72], hence

$$V = -\frac{b^2}{12\mu}\partial_n p \qquad \text{(at the interface)}, \tag{4.2}$$

where ∂_n is the normal component of the gradient. The process is called Laplacian because, assuming that the oil is incompressible ($\nabla \cdot \mathbf{v} = 0$), the

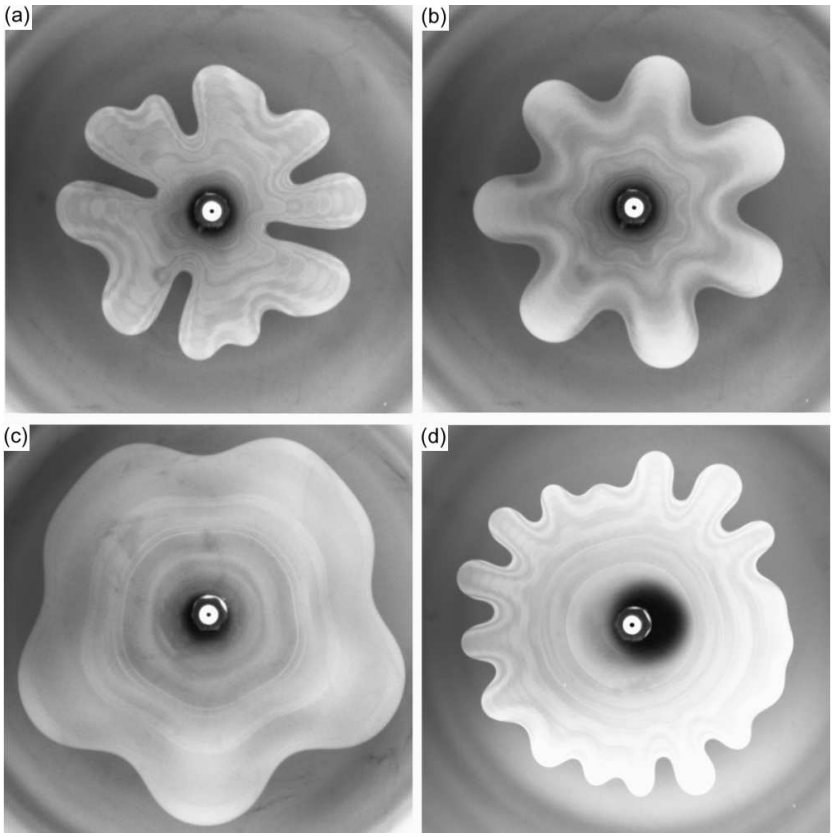

Figure 4.1: Controlling the viscous fingering instability, images of four air bubbles with different growth conditions. Each box is 13.85 cm wide. Bubble (a) was grown at a constant pumping rate of 0.52 mL/min. Bubbles (b),(c) and (d) were grown with varying pumping according to Bataille formula (4.21). See Fig. 4.3 for pumping details of bubble (b).

pressure field is a harmonic function

$$\nabla^2 p = 0 \qquad \text{(in oil)}. \tag{4.3}$$

Equations 4.1-4.3 must be supplemented by a pressure condition at the interface and a boundary condition for the pressure at infinity to completely formulate the problem. The pressure jump across the oil-air interface was calculated by Park and Homsy [101] to be

$$p = -\sigma\left(\frac{\pi\kappa}{4}\right) + \frac{2\sigma}{b}\left[1 + 3.8\left(\frac{\mu V}{\sigma}\right)^{2/3}\right], \tag{4.4}$$

where κ is the local curvature of the interface in the horizontal plane. The first term of the pressure jump is the traditional pressure condition $p = -\sigma\kappa$ [121] corrected by Park and Homsy to include a factor of $\pi/4$. The second term accounts for the thin wetting layer of oil left behind on the glass plates of the Hele-Shaw after the interface advances. The faster the interface travels, the thicker the film that is deposited and the larger the correction term is [73, 101, 133]. The predicted thickness of the film was experimentally confirmed by Tabeling and Libchaber for $6 \times 10^{-4} < \frac{\mu V}{\sigma} < 3 \times 10^{-3}$ [131]. This film can be seen as interference fringes on the images in Fig. 4.1, because the interface is slowing down as the bubble expands, leaving a successively thinner film.

In the radial geometry, the asymptotic pressure boundary condition in the oil far from the interface is

$$p = -\frac{3\mu Q}{\pi b^2}\log(x^2 + y^2) \qquad (\text{for } x^2 + y^2 \to \infty), \tag{4.5}$$

where Q is the pumping rate (the rate of area growth), which may depend on time. This system of equations (4.1-4.5) constitutes 2D viscous fingering, which is the prototype of Laplacian growth.

Laplacian growth is one of the famous classical free-boundary problems [47, 68]. Being a highly unstable, dissipative, non-equilibrium, and nonlinear process, it produces universal patterns [118, 121, 126]. It occurs in many physical systems and is known by different names, such as crystal growth, amorphous solidification [74], electrodeposition [26, 125], bacterial colony growth [8], diffusion-limited aggregation (DLA) [149], motion of a charged surface in liquid Helium [155], and fractal growth (of the DLA type) in a viscous medium [108]. Many features are still unexplained, despite long effort and full knowledge of the laws of physics standing behind the process. There are thousands of articles (theoretical, experimental, and computational) devoted to Laplacian growth if one counts the works on closely connected areas, such as the Stefan problem (solidification) [66, 75], DLA fractal growth, and the phase-field model [55].

4.1.2 Harmonic moment description of viscous fingering

This work is devoted to applying a powerful description of Laplacian growth called harmonic moments to the growth of viscous fingering patterns. As we will see, the harmonic moment description is uniquely matched to Laplacian growth and predicts several remarkable features of the process. All of the harmonic moments except the zeroth moment are conserved during Laplacian

growth without surface tension. Our eventual goal is to test whether or not this prediction is observable and robust.

Harmonic moments are defined as[2]

$$M_k = -\int_D z^{-k}\,\frac{dxdy}{\pi} = \oint_\Gamma z^{-k}\,\overline{z}\,\frac{dz}{2\pi i}, \tag{4.6}$$

where $k = 1, 2, \ldots, \infty$, $z = x + iy$, $\overline{z}$ is the complex conjugate of z, and the domain of integration D is *exterior* to the pattern's boundary Γ.[3] Harmonic moments form a complete basis for representing any 2D interface, regardless of its complicated shape, provided that D is analytic and singly connected [42, 99]. Like Fourier modes, each harmonic moment M_k corresponds to a particular aspect of the interface. M_0 is the area of the domain D divided by π. Moments M_k for $k > 1$ are measures of the components present on the nearly circular interface of the form $z = R\ exp(i\phi)[1 + a\ exp(-ik\phi)]$, where ϕ is the phase, a is an amplitude, and R is the bubble radius. For an approximately n-fold pattern [e.g. Fig. 4.1(b) is approximately 7-fold symmetric and Fig. 4.1(c) is approximately 5-fold symmetric] the dominant moments are M_n,

[2]This is the definition of exterior harmonic moments, which is relevant for the Laplacian growth described in this work. Interior moments are defined similarly, but with positive powers of z under the integral, and the domain of integration occupies the *interior* of the pattern.

[3]For completeness, we should mention that harmonic moments are defined differently in different geometries. For instance in a rectangular geometry, which corresponds to a Hele-Shaw cell in a form of a channel [121], the domain of oil D_{oil} occupies a semi-infinite strip and the harmonic moments' definition is

$$M_k = \int_{D_{oil}} e^{-kz}\,\frac{dx\,dy}{\pi}. \tag{4.7}$$

For the wedge geometry, the definition of M_k is the same as for the radial one in (4.6). The definition for multiconnected cases are less trivial and are presented in [68].

M_{2n}, M_{3n}, etc. We should be careful in comparing magnitudes of moments directly though, since different moments have different units; the moment M_k has units of cm^{2-k}. In contrast to the Fourier basis, there is no general inverse transform from harmonic moments to the shape of the domain. Harmonic moments should not be confused with the harmonic measure [56], which is the growth velocity along the interface, and they should not be confused with the moments of some distribution.

In 1972 S. Richardson showed that, during Laplacian growth in the absence of surface tension, all moments M_k except $k = 0$ are *conserved in time* [114]. Richardson's analysis relied on a finite D (e.g. the interior of a viscous domain). The whole evolution of $D(t)$ is then reduced to the time-dependent area $A(t) = \int^t Q(\tau)d\tau \propto M_0$. This result was extended by Mark Mineev-Weinstein to an infinite viscous domain exterior to an interface [92], which is the case in our experiments. The moments are defined purely geometrically, but they are more than geometric measures. Harmonic moments form a basis that is matched to Laplacian growth so well that the moments are conserved quantities (i.e. the geometric objects contain the physics). The same is not true for other decompositions, such as Fourier modes, Pade-approximants [5], and wavelets [91]. This conservation of harmonic moments relies on the surface tension being zero. However, the experiments we conducted have surface tension, so we must be able to account for its effects.

4.2 Theory of the dynamics of harmonic moments with nonzero surface tension

In Laplacian growth with nonzero surface tension σ, the moments M_k are no longer constants. The time derivative of M_k follows from (4.1) and (4.6):

$$\frac{dM_k}{dt} = \frac{b^2}{12\mu} \oint_\Gamma z^{-k}\, \partial_n p\, \frac{dl}{\pi}.$$

We want to exchange the derivative between p and z^{-k}, so we add and subtract $p\, \partial_n z^{-k}$ from our integrand

$$\frac{dM_k}{dt} = \frac{b^2}{12\mu} \oint_\Gamma (z^{-k}\, \partial_n p - p\, \partial_n z^{-k} + p\, \partial_n z^{-k})\, \frac{dl}{\pi}, \tag{4.8}$$

where l is the arclength along the interface Γ. The integral of the first two terms is zero by virtue of Gauss's theorem, after using (4.2) and the analyticity of z^{-k} in D:

$$\begin{aligned} \oint_\Gamma (z^{-k}\, \partial_n p - p\, \partial_n z^{-k}) dl &= \oint_\Gamma (z^{-k} \nabla p - p \nabla z^{-k}) \cdot \vec{n}\, dl & (4.9) \\ &= \int_D \nabla \cdot (z^{-k} \nabla p - p \nabla z^{-k})\, dx\, dy = 0. & (4.10) \end{aligned}$$

We now have the pressure outside of the derivative

$$\frac{dM_k}{dt} = \frac{b^2}{12\mu\pi} \oint_\Gamma p\, \partial_n z^{-k}\, dl. \tag{4.11}$$

Substituting the Park and Homsy expression (4.4) for the pressure on the interface, we have

$$\begin{aligned} \frac{dM_k}{dt} &= -\frac{\sigma b^2}{48\mu} \oint_\Gamma \kappa\, \partial_n z^{-k}\, dl & (4.12) \\ &+ \frac{\sigma b}{6\mu\pi} \oint_\Gamma \left[1 + 3.8 \left(\frac{\mu V}{\sigma} \right)^{2/3} \right] \partial_n z^{-k}\, dl. & (4.13) \end{aligned}$$

Using the definition of curvature $\kappa = d\theta/dl$ where θ is the angle of a line tangent to the interface and the identity $\partial_n z^{-k} = -i\partial_l z^{-k} = ikz^{-(k+1)}dz/dl$, where ∂_l denotes a tangential derivative, the expression becomes

$$\frac{dM_k}{dt} = -\frac{\sigma b^2 ik}{48\mu} \oint_\Gamma z^{-(k+1)} \frac{dz}{dl}\frac{d\theta}{dl}\, dl \tag{4.14}$$

$$+ \frac{\sigma bik}{6\mu\pi} \oint_\Gamma \left[1 + 3.8\left(\frac{\mu V}{\sigma}\right)^{2/3}\right] z^{-(k+1)} \frac{dz}{dl}\, dl. \tag{4.15}$$

Next we change the integrand with $dz/dl = \exp(i\theta)$,

$$\frac{dM_k}{dt} = -\frac{\sigma b^2 ik}{48\mu} \oint_\Gamma z^{-(k+1)} \exp(i\theta)\, d\theta \tag{4.16}$$

$$+ \frac{\sigma bik}{6\mu\pi} \oint_\Gamma \left[1 + 3.8\left(\frac{\mu V}{\sigma}\right)^{2/3}\right] z^{-(k+1)}\, dz. \tag{4.17}$$

Finally, integrating by parts, we arrive at

$$\frac{dM_k}{dt} = \sigma k \frac{b^2\pi}{12\mu}\left[\frac{k+1}{4} \oint_\Gamma e^{i\theta} \frac{dz}{z^{k+2}}\right. \tag{4.18}$$

$$\left. + \frac{3.8\, i}{\pi b/2} \oint_\Gamma \left(\frac{\mu V}{\sigma}\right)^{2/3} \frac{dz}{z^{k+1}}\right]. \tag{4.19}$$

This relationship makes testing the harmonic moments description of Laplacian growth feasible, because it no longer requires zero surface tension. Note that the moment's evolution dM_k/dt goes to 0 as surface tension σ vanishes, which reproduces the conservation of moments in a simple, well-defined manner. The surface tension is now a regular rather than a singular perturbation.

Five parameters enter our theory: surface tension, viscosity, gap thickness, size of the bubble, and time. Given the interface dynamics and any four of the parameters, we can calculate the fifth. We can measure the surface

tension, viscosity, and gap thickness using traditional equipment, such as a tensiometer, rheometer, and micrometer screw gauge. We know the size of the bubble and time from the images and the image times. So we know all five parameters and we can measure dM_k/dt and V directly from our experimental images; thus we can directly test the theory.

4.3 Experiment

4.3.1 Apparatus

Silicone oil was displaced by air in a circular Hele-Shaw cell consisting of two horizontal, closely spaced glass plates with a central hole in the bottom plate (Sect. 1.2). The optically polished glass plates have a diameter of 28.8 cm and a thickness of 6 cm, as described in [96, 108, 118]. The gap between the plates was 125.5 $\pm$ 4.6 μm or 384.0 $\pm$ 5.3 μm. Most of this uncertainty is from using a micrometer to measure the thickness of the metal shim used to set the height of the gap. The nonuniformity of the gap thickness is known more precisely than the absolute thickness, 0.3 microns for the smaller gap and 1.6 microns for the larger gap, because the uniformity was measured by interferometry. A sodium lamp was suspended above the cell and the experimentalist stood over the cell and counted the number of interference fringes that appeared or disappeared as he moved his head from directly above the center of the plates to directly above the outer edge of the plates.

An annular buffer and the gap are initially filled with silicone oil (Dow Corning 200 fluid at 24 °C: viscosity $\mu = 49.9 \pm 0.3$ mPa s, surface tension

$\sigma = 21.12 \pm 0.02$ mN/m, density $\rho = 0.9585 \pm 0.0005$ g/cm^3). An initial, nearly circular bubble was obtained by withdrawing oil slowly from the buffer surrounding the gap between the plates, while the hole in center of the bottom glass plate was open to the atmosphere. The bubble was imaged from above with a CCD camera (1300 x 1030 pixels, 12 frames per second maximum).

4.3.2 Growing a bubble

A bubble was grown using a precision computer controlled syringe pump to remove oil from the annular buffer at the withdrawal rate $q(t) = b\,Q(t)$ after an initial bubble had been grown. The withdrawal rate Q has units of area per unit time, while q has units of volume per unit time. The initial bubble radius was chosen to be at least 20 mm, which is sufficiently large to give good resolution by the imaging system. Depending on the conditions of the experiment, the frame rate ranged from 1/6 frames/s to 2 frames/s. Experiments ranged from 30 to 1600 seconds with a typical duration of 300 seconds.

To avoid any interactions between modes, we wanted to watch a single moment evolve individually as a perturbation on a nearly circular bubble. A bubble with only one dominant moment, say M_n, will have an approximate n-fold symmetry (Fig. 4.1).[4] As a bubble's area A grows, its average radius $R = \sqrt{A/\pi}$ increases. To grow a bubble with a single dominant moment n,

[4]The subscript n refers to the single moment number of a bubble with a particular n-fold symmetry. Typically the single dominant moment number n is grown using the Bataille formula (4.21). The subscript k refers to an arbitrary moment number.

the pumping rate must decrease as the bubble's radius R increases such that the most unstable wavelength λ_c is

$$\lambda_c \approx \frac{2\pi R}{n}. \tag{4.20}$$

Linear stability analysis by Bataille [7] and later by Paterson [102] provides an expression for the withdrawal rate Q_n needed to keep the same n-fold perturbation growing the fastest:

$$Q_n = \frac{\pi^2 \sigma b^2}{24 \mu R}(3n^2 - 1). \tag{4.21}$$

The units of both sides of this equation are m^2/s. Although the original Bataille analysis used the traditional pressure jump ($p = -\sigma\kappa$), we used the first term of the Park and Homsy pressure jump ($p = -\sigma\kappa\pi/4$) to calculate Q_n. The basic idea and first implementation of this method was done by Olivier Praud.

We used (4.21) to adjust the pumping rate as the bubble radius increases, to maintain a maximal growth rate for a chosen n-fold mode (the chosen number of fingers). A feedback loop made of the camera imaging the bubble and the LabVIEW-controlled pump ensures the correct withdrawal rate Q_n. Maintaining the withdrawal rate according to the Bataille formula does not prevent perturbations of other moment numbers from growing. However, the growth rate of perturbations with moment number other than n diminishes as the moment numbers become further away from the mode of maximal growth n. Pumping with this method insures that the desired moment number grows most quickly. While this method does not produce bubbles with

only a single mode, a distinct n-fold symmetry can be achieved, as Fig. 4.1(b) demonstrates.

The exact conditions at the initial stages of a bubble's growth determines the bubble's dominant mode structure at early times. If the initial growth stage selects moment numbers that are not desired, then growing the desired moment number is much more difficult, even to the extent that it appears to us that the initial structure of the bubble predetermines the bubble's resulting shape and that non-uniformities and errors in the withdrawal rate are less important than the initial stage of growth (Fig. 4.2). This behavior places a practical requirement on the initial interface; it should not be "too perturbed" so that we can still influence the growth of the desired wavelength with our feedback loop. Another method was to grow an initial bubble, observe the dominant moment on the initial bubble, and then choose that moment to grow using the Bataille process.

The withdrawal rates Q_n as a function of $R(t)$ for different mode numbers n are plotted in Fig. 4.3, where the bold stepping line indicates the $Q_n(R)$ used in an ideal experiment with a target mode number $n = 7$ following the Bataille formula. Conventional pumping with constant Q would appear as a vertical trajectory on Fig. 4.3. In practice, the lowest n achievable was 5; the moment amplitude for smaller n grew too slowly to overcome the initial perturbations on the interface before the bubble reached the edge of the cell.

The bubbles grown in these experiments have a nonzero Q during the entire evolution. This is to prevent a bubble from relaxing under surface ten-

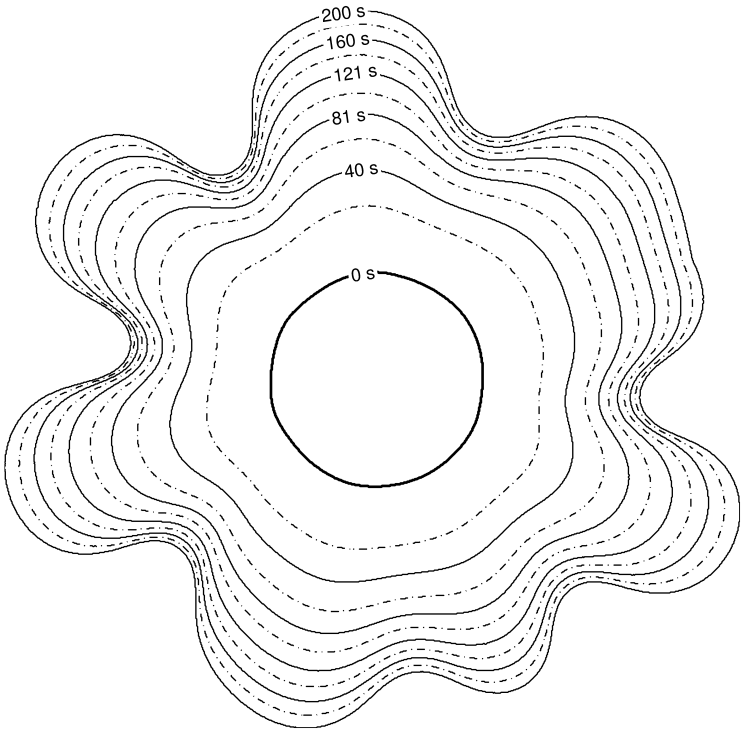

Figure 4.2: An air bubble grown without a clean n-fold symmetry. Adjacent interfaces are separated by 20 s. The pumping rate followed (4.21). The bubble is not symmetric, because during the growth of the initial bubble, the growth rate was such that perturbations with moment numbers other than $n = 7$ were grown faster than moment number n. These unwanted perturbations did not relax in the duration of the experiment. The gap thickness was 384 μm and the maximum bubble diameter at $t = 200$ s was 20 cm. The same growth curve as in Fig. 4.3 was followed, but for different initial and final radii.

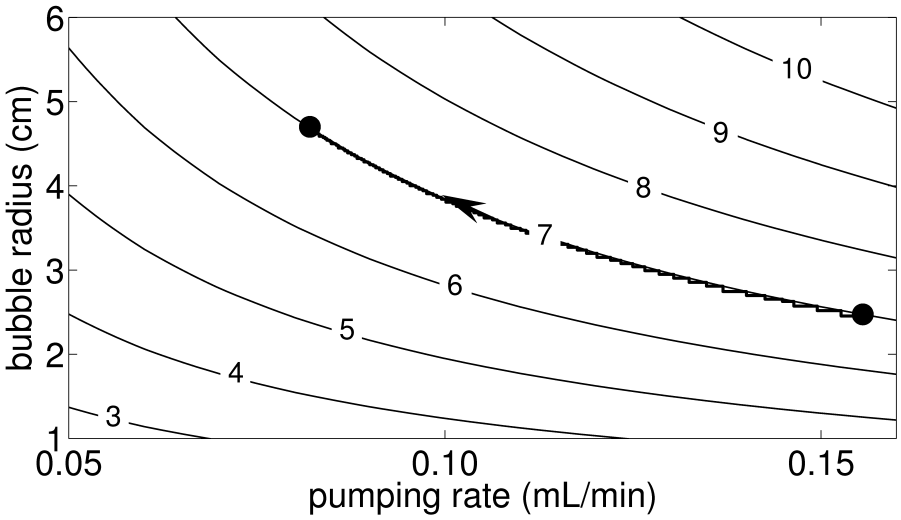

Figure 4.3: The withdrawal rate Q_n changes in time according to (4.21) to grow an n-fold symmetric bubble (solid line). The bold stepping line shows how the pumping rate can be adjusted to maximize the growth rate of 7-fold perturbations, depending on the area of the bubble. The arrow indicates that the bubble's area is increasing in time. The bubble radius is the average radius $R = \sqrt{A/\pi}$ computed from the total bubble area A.

sion to the extent that the interface moves backwards (i.e. toward the center). If the interface reverses direction, it absorbs the wetting film it left behind when it passed that point earlier in its evolution. The bubble moves faster where the film is thicker, and the thickness of that film depends on what speed the interface had at the earlier time. This non-uniform, history-dependent disturbance of the bubble evolution is avoided with the aforementioned nonzero pumping rate.

4.3.3 Image analysis

The interface in each image was first obtained by subtracting the background image, thresholding, and using an edge detection algorithm. This located the interface to within a pixel. The resolution of the air-oil interface was typically 50 pixels/cm, so that one pixel's length was about 0.2 mm.

Then for each image, the position of each point on the interface was obtained with sub-pixel accuracy by interpolating the location along a line perpendicular to the rough interface that was half of the intensity difference between the inside of the bubble (more intense) and the outside of the bubble (less intense). The algorithm typically found a position of half-intensity to 0.1 pixel (about 20 μm).[5] This algorithm for finding the interface was consistent

[5]While the interface looks like a line when viewed from above, it should be noted that the actual interface between the volumes of air and oil exists in three dimensions, because the air bubble is confined in the gap, which was 125.5 or 384.0 μm, much larger than the 20 μm spatial resolution. We chose the position of the interface to be the location of half-intensity as described above. To identify where the half-intensity occurs on the real interface, we would need to calculate what the light profile would look like after the uniform overhead

enough that the data did not require smoothing.

4.4 Results

Figure 4.4 shows a bubble's growing interface and plots the harmonic moment evolution of the same bubble, which was grown in a gap of 125.5 μm. As in all of our experiments, the harmonic moments decay with time. While it is clear that the moments are not conserved, a detailed analysis is needed to decide if the rate of decay of the harmonic moments agrees with the rate predicted in (4.19).

To this end a time integration of (4.19) improves the signal-to-noise ratio in the analysis of the experimental interfaces, because the derivatives in (4.19) amplify the effects of experimental noise. The final formula used to compare our harmonic moments theory with our experiments is

$$M_k(t_2) - M_k(t_1) = \sigma k(k+1)\frac{b^2}{48\mu}\int_{t_1}^{t_2}\oint_\Gamma e^{i\theta}\,\frac{dz}{z^{k+2}}dt \tag{4.22}$$

$$+\sigma k\frac{b^2}{12\mu\pi}\int_{t_1}^{t_2}\frac{3.8\,i}{b/2}\oint_\Gamma\left(\frac{\mu V}{\sigma}\right)^{2/3}\frac{dz}{z^{k+1}}dt \tag{4.23}$$

The time t_1 was chosen when the amplitude of the perturbation from a circle was larger than 3 pixels with the amplitude being defined as

$$a_k = |M_k| * |M_0|^{\frac{k-2}{2}}. \tag{4.24}$$

The time $t_2 - t_1$ was chosen as the time to collect at least 10 useable images, which was at least 5 seconds. This criterion for $t_2 - t_1$ was not as well-defined

illumination is reflected, scattered, and refracted by the air bubble in the silicone oil.

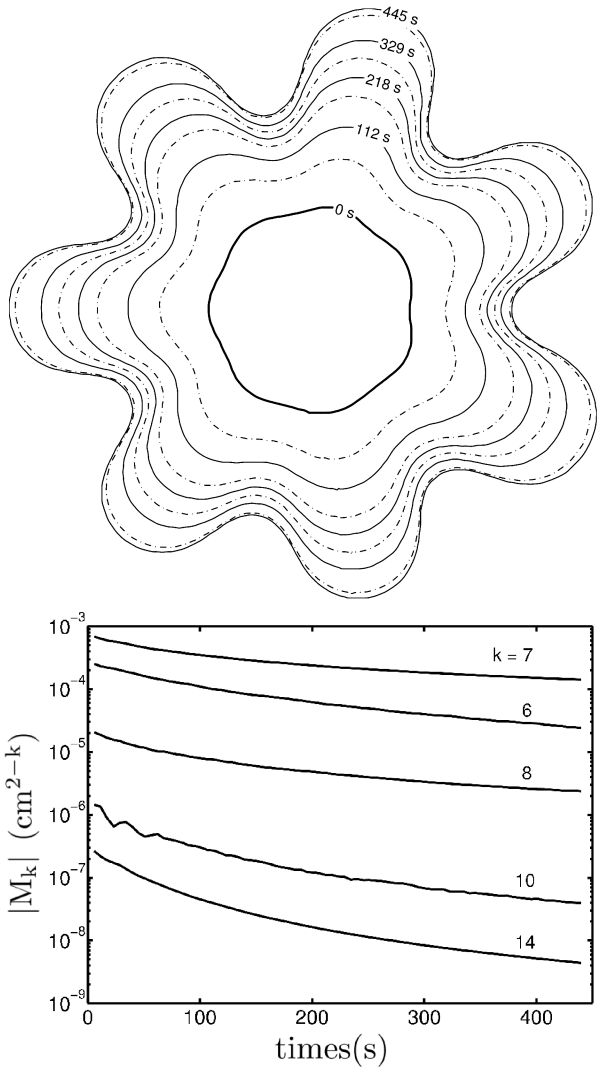

Figure 4.4: Surface tension breaks the conservation of the moments. (a) An air bubble growing in oil within a Hele-Shaw cell. Adjacent interfaces are separated by 55 s. The maximum span of the bubble at $t = 445$ s is 9 cm. The time-dependent pump rate selects the 7-fold symmetry (cf. Fig. 4.3). (b) Amplitudes of moments 6,7,8,10 and 14, computed using (4.24). The units of M_k are cm^{2-k}. Initial conditions set the initial magnitude of each moment. The gap thickness was 125.5 μm.

as the criterion for t_1. If the time $t_2 - t_1$ was too small, the advantage of the time integration would be lost. If the time $t_2 - t_1$ was too large, then time integral would average out any subtle changes in the dynamics of the bubble. However, the result was not sensitive to the choice of $t_2 - t_1$ and the operational criterion was sufficient. The velocity V was calculated by projecting the local normal to the next good interface in time. The use of splines allowed for the intersection to occur between interface data points, so that the velocity could be computed more precisely. Sums over the points of the interface were used as approximations of a contour integral, and sums over the time sequence of interfaces were used as approximations of a time integral. The capillary number $\mu V/\sigma$ of our experiments, which appears in (4.23) was in the range $9 \times 10^{-5} < \frac{\mu V}{\sigma} < 2 \times 10^{-2}$.

The constant system parameters were measured using well developed techniques. We had the surface tension measured by the Wilhelmy Plate (WP) method using a Kruss K11 tensiometer in a commercial lab, we measured the viscosity using a Paar Physica MCR300 rheometer, we know the gap thickness from micrometer measurements of the shim. We call the surface tension resulting from the WP method the reference value of surface tension $\sigma_{reference}$.

We decided to pretend that we did not know the value of surface tension for the silicone oil and try to calculate the surface tension using (4.23). Equation (4.23) is effectively a cubic equation of the form $a\sigma + b\sigma^{1/3} + c = 0$, which was solved numerically for surface tension; we call this number the measured value for surface tension $\sigma_{measured}$. We can then compare the value

measured by the conventional technique in the commercial lab $\sigma_{reference}$ with the value extracted from (4.23) using our experiments $\sigma_{measured}$. The ratio $\sigma_{measured}/\sigma_{reference}$ is an indication of how much of the observed decay in the harmonic moments is accounted for by the theory.

We grew 26 different bubbles with a representative set of different conditions. The two gap thicknesses were 125.5 and 384 μm, one viscosity of 49.9 mPa s, and the extraction rates followed the pumping curves Q_n [see (4.21)] for moment numbers $n = 5 - 14$. For each bubble, Tables 4.1 and 4.2 list the individual experiments and the moment numbers of sufficient amplitude. I want to stress that the special Bataille growth method is not necessary for the harmonic moments description of viscous fingering to be valid; it only makes the results easier to interpret. Figure 4.1(b) shows a nearly symmetric bubble. Figures 4.1(a,d) show bubbles with perturbations of various wavelengths and amplitudes. A spectrum of the harmonic moments present in a bubble can be calculated by using (4.24). A highly symmetric bubble has only a few dominant moments and their integer multiples. For example the bubble displayed Fig. 4.5(a) has significant components of the moments 7, 14, and 21. A bubble with imperfect symmetries has a mixed moment spectrum [Fig. 4.5(b)].

For each pair of images separated by $t_2 - t_1$, we calculated the value of the surface tension using (4.23), thus obtaining anywhere from 50 to 500 measurements of surface tension during one bubble's evolution (Fig. 4.6). If a

Table 4.1: Experiments with a gap thickness of 384 μm

Base Filename	Moment Numbers
d060315_r03	9,10
d060315_r00	6
d060313_r06	6,7,8
d060313_r05	8,9,10
d060313_r04	5,7
d060313_r03	6
d060313_r02	9,11,13
d060313_r01	6,9,11
d060313_r00	6
d060309_r00	6

Table 4.2: Experiments with a gap thickness of 125.5 μm

Base Filename	Moment Numbers
d060307_r03	6
d060307_r02	8,9,13
d060307_r01	5
d060227_r03	11,12,14
d060227_r02	11
d060227_r01	12,14
d060223_r00	10,11,12
d060213_r01	7
d060213_r00	7
d051201_r00	10,11
d051201_r00	9
d051128_r00	8,9
d051122_r01	7,8,9
d051122_r00	9,10,11
d051121_r00	6
d051117_r00	8

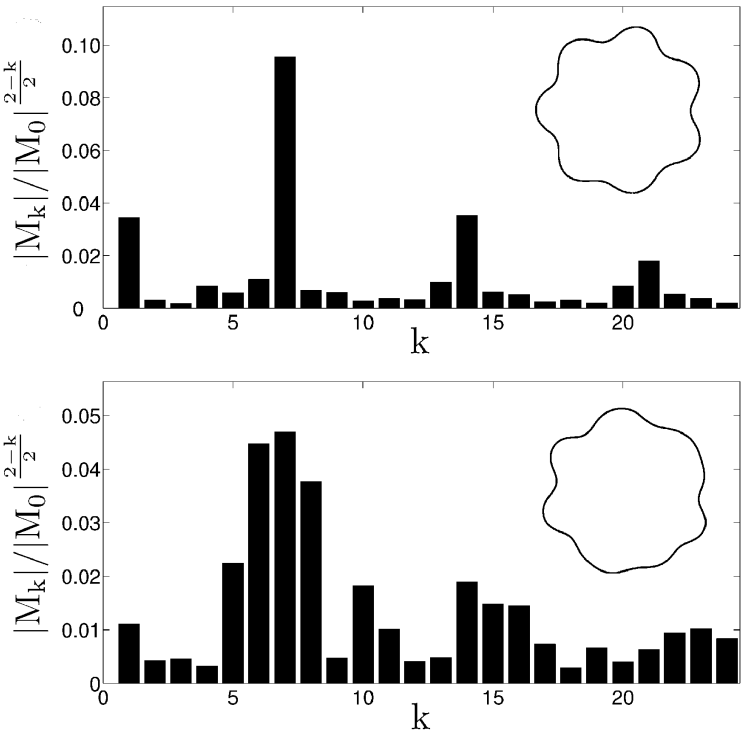

Figure 4.5: Moment spectra for the bubbles on Fig. 4.4 (top) and Fig. 4.2 (bottom) are plotted. One can see how the symmetry of the bubble is represented in the spectrum. For a nearly 7-fold symmetric bubble (top) the spectrum has only one dominant moment number and its integer multiples, unlike the spectrum for nonsymmetric bubble (bottom).

bubble had several moments numbers with an amplitude over 3 pixels, surface tension calculations were performed for all the moment numbers that had a sufficient amplitude. In gathering statistics, every measurement of every experiment is weighted the same.

To determine the contribution of wetting to the dynamics of the oil domain, we computed a value of surface tension $\sigma'_{measured}$, which does not include the effect of the velocity-dependent wetting term in (4.4). The difference between $\sigma_{measured}$ and $\sigma'_{measured}$ depends on the forcing, bubble size and gap thickness of the experiment. In Fig. 4.6, $\sigma_{measured}$ and $\sigma'_{measured}$ differ significantly in the first 100 seconds of the experiment before the wetting correction becomes small due to the decreasing velocity of the interface. This indicates that wetting, while being irrelevant to most Laplacian growth processes, is important for experiments conducted on viscous processes in the Hele-Shaw cell.

For over 6000 measurements on 26 bubbles with dominant moments from 5 to 14, the resulting statistics of $\sigma_{measured}/\sigma_{reference}$ and $\sigma'_{measured}/\sigma_{reference}$ are presented in Fig. 4.7. The histogram is an aggregate of all measurements for all of the bubbles, of which Fig. 4.6 is a particular example. The reference value of surface tension was 21.12 $\pm$ 0.02 mN/m. For the theory without the velocity-dependent wetting correction, $\sigma'_{measured}$ was 23.3 $\pm$ 3.5 mN/m. With the velocity-dependent wetting correction, $\sigma_{measured}$ was 17.8 $\pm$ 1.9 mN/m. The distribution for the surface tension value $\sigma_{measured}$ including the wetting correction has a narrower distribution, because the uncorrected data vary with

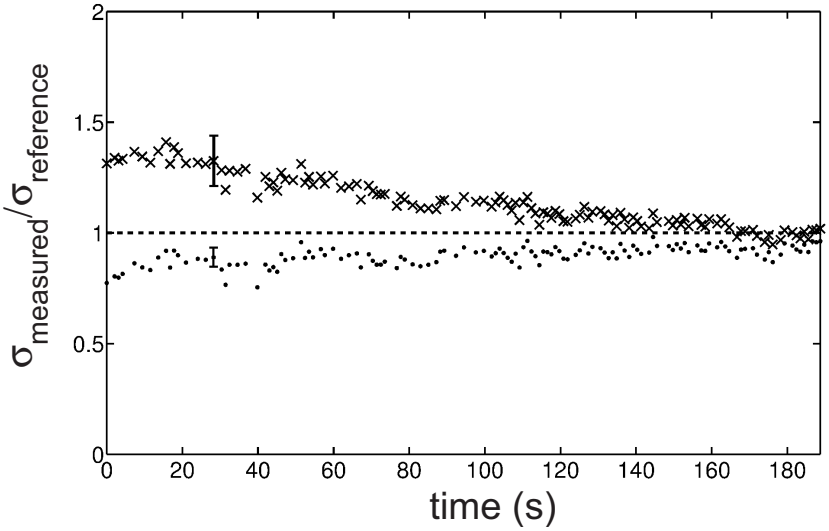

Figure 4.6: Results from one bubble's evolution. The measured surface tension $\sigma_{measured}$ is calculated using image data from the bubble in Fig. 4.2 and the bottom of Fig. 4.5. The abscissa is time t_1 from (4.23). The theory can account for most of the dynamics of the harmonic moments as quantified by the ratio of the measured value of the surface tension $\sigma_{measured}$ and the reference value $\sigma_{reference}$, plotted as a function of time. The analysis is done for the theory with ($\bullet$,$\sigma_{measured}/\sigma_{reference}$) and without ($\times$,$\sigma'_{measured}/\sigma_{reference}$) the wetting correction. The wetting correction is the velocity-dependent double integral of (4.23). The dashed line is the reference value of surface tension normalized to unity. Adjacent interfaces are separated by 20 s. We remind the reader that the actual surface tension itself is assumed to be constant, but the ratios are measures of the theory's accuracy.

the size of the wetting correction. However, it also appears that the velocity-dependent wetting correction term is too large and shifts the distribution to values of surface tension lower than the reference.

Our estimate of the known sources of error from system parameters is 8%. The main sources of error are the measurements of the gap thickness, the oil viscosity, and the image scaling. Other possible sources of error not included in the estimate are the discretization of the integrals and derivatives and a known camera synchronization problem. Another intriguing possible source of error is the 3.8 factor in the Park and Homsy wetting correction term [101], which has its origin in a numerical integration done by Ruschak [119].

Bubbles in the experiments presented have had non-zero pump rate Q at all times. An alternative condition is to allow the bubble to undergo pure relaxation (Q=0) after an initial period of unstable growth. We conducted experiments of this kind and found that the extracted surface tension from pure relaxation yields a value consistently lower than the reference value $\sigma_{reference}$ by 15% to 25%. We emphasize that the actual value of the surface tension of the silicone oil is the same in the experiments, but the extracted surface tension we report is a composite measure of how well the theory describes the interface dynamics. We suspect that because the interface travels backward during the relaxation process, the wetting film has been absorbed and has effected the dynamics significantly. The optimal pumping conditions are then slow enough for the wetting correction to be small and fast enough for the

relaxation process to be prevented.

The reference value of surface tension $\sigma_{reference}$ lies within 16% of both $\sigma'_{measured}$ and $\sigma_{measured}$. This result is strong evidence that the theory presented in this paper successfully accounts for the observed decay in the harmonic moments within our measurement uncertainty. By deduction, for the case of zero surface tension, the moments would be conserved quantities within uncertainty.

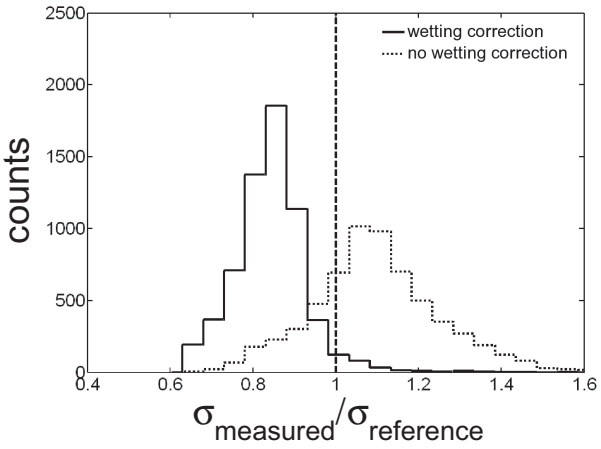

Figure 4.7: A distribution of surface tension extracted from the theory divided by reference value is plotted. The histogram includes over 6000 measurements taken from the growth sequences of 26 bubbles. Each bubble had one or more dominant moments ranging from 5 to 14. Solid line represents the computations carried taking in account the wetting term, dotted assuming there is no wetting in the system. The bin size is 0.05. A few outlying points are outside of the abscissa's range.

4.5 Discussion

Harmonic moments M_k form a complete basis for a complicated time-dependent domain D, provided that D is analytic and singly connected. We have made the first demonstration that harmonic moments evolve in time because of the nonzero surface tension; otherwise all moments (but M_0, the area) would be conserved. This work is the first laboratory determination of harmonic moments and their dynamics. The harmonic moment description of Laplacian growth pattern dynamics including surface tension has been experimentally confirmed. Surface tension values deduced from the dynamics of the harmonic moments are within 16% of independently determined values. This result is robust and does not depend on n, the bubble symmetry, or how far the bubble has deviated from a circle.[6]

Use of the Bataille formula to adjust the pumping rate $Q_n(t)$ enables one to grow a nearly n-fold symmetric bubble. We find that if an n-fold bubble is grown initially from a slightly perturbed circle, the n-fold symmetry is retained even for large amplitude fingers, far beyond the range of the applicability of Bataille formula, which was obtained from a linear stability analysis (an analysis of infinitesimal perturbations).

We believe that the harmonic moment interface representation is important in light of the theoretical progress in the field of growing interfaces. Because Laplacian growth patterns evolve to a fractal with universal character-

[6] Although tested for large deviations from a circle, the theory was not tested for patterns with multiple generations of fjords.

istics (indistinguishable from those obtained in diffusion-limited aggregation [86]), we believe that a great challenge in the elucidation of the geometry in long-time asymptotics of Laplacian growth is to know the behavior of the moments M_k in the long-term limit. To this end, it would be interesting to conduct the same measurements on other secondary tip-splitting instabilities, such as in electrodeposition and bacterial colony growth.

Chapter 5

Pinch-off in a Hele-Shaw cell

5.1 Background

This chapter presents previously unpublished tests of two theoretical predictions for flows in a Hele-Shaw cell involving the break-off process of fluid domains.[1] For a connected volume of fluid to divide into two separate volumes of fluid, the interface of the original volume must rupture. This process is called pinch-off and occurs in liquid drops [1, 27, 35, 38, 40, 62, 128, 152], gas bubbles [12, 20, 65], and crystals [59]. The field is over a hundred years old and the array of work is staggering, which is reviewed in [37]. Most commonly, pinch-off is driven by surface tension (and is called capillary pinch-off), but pinch-off can also be driven by other mechanisms, such as viscous forces. The opposite process of two volumes merging to form one volume is called coalescence [23].

In viscous fingering, the existence of surface tension prevents the interface from developing finite-time singularities, such as cusps. In our experiments on viscous fingering, the process of pinch-off was avoided by limiting the forcing as it could affect our measurements of the fractal dimension (Sect. 3.2)

[1] This chapter is based on work of Brooks Campbell, which lead to an award-winning Undergraduate Honor's thesis [21]. While Harry Swinney and I guided Brooks on these two experiments, he did the overwhelming majority of the work.

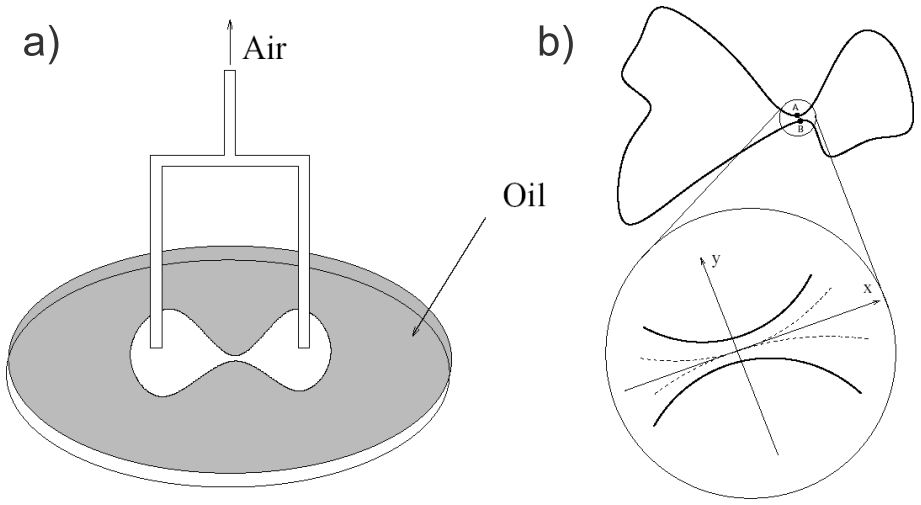

Figure 5.1: (a) The pinch-off process in a Hele-Shaw cell with two inlets. An air domain is about to pinch-off. (b) Close-up view of the pinch-off region with the coordinate system discussed in Sect. 5.3. Adapted from Lee, Bettelheim, and Wiegmann [76], used with permission.

[86, 108, 118].

Bubble pinch-off is the process of a bubble of a less viscous fluid surrounded by a more viscous fluid separating into two bubbles (Fig. 5.1). The pinch-off process exhibits a singularity when the thin neck of the bubble breaks. After pinch-off, the retraction of the air domain is stable, since the more viscous fluid is pushing into the less viscous fluid. Despite the long history, recent mathematical analyses have predicted surprising results, which if they are observed, would connect a large body of mathematics to the physical world.

5.2 Apparatus

A square Hele-Shaw cell was built to conduct quasi-two dimensional fluid experiments (Fig. 5.2) and was based on the suggestions of Lee *et al.* (Fig. 5.1). The two plates were made of acrylic, so they were easily machinable and the interface between two fluids could be imaged with a CCD camera from above. The plates were separated by metal shims. Two holes were drilled in the bottom plate so that fluid and air could be injected and withdrawn in the thin space between the plates. Experiments were conducted with air and 103 mPa s silicone oil. A series of tubes, valves, syringes, and syringe pumps determined the location, rate, and direction of fluid flow. Clamps held the two plates down to maintain the thickness of the gap. A reservoir of fluid surrounds the thin gap so that the pressure at the edge of the entire cell is nearly the same. The size of the reservoir was chosen so that the pressure drop from fluid flow in the reservoir was much smaller than the pressure drop in the gap. An O-ring around the reservoir sealed the fluid in between the plates. The fluids are lit from below with an array of LEDs behind a diffusive, transparent plastic panel. The scaling in the square cell was either set by the diameter of the inlet valve's nut or calibrated using grids. For a detailed description and machine drawings, see Campbell's thesis [21]. The radial Hele-Shaw cell described in Chapter 1 was also used for experiments.

A Phantom brand high speed camera recorded the dynamics at 200-1000 frames per second at a resolution of 512 by 512 pixels. A typical image of an air bubble in the oil layer is displayed in the left image of Fig. 5.3.

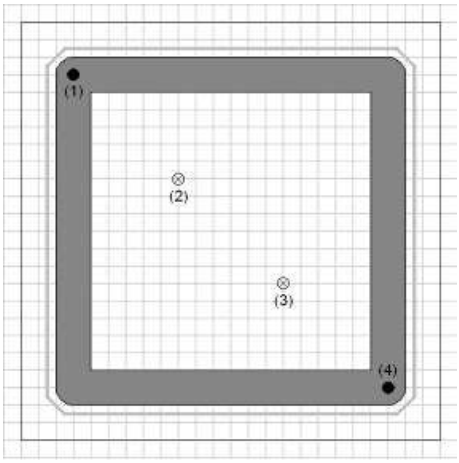

Figure 5.2: The square Hele-Shaw cell, 30.5 cm on a side. The plates are separated by 1.0 mm. The gray area is the 2.5 cm deep reservoir. The inlets (1) and (4) are in the reservoir and the inlets (2) and (3) are in the gap. Reprinted with permission from Campbell's thesis [21].

An algorithm was developed by Brooks Campbell for extracting the pixels corresponding to the interfaces. The interface points extracted from the image are highlighted in the right image of Fig. 5.3.

5.3 Pinch-off in a Hele-Shaw cell

Based on the work of Richardson, Lee *et al.* have predicted that the shape of an inviscid bubble breaking into two bubbles while surrounded by viscous liquid is self-similar and universal [76, 114]. This means, respectively, that each interface near the pinch-off region can be rescaled to a common functional form and that the initial global shape of the bubble does not influence the shape of the pinch-off region. The same result is a solution of the dis-

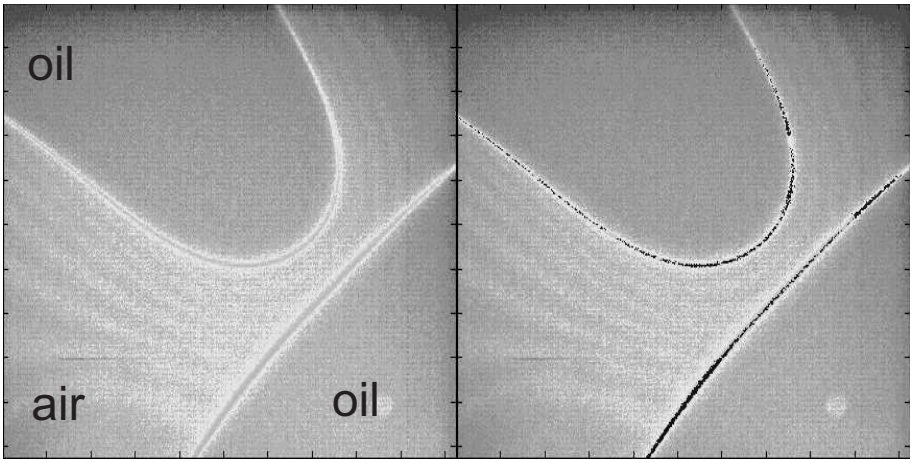

Figure 5.3: Left: An experimental image of the approaching interfaces. The field of the image is 2.8 mm wide. This image was taken in the radial cell with a gap thickness of 125.5 μm. Right: The dark dots are the points of the interface identified by the algorithm. Reprinted with permission from Campbell's thesis [21].

persionless limit of the ANKS hierarchy, using the mathematics of harmonic moments, the Cauchy transform, and the Schwarz function [76]. If this theorized connection between mathematics and the physical world was verified, further work could provide a better understanding of nonlinear and integrable phenomena. While the process of pinch-off is very common in manipulating fluids and bubbles, the conditions required for self-similarity are specific. We propose to test these predictions in carefully controlled experiments in a Hele-Shaw cell.

Before pinch-off, Lee *et al.* predicted that the interface's shape [sketched

in Fig. 5.1(b)] will be

$$y = x^2 (\pm a + c) + t (\gamma \pm 1), \tag{5.1}$$

where x and y are spatial coordinates with dimensions of length, time t has dimensions of length, a and c are the constants with dimensions of inverse length that define a parabola, and γ is the dimensionless drift constant. This equation appears in Lee *et al.* [76] as Equation (26). Pinch-off happens at $t = 0$. Equation 5.1 defines two curves, which correspond to the upper and lower curves of the interfaces to merge. The theory makes several assumptions:

1. surface tension is zero and the flow is dominated by viscosity,
2. the flow is two dimensional,
3. the air domains are at the same pressure (even after pinch-off).

A procedure to find the constants a, c, and t from experiments was developed with the assistance of Eldad Bettelheim. At the instant of pinch-off ($t = 0$), the two interfaces are approximated as parabolas. The two constants a and c are chosen such that both interfaces are well described by $y = x^2(\pm a + c)$. Then as the interfaces approach each other, the shortest distance between the two interfaces is $2t$. The extracted volume of air T is linearly related to the separation distance t

$$T = A + Bt, \tag{5.2}$$

where A and B are constants. This prediction that the interfaces approach linearly is a result from the theory, given that the length scale of the pinch-off

is much smaller than the length scale of the bubble. Since time is measured as a distance, the drift velocity γ is dimensionless.

After pinch-off ($t < 0$), the predicted shape is

$$y = x^2 \left(a\sqrt{1 + \frac{2t}{ax^2}} + c + \gamma \frac{t}{x^2} \right). \tag{5.3}$$

The constants a, c, and γ are the same before and after pinch-off. This equation appears in Lee *et al.* [76] as Equation (27).

All the curves after pinch-off collapse to a self-similar form

$$Y = X\sqrt{2 + X^2} + CX^2 + \Gamma, \tag{5.4}$$

where $Y = y/t$, $X = x\sqrt{\frac{a}{t}}$, $C = c/a$, and $\Gamma = \gamma$. Each of the new rescaled variables are dimensionless. After pinch-off, the linear relationship between the tip separation and time is relaxed, but the same A and B apply when changing extracted volume T into the time t of (5.2).

5.3.1 Preliminary experiments

We attempted experiments in both the square and the radial Hele-Shaw cells. The Hele-Shaw cells approximate two dimensional flows. Air has a viscosity $\mu = 0.018$ mPa s, which is much less viscous than the silicone oil of viscosity $\mu = 103$ mPa s. So the fluids approximate the inviscid and viscous domains of the theory. In this way, the second and third assumptions of the theory are approximated. A few preliminary results obtained in the radial cell are presented here. The experiments in the square cell still have some

issues to resolve before reliable data can be taken reproducibly, as discussed in Sect. 5.3.2.

Previous theoretical studies of pinch-off most commonly deal with three dimensional, rotationally symmetric situations. While this study was initially thought to study two dimensional pinch-off, the experimental parameters we have tested so far do not exhibit pinch-off until the size of the neck width approaches the gap thickness b. At times close to the actual pinch-off event, the third dimension cannot be neglected. It is hoped that a careful choice of experimental parameters would allow the interface's dynamics approaching pinch-off to be two dimensional for some time, even if the dynamics inevitably become three dimensional.

Another condition of the theory is that the two bubbles of air must be at the same pressure at all times, so we connected the inlets to the gap to the same air reservoir, as in Fig. 5.1. The paper of Lee *et al.* calls for the air to be removed, decreasing the area of the bubble until it pinches-off. However, instead of driving the bubble in this fashion, we decided use the radial cell and inject air and then inject oil. This grew an annulus of air which became thinner and thinner as more oil was injected. Finally the annulus became unstable, and the interior and exterior interfaces of the annulus merged to form a single, crescent shaped bubble of air (Fig. 5.4). This experiment did not yield satisfactory data, since the region that changes as pinch-off occurs is too small to be resolved with our optics. In this case, only the global dynamics are observed, and no local, self-similar dynamics are observed.

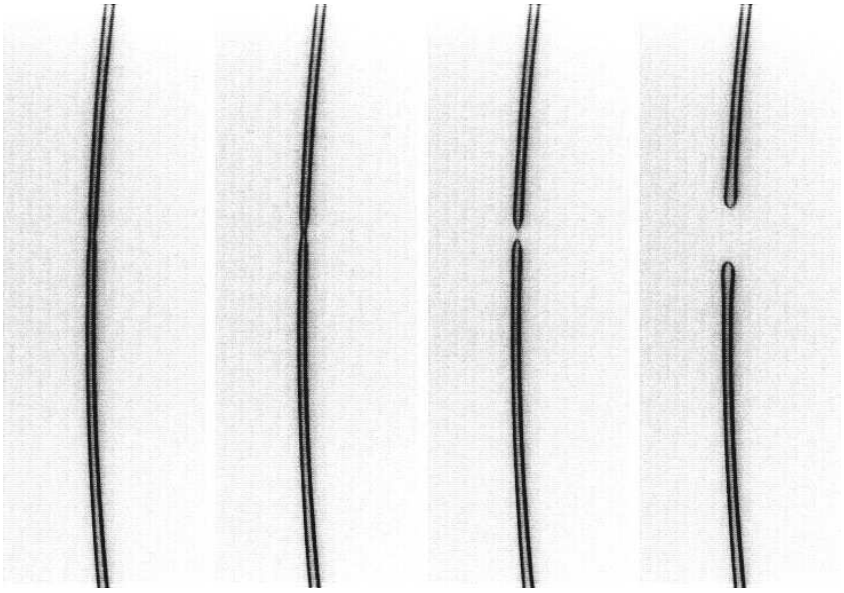

Figure 5.4: Pinch-off of a thin annulus of air in the radial cell. The gray background is silicone oil. Each frame is 0.73 cm tall. The relative times between images are 0, 12, 16, and 32 ms.

For a later set of experiments in the radial cell, we injected air into the oil layer and grew a viscous fingering pattern with a few fingers and no tip splitting beyond the initial instability. Then we injected oil and grew a stable oil domain inside of the viscous fingering pattern. This produced a set of interfaces with curvatures more appropriate for imaging. The interfaces extracted from this experiment are shown in Fig. 5.3. The radial cell has a much better defined gap thickness and uniformity than the square cell. Figure 5.5 is a comparison of data and theory.

It is observed that before pinch-off, the interfaces simply translate toward each other. The interfaces are self-similar, but in a trivial manner. After pinch-off, the interfaces do not have the shape predicted by the theory. Moreover, no scaling law has been found to describe all of the experimental interfaces. This is not strong evidence against the existence of the scaling regime, rather it probably indicates that our experimental parameters do not meet the criteria necessary for the theory to be predictive. It is thought that this is because these dynamics are dominated by surface tension and not by the viscous flow, as the pumping rate is low. However, this suggestion has not been confirmed either.

5.3.2 Next steps

For a complete experimental test of the predictions of Lee *et al.*, there are several experimental parameters to change and several issues to resolve. In the radial cell experiments, the pumping rate and surface tension should

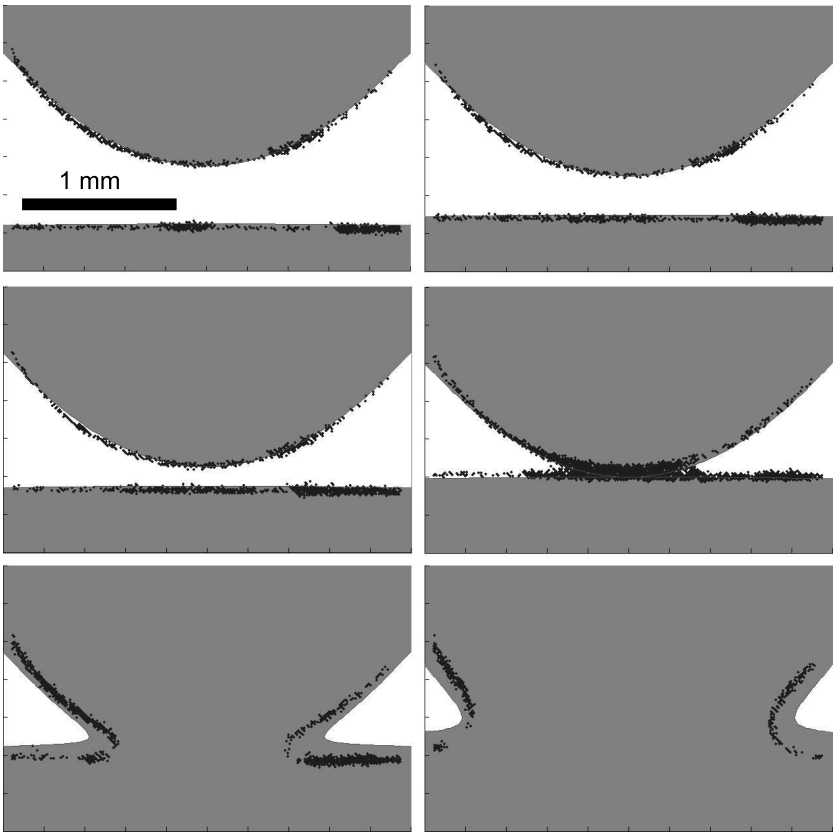

Figure 5.5: Experiments match the theory well only before pinch-off. After pinch-off, there are significant deviations. The oil domain is gray and the air domain is white. The boundary between the areas shaded gray and white is the predicted interface between the oil and air domains. The interfacial points are data extracted from the experiment. The times relative to pinch-off for the images are -0.9, -0.6, -0.3, 0, 0.3, and 0.6 s. Adapted from Campbell's thesis [21], printed with permission.

be varied so that the flow can be varied through the full range from surface tension driven to viscosity driven.

An expression relating the experimental parameters to the relative strength of surface tension and viscosity would be most helpful. The capillary number $\mu V/\sigma$ would be a good place to begin, but more work would need to confirm its usefulness. For example, increasing the viscosity μ would also decrease the velocity V for a given pressure difference Δp. If the viscosity μ was increased and the pressure difference Δp was increased to keep V constant, then we would expect the flow to become more dominated by viscosity. A smaller gap thickness b would prevent pinch-off until the interfaces were very close, since we observed that the interface did not pinch-off until the interfaces are separated by a distance on the order of b. A smaller b would also decrease V for a given pressure difference Δp, so this change in expected to make the viscous forces less dominant.

The next step would be to use two fluids with a smaller surface tension than air and silicone oil. For example, perfluorohexane (CAS Ref. No. 355-42-0) has a surface tension of 12 mN/m at 20 °C in air and is relatively safe to work with. However the viscosity of the perfluorohexane would need to be increased (such as with glycerine) to maintain a large viscosity contrast between the two fluids. This would probably then increase the surface tension. The compatibility and solubility of these fluids would need to be checked to ensure a safe experiment. Surface active chemicals could be added to lower the surface tension. The tension between water and carbon dioxide can be changed

from 20 mN/m to 2 mN/m by adding surfactants [31]. Two liquids could also be used to lower the interfacial tension. For instance, water and octyl alcohol have an interfacial tension of 8.5 mN/m at 20 °C [147]. The surface tension and viscosity of most liquids decrease with increasing temperature. If the surface tension decreases more quickly than viscosity, then a heated liquid might be a possibility for making viscosity more dominant. Finally, silicone oils wet the glass plates completely. To change this, the glass plates could be coated or different fluids could be used that wet the plates differently.

In the square cell, the most important problem is that there is no reliable method to connect the air bubbles of the two inlets. Moreover there is no method to produce a pinch-off event in a reproducible location. Ideally, the pinch-off could occur in a predictable place so that the camera can be zoomed to high magnification. If the gap thickness was much smaller in a particular region, then perhaps pinch-off would happen there preferentially. This might change the dynamics of the pinch-off and the smaller gap would be more difficult to bridge an air bubble across it to initialize the experiment. Overall the parameters have complicated dependencies and changing a parameter can have unexpected consequences.

Another issue in the square cell is that air and oil are often held in the same pipe, making the experiment only sporadically successful. This could be solved by pumping oil from the reservoir and by having the inlets to the gap layer open to the atmosphere, draining by gravity to a dish below the lighting panel. If this was done, the LEDs and electrical connections would need to be

protected from the draining oil. Finally the uniformity of the gap thickness should be verified with interferometry. The uniformity of the rectangular and radial cells were confirmed by counting the interference fringes produced by the light of a sodium lamp.

5.4 Richardson's "soliton"

In two papers published in 1996, S. Richardson presented an counter-intuitive theoretical result: a region of oil absorbed by a moving oil domain with finite length would cause another region of oil to be deposited in its original location after the moving oil domain had passed by [115, 116]. Figure 5.6 shows such an event in the radial geometry. An example of Richardson's "soliton" in the rectangular geometry appears in Fig. 5.7 [115]. The result came from a functional approach to Laplacian growth of multiply-connected viscous oil domains, assuming zero surface tension. Mark Mineev-Weinstein helped us by modifying, interpreting, and applying Richardson's work to our experiments.

In a sense, the two oil domains passing through each other are solitons, because they are localized objects that interact without changing shape. Otherwise they are not like solitons, which have more special conditions and properties. Despite the zero surface tension assumption, if experiments would exhibit these phenomena in some parameter range, the work could readily be applied to the extraction of oil from underground reservoirs. Often gas and liquid are injected repeatedly during secondary and tertiary recovery [71], which

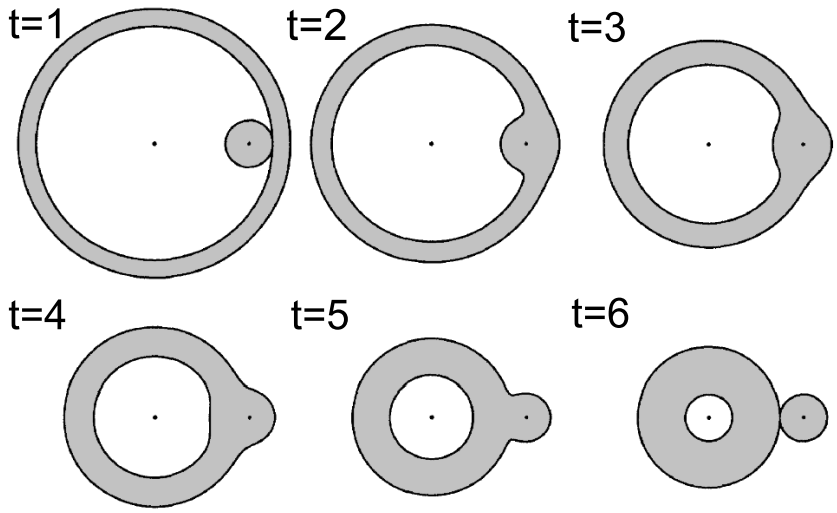

Figure 5.6: Air is withdrawn from the left dot. Regions of oil are shaded gray and inviscid regions are white. The droplet of oil centered on the right dot (an injection port used to grow the oil droplet) is initially inside of the annulus. The droplet is absorbed and then subsequently disgorged by the annulus of oil. The label t gives the order in time. Adapted from Richardson [116], used with permission.

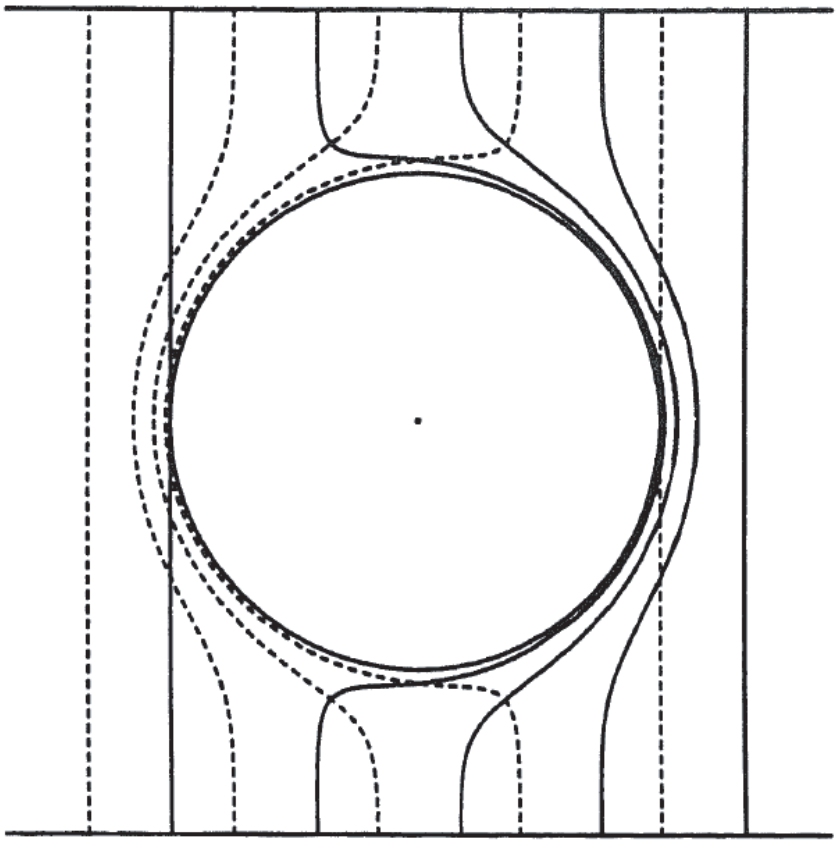

Figure 5.7: A rectangular oil domain absorbs and disgorges an oil droplet. The left-hand and right-hand free boundaries are drawn as dashed and solid lines, respectively. The dot marks the center of the oil drop. Reprinted with permission from Richardson [115].

are attempts to free oil that is trapped in the porous rock. These pumping schemes could lead to situations where domains of oil are absorbed and then disgorged, which would leave behind substantial quantities of oil.

We should be aware that even Richardson thought the experiment would be difficult [115]:

> A final note of caution is, perhaps, called for. Our analysis concerns an idealized model of the motion taking place in a Hele-Shaw cell, the most contentious assumption probably being that of constant pressure along a free boundary. This is generally regarded as appropriate for a hypothetical situation where surface tension is generally zero, but in a real situation with non-zero surface tension this feature *must* become significant as any configuration involving a cusp is approached, no matter how small the relevant surface tension parameter may be. The inclusion of a non-zero surface tension into the theory would almost certainly have important consequences for the phenomena illustrated in the examples, and it is not clear whether a convincing demonstration of these phenomena could be given in an experiment.

Acknowledging this warning and accepting the challenge, we knew to study the predicted absorption and disgorging phenomenon for a wide range of experimental fluid parameters was necessary. The most important parameters are the surface tension, viscosity, and wettability. Other parameters to vary include the gap thickness, initial conditions, and the sizes of the oil domains. The relative influence of viscosity and surface tension can be expressed as the

capillary number, $Ca = \mu V/\sigma$. For immiscible fluids, the pumping rate could vary the capillary number, but the capillary number would remain finite. Surface tension introduces qualitatively different behavior (even if it is very small), because it is a singular perturbation meaning that the limit of surface tension going to zero is *not* the same as surface tension being zero. Miscible fluids are usually considered as having no surface tension, but there is evidence that there does exist an effective surface tension between two miscible fluids [106]. It is clear then that the experimental parameters must be varied widely and carefully chosen. If the same engorging and disgorging phenomena exist for nonzero surface tension, we will attempt to identify the mechanism.

Preliminary experiments were undertaken. First a field of small oil droplets was prepared by rapidly injecting air into the oil-filled gap. Then a quantity of oil was injected, followed by air, which produced an annulus of oil. As more air was injected, the annulus expanded and collided with the oil droplets. If the experimental parameters meet the conditions of the theoretical prediction, then oil droplets are expected to be deposited where the original oil droplets were located. Figure 5.8 shows one such experiment, and the bubbles absorbed by the oil annulus are not disgorged.

Figure 5.9 illustrates the problems I suspect will prevent the phenomena with nonzero surface tension. Figure 5.9(a) is a sketch of a strip of oil approaching a oil droplet. The strip of oil could be part of a larger annulus of oil or it could be confined between the two parallel walls of the rectangular Hele-Shaw cell. As the strip approaches, the oil drop is stationary because the

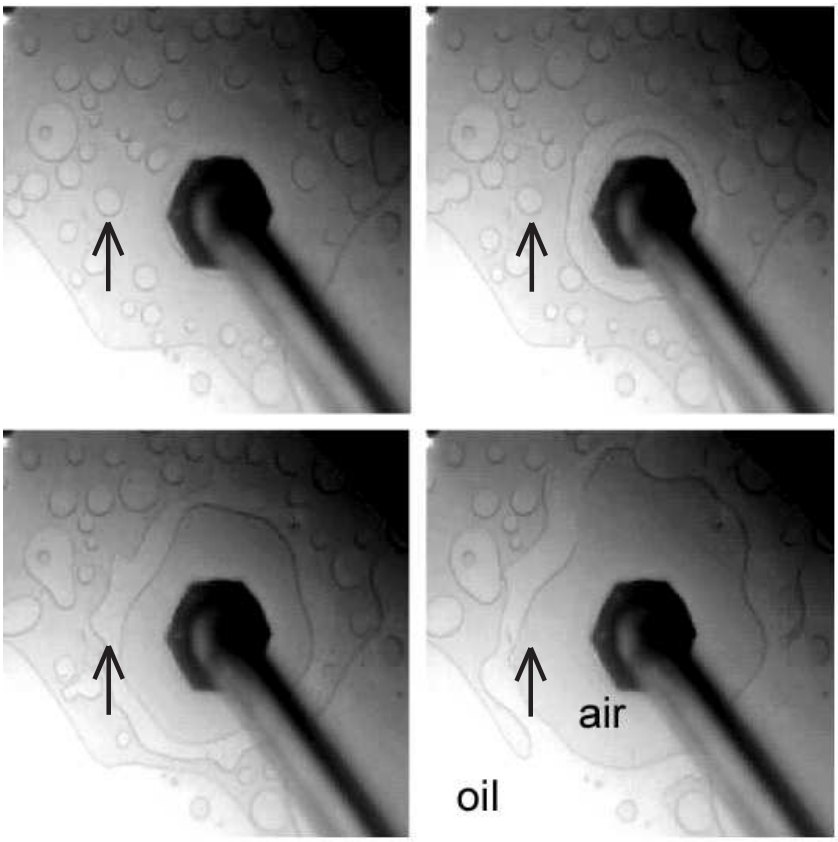

Figure 5.8: A sequence of images showing air being injected to drive an annulus of oil. As the annulus grows, it absorbs drops of oil, but does not deposit any oil. The arrow identifies the absorption of a single oil droplet that is not later disgorged. The arrow remains in the same relative location in each image. The total injected volume was 4.2 cm^3. The pumping was done by hand in this experiment. The gap thickness in this experiment was 1.0 mm. The maximum diameter of the hexagonal nut in the image is 1.42 cm. The time between images was 2.5 s. The silicone oil viscosity was 103 mPa s. Data taken by Brooks Campbell.

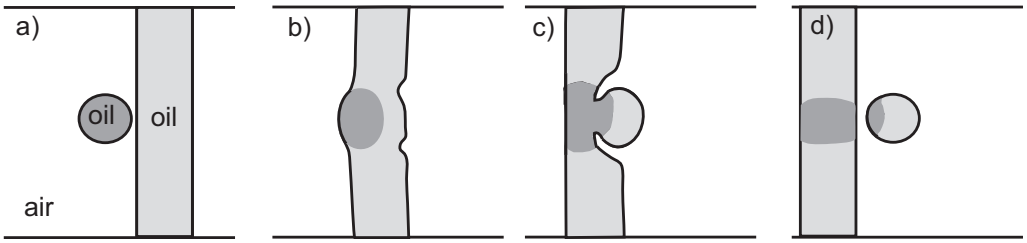

Figure 5.9: My interpretation of the absorbing and disgorging of a oil drop is used to point out potential reasons why nonzero surface tension would prevent the disgorging of a drop. (a) A strip of oil advances toward a drop of oil. (b) As the drop is absorbed, two fingers begin to grow on the back interface. (c) The fingers grow toward each other as the drop to be disgorged forms. (d) The fingers meet, separate the new oil drop, and the back interface flattens out.

nearly inviscid air around it equilibrates the pressure on the drop's interface. Once the drop merges with the moving strip of oil [Fig. 5.9(b)], the bump on the front of the drop will flatten, because the interface propagation is stable when more viscous fluid enters less viscous fluid. The back interface is unstable though, and for the drop to be disgorged after the strip passes, two fingers of air need to begin to grow. As Fig. 5.9(c) shows, the fingers of air must come together for the bubble to be disgorged. The same pressure difference that drives the strip of oil forward could grow fingers on the unstable back interface. However, it is not clear what drives the tips of the fingers together. In all of our other experiments, the tips competed and shielded the gradient from each other. There is no apparent source of a gradient between the tips, which would be required for them to come together and form the new droplet. The same problem exists in finding a mechanism that is compatible with the

presence of surface tension for the fingers to finally meet and separate the bubble from the strip [Fig. 5.9(d)]. I suspect that if the two fingers formed in the correct place, the strip of oil would be broken by one of the fingers of air. The pressure gradient driving the strip of oil would also drive the finger of air to the strip's front interface and not drive the two fingers together. I think only one of the fingers would make it to the front because the two fingers would compete, and whichever finger was slightly ahead of the other would win. Finally, after the droplet has been disgorged, the unstable back interface must straighten. How this occurs without surface tension is not intuitive. For it to occur with surface tension, the surface tension would have to dominate over the strip's driving force, but this would possibly preclude the formation of the initial two fingers of air in the first place. At this point, this is good news for oil recovery, since no oil drops were observed to be left behind. Further experiments at other conditions (especially with miscible fluids) are necessary for testing this prediction completely.

Chapter 6

Bouncing jet

Our work on the bouncing jet has been published as "Bouncing jet: A Newtonian liquid rebounding off a free surface" in *Physical Review E* with me, Sunghwan Jung, Yee Kwong Pang, Chih-Piao Chuu, and Harry L. Swinney [136], which grew from a Master's research project [135]. These can be downloaded at `http://arxiv.org/abs/0707.1721` and `http://chaos.ph.utexas.edu/research/fluids/Thrasher_MA_Thesis.pdf`. Supplemental information follows.

6.1 Newtonian viscosity

Careful measurements of viscosity as a function of shear rate were made with a Paar Physica MCR300 rheometer.[1] Figure 6.1 shows my measurements of dynamic viscosity for silicone oils rated with nominal kinematic viscosities of 50 cS, 100 cS, 200 cS, 350 cS, 500 cS, and 1000 cS. All measurements were controlled at a temperature of 22 °C, because our collaborator Yee Kwong Pang observed that a temperature change of 1 °C in the bath changed the

[1] We wanted an equally precise way to measure surface tension, but it was decided that it was better to pay a commercial lab to measure our limited number of samples instead of buying the equipment.

boundary of the bouncing regime by 1-2%. For 1000 cS ($\approx$ 1 Pa s) above 3500 s^{-1}, the fluid began to be spun out from between the cone and plate, and so the measurements were not valid there.

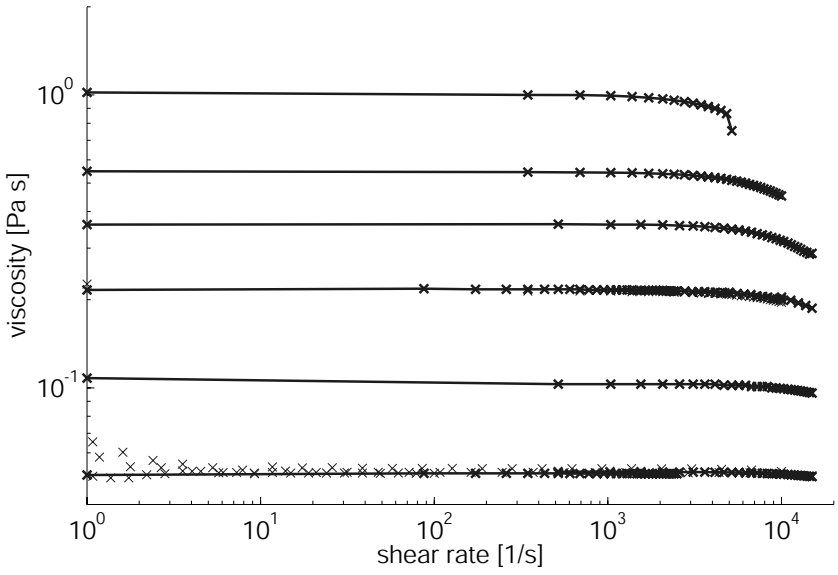

Figure 6.1: Dynamic viscosity as a function of shear rate for silicone oils with nominal viscosity of 50, 100, 200, 350, 500, and 1000 cS.

Silicone oil was a convenient liquid to use since it stayed clean and came in a wide range of viscosities, but the bouncing jet occurs in fluids other than silicone oil. Table 6.1 lists some conditions for the bouncing jet in several common fluids. For many more fluids and conditions, see my Master's thesis [135]. Figure 6.3 shows the measurements of dynamic viscosity at 22 °C for mineral oil, motor oil, canola oil, and a 1:10 solution of dish soap and water.

Figure 6.2: A solution of soap and water bouncing. The solution was one part dish soap and ten parts water. Conditions: $V_{bath} = 15 \pm 1$ cm/s, and $H = 2$ cm. The nozzle diameter was 0.1 cm, and the field of view is 6.4 cm. The exact flow rate and liquid viscosity are not known, but the viscosity was approximately 1 mPa s. This picture was taken by Yee Kwong Pang, used with permission.

Table 6.1: Some common fluids with typical parameters* for bouncing.

Fluid	Viscosity mPa s	Nozzle Height cm	Flow Rate cm^3/min	Bath Velocity cm/s	Bath Depth cm
canola oil	64±1	3	50	14	4
10W-40 motor oil	250±4	5	30	17	3
heavy mineral oil	175±2	6	50	10	4

*Typical parameters for bouncing are meant as guidelines. To find the range of parameters where the bounce is most stable, the parameters should be varied over a wide range.

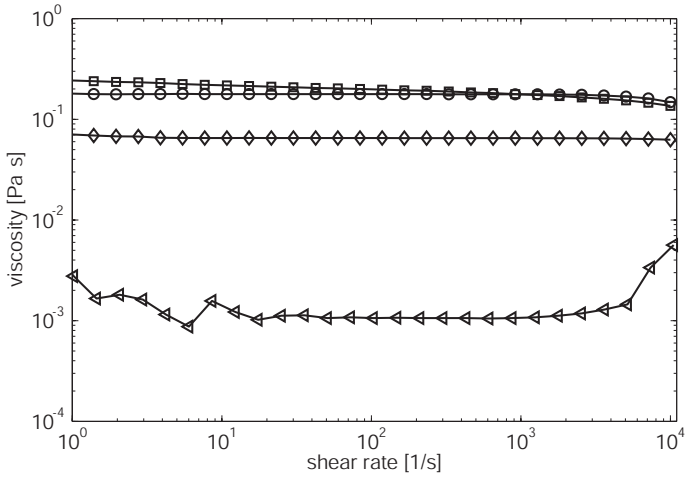

Figure 6.3: Dynamic viscosity as a function of shear rate for mineral oil (○), 10W-40 motor oil (□), canola oil (◊), and a 1:10 solution of dish soap and water (◁).

For the soap solution above 4000 s^{-1}, the fluid began to foam and be spun out from between the cone and plate, thus those measurements are not accurate.

In our experience, water and mixtures of water and glycerine were not observed to bounce without surfactants. Observations suggested that the large surface tension of water and glycerine pinched the air film into bubbles too quickly to form a stable air film. Water jets plunging into baths of water have been studied before [13, 39], but our collaborator Yee Kwong Pang observed a solution of water and detergent bouncing (Fig. 6.2). It is unknown if the non-Newtonian properties of the solution play a role in the bouncing.

6.2 Velocity lost

During the bounce, the jet and the bath are separated by a thin layer of air. Although the air lubricates the relative motion between the two bodies, the jet does lose energy and slow down. The energy dissipated in the jet's interaction with the surface was measured by comparing the velocity of the jet before and after bouncing off the surface.

The velocity V_{jet} can be measured from the jet diameter d_{jet}

$$V_{jet} = \frac{4Q}{\pi d_{jet}^2}, \tag{6.1}$$

where Q is the jet's flow rate. However, this method is inaccurate because the resolution of images only gives the diameter of the jet to 4%. A more accurate method is to measure the height $H_{rebound}$ and the horizontal distance D_{range} that the jet rebounds. Simply because these distances are much larger, they can be measured to 1% or better. From these two measurements and the assumption that the jet undergoes free fall, the measured velocity V_m and the measured angle of rebound θ_m can be approximated as

$$V_m = \frac{\sqrt{2gH_{rebound}}}{sin(\theta_m)} \tag{6.2}$$

$$\theta_m = tan^{-1}(4H_{rebound}/D_{range}). \tag{6.3}$$

The angles here are measured from the horizontal axis.

We will examine the rebound velocity of the jet for a flow rate Q from 0.18 cm^3/s to 0.54 cm^3/s, a bath velocity V_{bath} from 0.66 cm/s to 7.87 cm/s, a viscosity of $\mu = 349$ mPa s, a falling height $H = 3.0$ cm. We would like to look

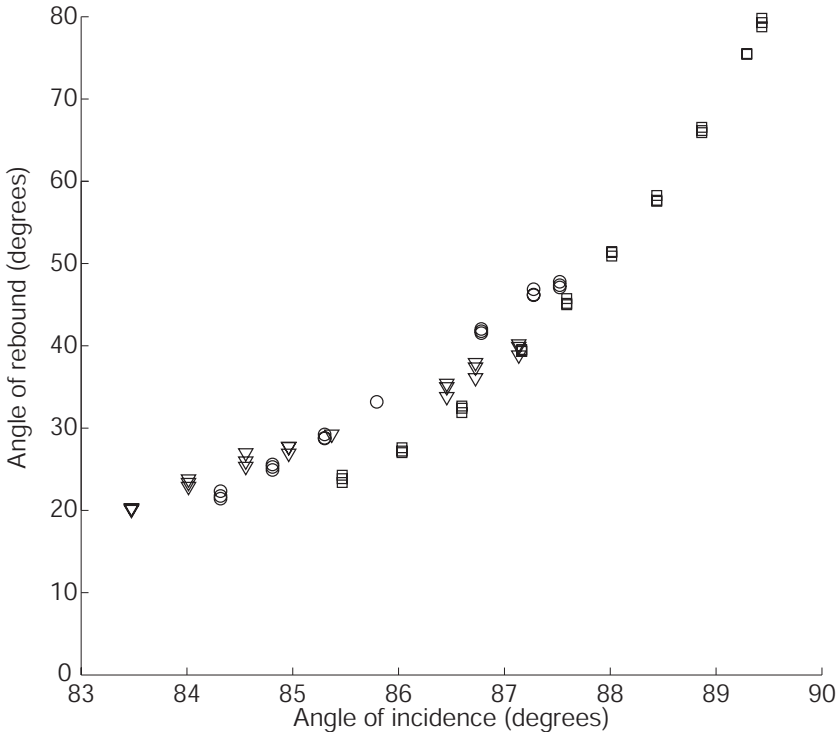

Figure 6.4: The dependence of the jet's angle of rebound θ_r as a function of the jet's angle of incidence θ_i for $Q = 0.18$ cm^3/s ($\square$), 0.36 cm^3/s ($\circ$), 0.54 cm^3/s ($\bigtriangledown$). Parameters: $\mu = 349$ mPa s, $H = 3.0$ cm, and $V_{bath} = 0.66 - 7.87$ cm/s.

at two effects, how the angle of incidence changes the angle of rebound and how much energy is lost during the rebound process. We can define a velocity of incidence V_i and an angle of incidence θ_i as

$$V_i = \sqrt{(V_{jet}^2 + V_{bath}^2)} \tag{6.4}$$

$$\theta_i = tan^{-1}(V_{jet}/V_{bath}). \tag{6.5}$$

Before we can discuss how the angle of incidence θ_i affects the measured angle of rebound θ_m, we must transform the angle of rebound into the same moving frame as the angle of incidence, which is accomplished by

$$\theta_r = tan^{-1}\left(\frac{V_m sin\theta_m}{V_{bath} + V_m cos\theta_m}\right), \tag{6.6}$$

where V_m is the velocity of rebound measured in the lab frame and θ_r is the angle of rebound in the frame moving with the bath velocity V_{bath}. Similarly, the velocity can be transformed

$$V_r = \sqrt{V_m^2 sin^2\theta_m + [V_m cos\theta_m + V_{bath}]^2}, \tag{6.7}$$

where V_r is the velocity of rebound measured in the moving frame. Finally, we can calculate the fraction of the initial energy lost during the bounce to be

$$(V_i^2 - V_r^2)/V_r^2. \tag{6.8}$$

Figure 6.4 shows the dependence of the angle of rebound θ_r on the angle of incidence θ_i. The different curves are for different flow rates. The general trend is that the jet rebounds at a steeper angle for angles of incidence closer

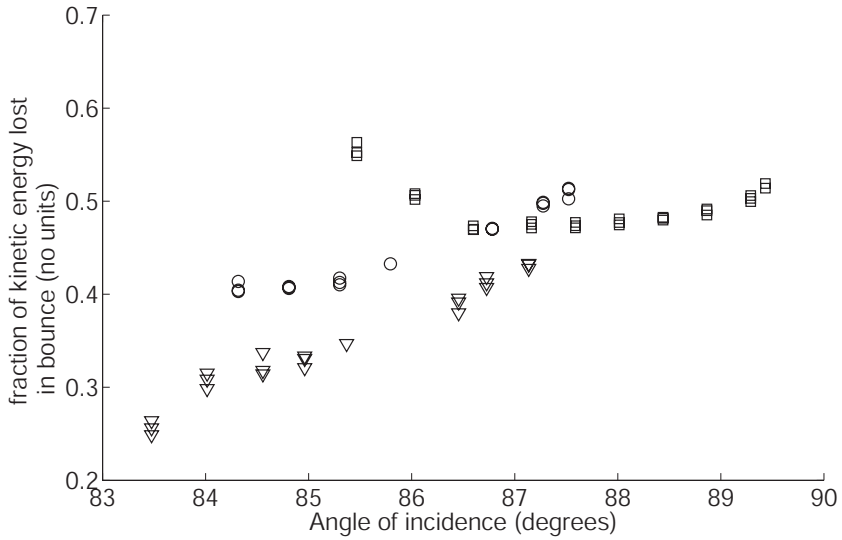

Figure 6.5: The fraction of the jet's initial kinetic energy lost during rebound for $Q = 0.18$ cm^3/s ($\square$), 0.36 cm^3/s ($\circ$), 0.54 cm^3/s ($\bigtriangledown$). Parameters: $\mu =$ 349 mPa s, $H = 3.0$ cm, and $V_{bath} = 0.66 - 7.87$ cm/s.

to normal incidence. It is interesting to note that small changes in the angle of incidence changes the angle of rebound greatly.

Figure 6.5 shows the fraction of the jet's initial kinetic energy lost during the rebound as a function of the angle of incidence. Again, the different curves are for data taken at different flow rates Q. The general trend is that more energy is lost the closer to normal that the jet is incident. Data for the energy lost at different viscosities is not available, but the same general trend was observed. When changing the fluid viscosity, the size of the semicircular indentation that the jet makes in the surface decreases with increasing viscosity. Thus, more viscous jets rebound with more of their original velocity.

The angle of the jet emerging from the nozzle is a parameter that was not varied in our experiments but would be useful in understanding the bouncing jet. Mei Yi Cheung performed such experiments as part of her International Baccalaureate program at the United Nations International School in New York City [24]. Anaëlle Hallé and David Quéré at Ecole Supérieure de Physique et de Chimie Industrielles (ESPCI, Paris) also conducted experiments varying the jet's collision angle [51].

6.3 Air layer confirmation

The presence of the air layer was confirmed experimentally by two methods. The first confirmation came from observations that the air layer will pinch into bubbles while the jet is impinging into the bath and entraining air. The second confirmation came from observations that the transition from entraining (with bubbles produced) to bouncing by increasing bath velocity when the jet is in the half-entraining state [136]. Another simple visual experiment would be to add dye to the falling jet.

The many experiments which have been done on bouncing and floating drops of fluid [60, 63, 83, 110, 112, 113, 143] can inform our understanding of the bouncing jet. For example, C.V. Boys popularized Lord Rayleigh's work on the collision of two water jets in midair [17]. Rayleigh knew then that the bounce was a "question of ... air .. [being] squeezed out during ... [the] collision" as he experimented with atmospheres of different gases, observed the absence of any electrical contact between the rebounding jets, and knew

to make sure that the water surfaces were very clean [110–112]. Mahajan furthered the studies by replacing the surrounding air with other gases and observed the effect on noncoalescing drops [83]. Similar experiments could be done with the bouncing jet by replacing the air with another fluid, such as water, helium (by putting the experiment in a balloon), carbon dioxide (No balloon is needed since carbon dioxide is more dense than air.), or SF_6. This would allow the density and viscosity of the surrounding medium to be varied considerably.

Another experiment that could shed light on the role of the air lubrication layer would be to change the pressure of the surrounding air. Vetrano and Dell'Aversana built an experiment contained in a vacuum chamber from which the air could be pumped out [143]. For a pendant drop suspended above a moving solid surface, they observed that the shape of the film did not change significantly if the ambient pressure of the surrounding air was at least 0.3 to 0.4 atm.

6.4 Lubrication theory

We present now an approximate calculation of the air film thickness, based on lubrication theory. The film thickness can be estimated by balancing the air squeezed out and the air drawn into the gap by the motion of the jet and bath. This mechanism was originally suggested by a Referee of our *Physical Review E* article [136]. A more rigorous derivation is needed if we are to arrive at a publishable conclusion. While this is an interesting and feasible

task, it will be left for a careful execution and experimental check at some later time. This calculation serves as only a demonstration of the complicated dependencies that arise in the bouncing jet phenomenon. We have found that simple relationships between parameters are very rare in this experiment.

Following Dorbolo *et al.* [34], the simplified Navier-Stokes for a uniform, narrow gap of thickness ϵ is

$$\frac{\partial p}{\partial x} = \mu_{air} \frac{\partial^2 v}{\partial z^2}, \tag{6.9}$$

where $v(z)$ is the velocity of the air, p is the pressure, μ_{air} is the air viscosity, x is along the gap and z is across it. With the bath surface moving at $v(z = 0) = V_{bath}$ and the jet moving at $v(z = \epsilon) = V_{jet}$, the velocity averaged over the gap is

$$< v >= -\frac{\partial p}{\partial x} \frac{\epsilon^2}{12\mu_{air}} + \frac{V_{jet} + V_{bath}}{2}. \tag{6.10}$$

In this very simple estimation, the pressure term accounts for the air squeezed out from the gap and the velocity term accounts for the air coming into the gap. The transition between a steady gap and a shrinking gap is when the average velocity $< v >$ is zero

$$\frac{\partial p}{\partial x} \frac{\epsilon^2}{12\mu_{air}} = \frac{V_{jet} + V_{bath}}{2}. \tag{6.11}$$

We can calculate the pressure gradient from the forces pushing the gap together, which are already estimated at the end of Section IIIA of our paper

as [136]

$$F_I \approx \rho\pi(d_{jet}/2)^2 V_{jet}^2(1 + sin\theta_m) \tag{6.12}$$

$$F_S \approx 2\sigma\ell, \tag{6.13}$$

where F_I is the force due to the change of momentum of the jet, F_S is the force due to the surface tension, ρ is the density of the liquid, and θ_m is the rebound angle of the jet measured in the lab frame. To get the pressure gradient, we assume that the pressure drop occurs across half of a jet diameter d_{jet} (assuming air is squeezed out to the side of the jet) and that the forces are distributed over the area $d_{jet}S$, where S is the semicircular length that the jet and the bath are in contact. The pressure gradient is then

$$\frac{\partial p}{\partial x} = 2\frac{(F_S + F_I)}{d_{jet}^2 S} = \frac{\rho\pi}{2S}V_{jet}^2(1 + sin\theta_m) + \frac{4\sigma}{d_{jet}^2}. \tag{6.14}$$

Using $Q = \pi d_{jet}^2 V_{jet}/4$ and $S = bQ$ (an empirical relation where $b = 3.13$ s/cm^2 is determined from measurements [136]), this can also be written as

$$\frac{\partial p}{\partial x} = \frac{\rho\pi}{2bQ}V_{jet}^2(1 + sin\theta_m) + \frac{\pi\sigma V_{jet}}{Q}. \tag{6.15}$$

Now the only unknown in (6.11) is the gap thickness ϵ. We can solve for the gap thickness

$$\epsilon^2 = 12\mu_{air}\frac{V_{jet} + V_{bath}}{2}\left(\frac{\rho\pi V_{jet}^2(1 + sin\theta_m)}{2bQ} + \frac{\pi\sigma V_{jet}}{Q}\right)^{-1}. \tag{6.16}$$

Only Q, μ_{air}, and V_{bath} are varied experimentally. The quantities ρ, σ, and V_{jet} are nearly constant. The angle θ_m was not measured systematically; for

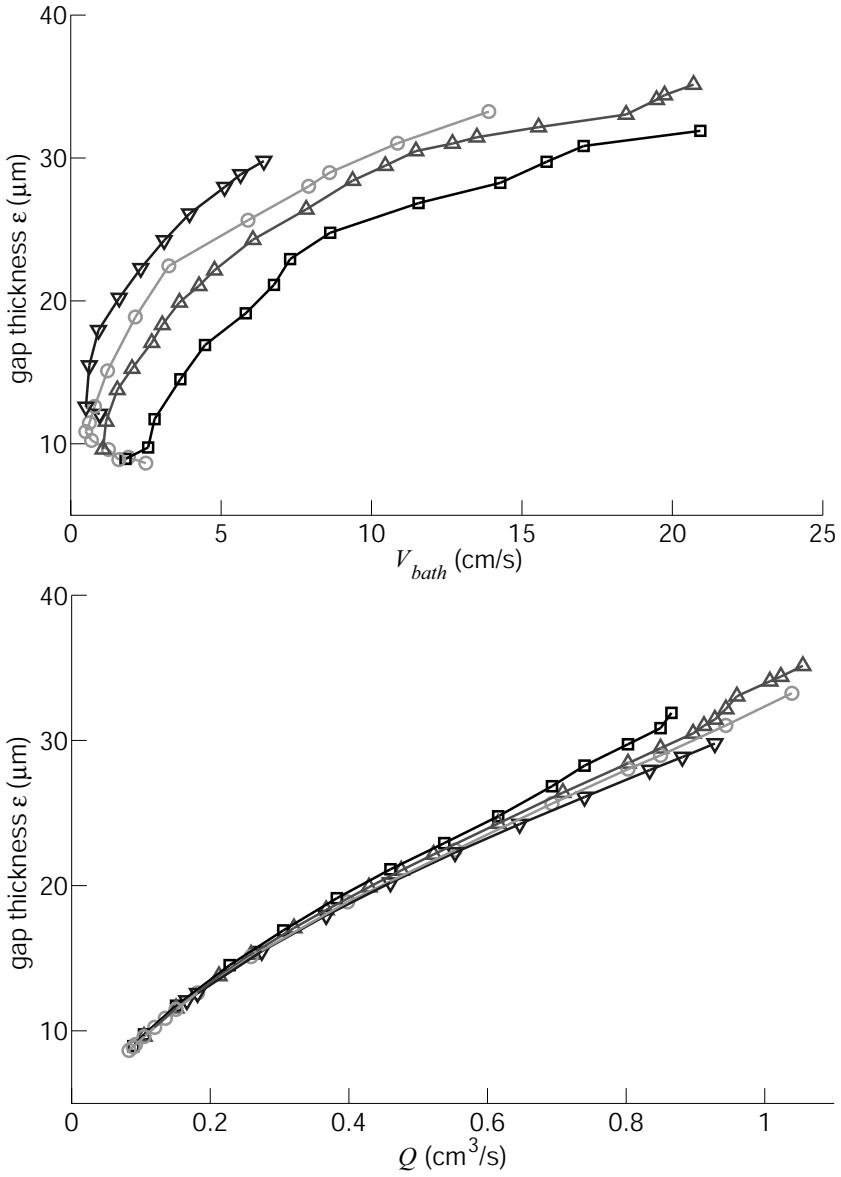

Figure 6.6: The gap thickness calculated from (6.16) using the transition curves between non-bouncing and bouncing states from Fig. 5 of [136]. Viscosity values $\mu = 53$ ($\square$), 102 ($\triangle$), 211 ($\circ$), and 349 mPa s ($\triangledown$).

simplicity we assume θ_m=90°. We can compute the gap thickness using the parameters at the transition between non-bouncing and bouncing states from Fig. 5 of our *Physical Review E* paper [136] (Fig. 6.6). Qualitatively the plots in Fig. 6.6 make sense. For larger V_{bath} the gap thickness grows as more air is pulled into the gap. For larger Q the gap thickness shrinks as the larger force squeezes more air out. However, this expression for the thickness does not collapse the transition curves. Quantitatively the gap thicknesses (computed here to be 10 to 30 μm) are larger than would be expected from previous work (0.1 to 10 μm) [60, 81, 143], but the rough agreement between our expectations and the model suggests that the air budget is a promising mechanism. It should be noted that this argument has not been confirmed and is just one mechanism of many possibilities.

6.5 Improving the methods

There are many possibilities for extensions of this work. Some have been discussed in Section VI of our paper [136].

A curious phenomenon that was observed resembled a fluid trampoline. If the flow rate of the bouncing stream abruptly goes to zero, the last bit of jet is thrown farther than the steady bouncing jet. It seems plausible that since the jet is no longer maintaining the indentation on the surface, the end of the jet absorbs some of the energy stored in the indentation as it springs back to the bath level. This propels the end of the jet much farther than the jet ordinarily bounces.

There were many small details that, if we had the experiments to do over again, would be done differently. For instance, the bath's interface pinned on edge of the inner cylinder, because this edge was machined rather sharp. The inner cylinder set the height of the bath, so the height of the surface relative to the jet nozzle would fluctuate as the fluid repeatedly built up enough height to spill over the edge of the inner cylinder into the reservoir. If the inside edge was rounded, the surface pinning would be avoided and the bath level would stay more constant.

A very productive next step would be to vary the velocity and diameter of the jet independently. By varying the flow rate as it was done in our experiments, the jet velocity and diameter could not be controlled easily. Moreover, the flow rate cannot be non-dimensionalized as meaningfully as the velocity and the diameter of the jet. The jet velocities in our experiments were known to about 8% and the velocity profiles within the jet were not known. This and the fact that most data was taken at the same height let us assume that the velocity of the jet was constant in our experiments, which was only an approximation. One way to measure the jet velocity profile is to track the motion of tracer particles in the falling jet. With the velocity and diameter of the jet known, one could begin to understand how different measurements of the bouncing jet behave as a function of the diameter of the jet.

All of our publishable data was taken at a single nozzle diameter. The nozzle was large and the fluid exited the large nozzle at a low velocity, which was beneficial for allowing the jet to fall from a fixed height with almost the

same velocity at different flow rates. But this precluded measuring how the jet bounces differently as the angle of incidence is varied in the lab frame.

In addition, several changes could be made to better image the bouncing jet. In our experiments all jets were seen through the wall of the acrylic tank, which introduced distortions and scattering. The walls of the cylinder could be cut shorter so that views to the top of the surface would be unimpeded, although the edge of the wall could make other problems. Another simple change would be to increase the contrast between the jet and the bath. This could be accomplished by having more homogeneous lighting and a more homogeneous background. Often the uneven reflective texture of the inner cylinder made interpreting the image more difficult. Aligning the camera carefully so that the camera could image above and below the surface simultaneously was useful, but was not practical in all cases, because of the meniscus and the change in the bath level due to the bath's changing rotation rate. Finally, the lighting used was continuous from two halogen bulbs, which would heat the bath. A strobe light synchronized with the still camera could spread the same intensity of light only when it was required and with only a fraction of the heat. Continuous lighting is probably still the easiest option for taking video because of synchronization issues.

Another improvement would be to measure the flow pattern in the bath with streak photography or particle image velocimetry using seed particles and laser sheets.

Finally, one unresolved puzzle has to do with the general need of a

perturbation to start the jet bouncing. The jet only starts to bounce spontaneously in specific situations (Sect. 1.7 and Fig. 1.6). This introduces an issue with the energy balance argument presented in our paper [136]. The jet does not start to bounce spontaneously once plunging becomes energetically unfavorable at all parameters, so why does the energy balance collapse the regime diagrams of Fig. 5 of [136]?

6.6 Image gallery

The bouncing jet has great visual appeal and some of the many behaviors are displayed in Figs. 6.7-6.13 below. To make the contour of the surface more visible, a polar grid was printed and laminated for the bottom of the bath's tank (Fig. 6.10). To capture these pictures, we used a Kodak Motion Corder Analyzer (Model SR-1000) and a Nikon D70 digital camera with a 50mm Macrolens. All but Fig. 6.12 were taken by Sunghwan Jung and me. Figure 6.12 was taken by Yee Kwong Pang.

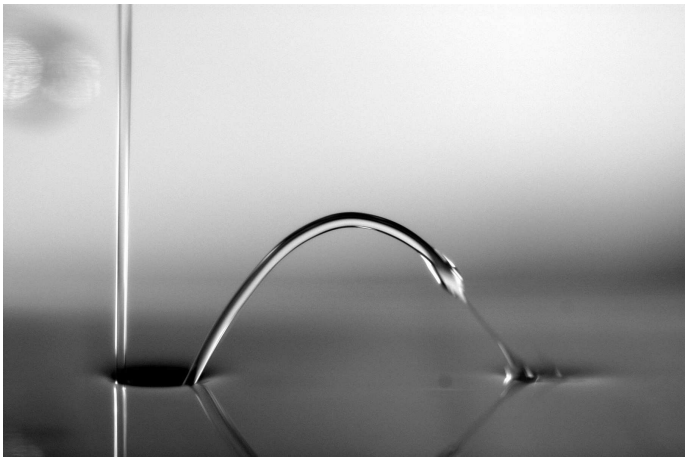

Figure 6.7: Rayleigh-Plateau instability occurring during the bounce. The field of view is 3 cm wide. Conditions: $\mu = 102$ mPa s, $Q = 0.23$ cm^3/s, $V_{bath} = 15.7$ cm/s, $H = 5.0$ cm.

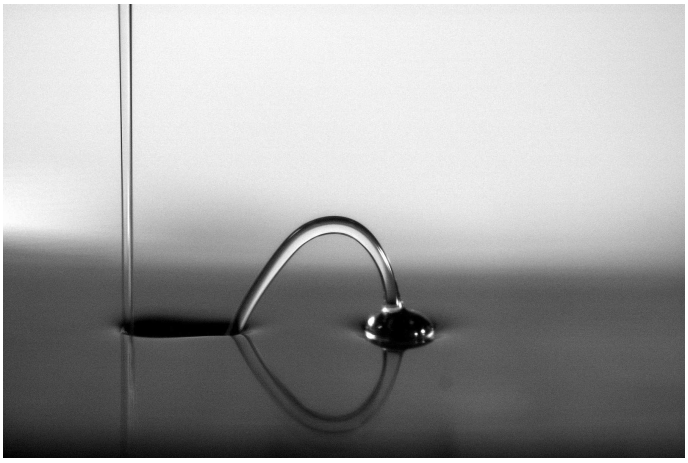

Figure 6.8: A jet floating after rebound. The field of view is 3 cm wide. Conditions: $\mu = 102$ mPa s, $Q = 0.35$ cm^3/s, $V_{bath} = 15.7$ cm/s, $H = 5.0$ cm.

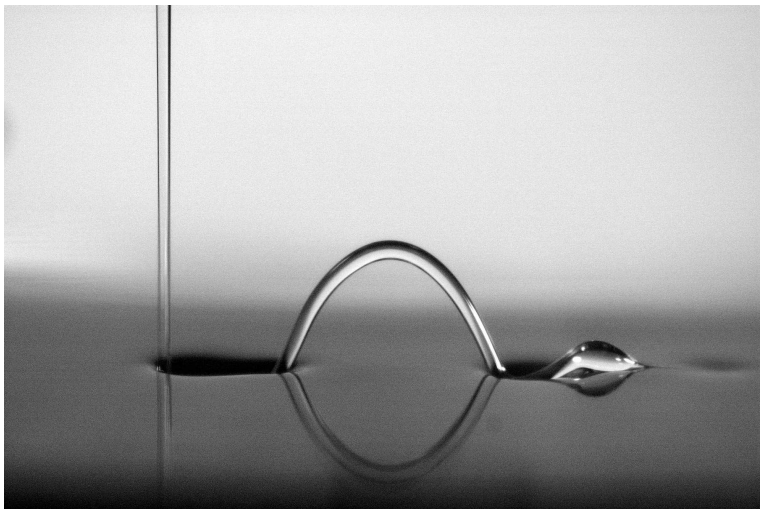

Figure 6.9: A jet bouncing twice with a blub of fluid on surface. This image was taken after a drop of fluid pinched off from the jet and merged with the bath, which created the indentation to the far right. The field of view is 3 cm wide. Conditions: $\mu = 102$ mPa s, $Q = 0.35$ cm^3/s, $V_{bath} = 15.7$ cm/s, $H = 5.0$ cm.

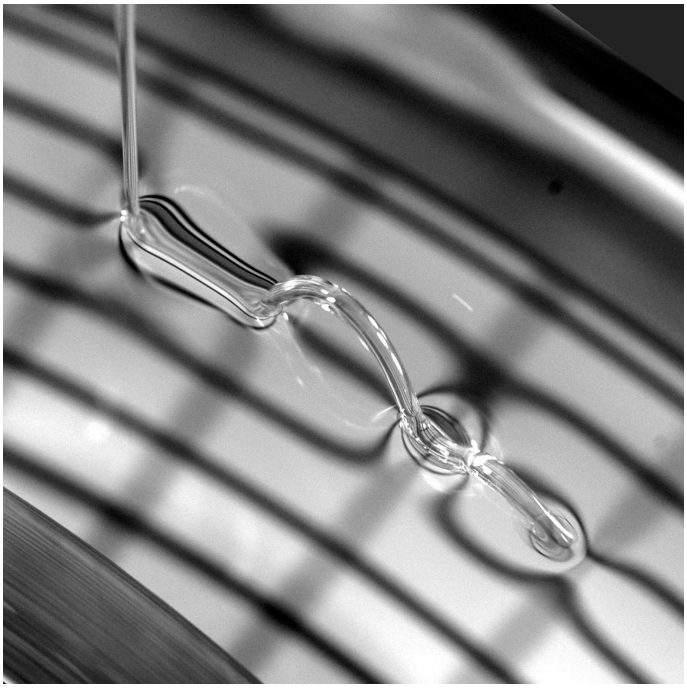

Figure 6.10: A view of the double bouncing jet from above against the background of the grid on the bottom of the tank, which accents the shape of the interface. The field of view is 4.3 cm wide. Conditions: $\mu = 102$ mPa s, $Q = 0.44$ cm^3/s, $V_{bath} = 15.7$ cm/s, $H = 5.0$ cm.

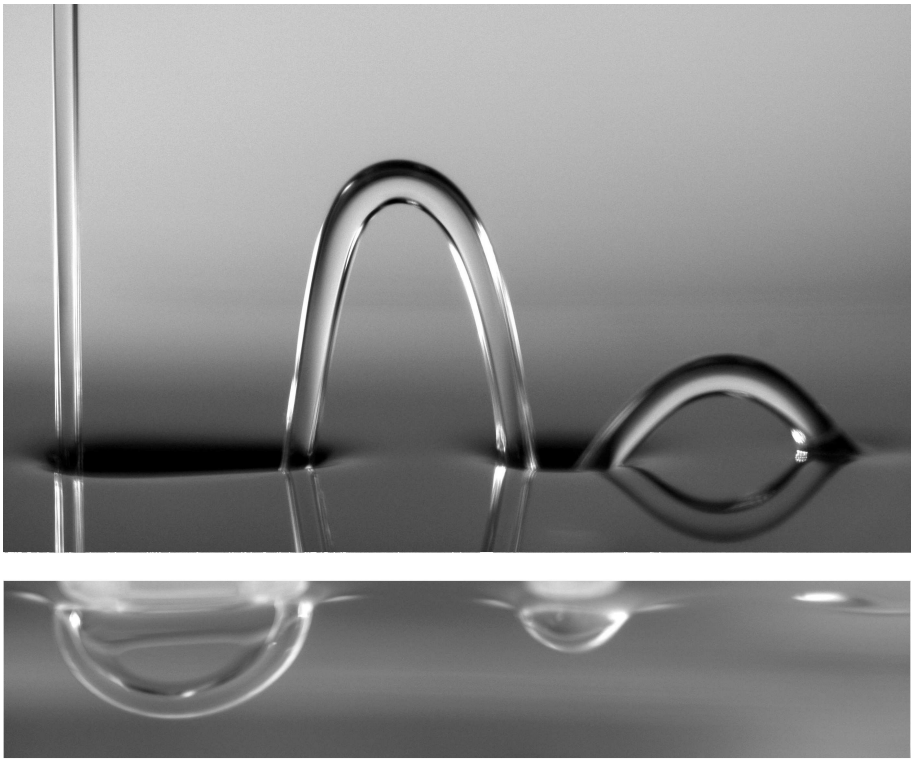

Figure 6.11: A view above and below the surface of a double bouncing jet while the bath velocity is low. The field of view is 3.3 cm wide. In both images, the bath surface extends back in perspective. Conditions: $\mu = 102$ mPa s, $Q = 0.35$ cm^3/s, $V_{bath} = 11.0$ cm/s, $H = 5.0$ cm.

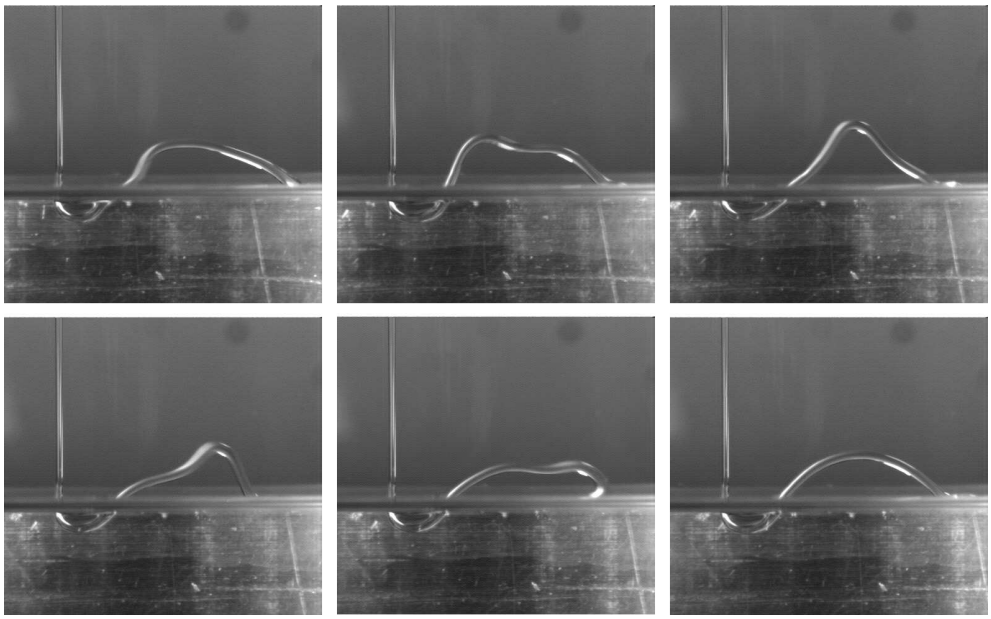

Figure 6.12: An irregularity in the falling jet has perturbed the bouncing jet in its trajectory. The irregularity passes and the bouncing jet returns to a nearly parabolic flight. The relative times of the images are 0, 0.04, 0.08, 0.10, 0.12, 0.16 s going left to right in the first row then left to right in the second row. The field of view is 3.7 cm wide. Conditions: $\mu = 349$ mPa s, $Q = 0.36$ cm^3/s, $V_{bath} = 4.9$ cm/s, $H = 4.2$ cm.

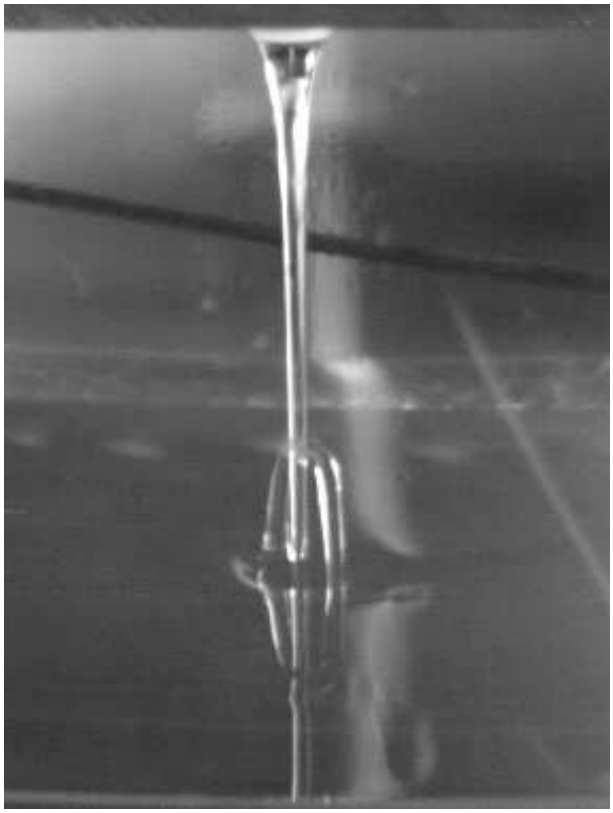

Figure 6.13: A jet bouncing opposite to the direction of the bath velocity. The bath is traveling slowly from left to right and the indentation in the surface is deep, pushing the jet opposite to the bath velocity. The rebounding jet emerges traveling upward on the right side of the stream. It bounces to the inside and lands in front of the stream. The lower edge of the white nozzle is visible in the top of the image; the jet falls 3.0 cm to the surface. Conditions: $\mu = 515$ mPa s, $Q = 0.6$ cm^3/s, $V_{bath} = 0.65$ cm/s, and $H = 3.0$ cm.

Chapter 7

Concluding remarks

Unstable interfaces produce a variety of shapes, depending on the conditions of growth and the underlying physical process. In the preceding chapters, we told about the research done on five instabilities involving viscous fingering, diffusion-limited aggregation (DLA), pinch-off, and bouncing jets. In these concluding remarks, we review what we learned that was already known, what we learned that was new, and why this work matters.

For the fjords of viscous fingering, we found the first new selection rules since the original Saffman and Taylor paper in 1958 [121] (Chapter 2). The selection rules pertain to the secondary tip-splitting instability.[1] Relative to the fingers of viscous fingering, the fjords have been neglected, so that it was for the fjords that we looked for two new rules. We found that the fjord base width was one-half of the most unstable wavelength at the time of the fjord's birth, which we defined as the moment that the curvature was zero for the piece of interface that would evolve to be the fjord's base. We also also found that the opening angle of fjords was $8.0^\circ \pm 1.0^\circ$ for a large range of viscosities,

[1]The distinction between the primary and secondary instability is historical and not entirely warranted. The primary Saffman-Taylor instability can be viewed as fjords pinned at the corners of the Hele-Shaw cell.

forcing, fjord length, and other experimental parameters. We propose that these two selection rules are fundamental to the preservation of the fractal dimension for viscous fingering patterns grown under different conditions. As the forcing increases the fjord base widths decrease and the fjord opening angles stay the same, which is similar to simply changing the spatial scale of the pattern. Looking at viscous fingering from the perspective that the fjords are the constituents of the patterns offers a challenge for theorists to find the source of the nearly invariant 8° opening angle, and a challenge for experimentalists to find the corresponding selection rules for other unstable systems. The first place to look would be other physical systems which approximate Laplacian growth with isotropic surface forces.

Previous to our work, Bouchbinder *et al.* developed methods to construct the conformal map from the unit circle to a complicated interface [16]. We had also taken fresh experimental data for complicated viscous fingering patterns. We combined the newest analytic tools with the newest data to help answer the question of whether or not viscous fingering and DLA produced quantitatively similar patterns (Chapter 3). In the process, we not only remeasured the fractal dimension of both patterns, but we also calculated that DLA and viscous fingering have the same $f(\alpha)$ spectrum of singularities within measurement uncertainty. The $f(\alpha)$ spectrum is a global measure of the growth dynamics and the geometry of the patterns. Since the two spectra are the same, we say that the two processes are in the same scaling universality class. This adds evidence to the argument that DLA and viscous fingering patterns

stem from the same underlying growth class. The hope is that more systems can be added to this class and that we can approach a unified foundation of how unstable systems grow and what mechanisms give them their properties. We also show preliminary data that the boundary conditions of viscous fingering growth patterns change the exponent of the power-law scaling of the area with perimeter, which could help to resolve reports of different scalings in the literature.

With this same goal of unification, we performed the first experimental test of harmonic moments as a special mathematical representation of Laplacian growth (Chapter 4). Harmonic moments have been known to be conserved quantities theoretically for almost 15 years [94]. However we found with the introduction of surface tension into the problem, the harmonic moments are no longer conserved and the moments decay at a specific rate. We observed that the predicted decay of the moments in experiments of growing viscous fingering patterns was accurate to within our 16% uncertainty. Because the moments decay as expected with non-zero surface tension, our experiments provide evidence that the moments would be conserved in growth with zero surface tension. This representation of harmonic moments should apply to any system undergoing Laplacian growth. Like the scaling universality class, the harmonic moments can bring us closer to unifying unstable, non-equilibrium systems. In the process of these experiments, we developed a clever application of Bataille's formula for the most unstable wavelength of an interface [7], which enabled us to grow nearly symmetric bubbles with an almost monochromatic

perturbation of a chosen moment number.

The first studies on pinch-off processes were concerned with capillary pinch-off of a fluid thread [37]. Now a trend is to study the singularity of the pinch-off event [152]. The goal is to develop integrable hierarchies and functional forms for describing nonlinear dynamics. We experimentally tested two such predictions for viscous fluids in a Hele-Shaw cell (Chapter 5):

1. Richardson predicted that two oil domains under the correct conditions can pass through each other without changing shape [115, 116].

2. Lee *et al.* predicted that for a bubble of air breaking into two bubbles, the shape near pinch-off will be self-similar and independent of the global shape of the air bubble [76].

However, while the theory is two-dimensional, we could not avoid fully three-dimensional pinch-off. The shape of interface depends on whether surface tension or viscous effects dominate. To experiment on this instability, the conditions must be very well controlled. The work presented on this problem is only preliminary.

The crucial importance of thin lubricating layers in stabilizing the non-coalescence of drops and streams of liquid has been known for over one hundred years [110]. These bouncing and floating drops and jet have been observed in Newtonian and non-Newtonian liquids [98, 143]. Adding to this body of knowledge, we have discovered that a Newtonian liquid stream can rebound from

the free surface of a moving bath (Chapter 6). The mechanism of bouncing was identified as a thin layer of lubricating air replenished by the relative motion of the jet and the bath. We measured the conditions necessary for the phenomenon to occur by varying three parameters: viscosity, bath velocity, and jet flow rate. Using these data, we presented evidence that an energy balance defines the transition curve between non-bouncing and bouncing states. Bouncing jets can be used as a method to control air entrainment, a method to control the attachment of a liquid stream to a substrate, an example of fluid flow with multiple steady states for the same parameters, and an example of steady non-coalescence.

The work presented in this dissertation was as much about developing and proving the techniques used to study the phenomena as understanding the phenomena themselves. The theme has been to distinguish what influences the patterns by observing their evolution. The overall goal has been to categorize the nature of the growth processes as being the same or different from other physical phenomena. If first we can identify classes of universal behavior, then it might be possible for the work of building a unified framework to understand nonlinear processes to begin.

Bibliography

[1] D. G. A. L. Aarts, H. N. W. Lekkerkerker, H. Guo, G. H. Wegdam, and D. Bonn. Hydrodynamics of droplet coalescence. *Physical Review Letters*, **95**:164503, 2005.

[2] O. Agam, E. Bettelheim, P. Wiegmann, and A. Zabrodin. Viscous fingering and the shape of an electronic droplet in the quantum Hall regime. *Physical Review Letters*, **88**:236801, 2002.

[3] E. Alvarez-Lacalle, J. Ortin, and J. Casademunt. Relevance of dynamic wetting in viscous fingering patterns. *Physical Review E*, **74**:025302, 2006.

[4] A. Arneodo, J. Elezgaray, M. Tabard, and F. Tallet. Statistical analysis of off-lattice diffusion-limited aggregates in channel and sector geometries. *Physical Review E*, **53**:6200, 1996.

[5] G. A. Baker. *Pade Approximants*. Cambridge University Press, 1996.

[6] F. Barra, B. Davidovitch, and I. Procaccia. Iterated conformal dynamics and Laplacian growth. *Physical Review E*, **65**:046144, 2002.

[7] J. Bataille. Stabilité d'un écoulement radial non miscible. *Revue de l'Institut Français du Pétrole et Annales des Combustibles Liquides*, **23**:1349, 1968.

[8] E. Ben-Jacob. From snowflake formation to growth of bacterial colonies.II. Cooperative formation of complex colonial patterns. *Contemporary Physics*, **38**:205, 1997.

[9] E. Ben-Jacob, G. Deutscher, P. Garik, N. D. Goldenfeld, and Y. Lareah. Formation of a dense branching morphology in interfacial growth. *Physical Review Letters*, **57**:1903, 1986. `http://link.aps.org/abstract/PRL/v57/p1903`.

[10] E. Ben-Jacob, R. Godbey, N. D. Goldenfeld, J. Koplik, H. Levine, T. Mueller, and L. M. Sander. Experimental demonstration of the role of anisotropy in interfacial pattern formation. *Physical Review Letters*, **55**:1315, 1985.

[11] D. Bensimon, L. P. Kadanoff, S. Liang, B. I. Shraiman, and C. Tang. Viscous flows in two dimensions. *Reviews of Modern Physics*, **58**:977, 1986.

[12] R. Bergmann, D. van der Meer, M. Stijnman, M. Sandtke, A. Prosperetti, and D. Lohse. Giant bubble pinch-off. *Physical Review Letters*, **96**:154505, 2006.

[13] A. K. Biń. Gas entrainment by plunging liquid jets. *Chemical Engineering Science*, **48**:3585, 1993.

[14] U. Bisang and J. H. Bilgram. Shape of the tip and the formation of sidebranches of xenon dendrites. *Physical Review E*, **54**:5309, 1996.

[15] V. A. Bogoyavlenskiy. Bridge from diffusion-limited aggregation to the Saffman-Taylor problem. *Physical Review E*, **63**:045305, 2001.

[16] E. Bouchbinder, J. Mathiesen, and I. Procaccia. Stress field around arbitrarily shaped cracks in two-dimensional elastic materials. *Physical Review E*, **69**:026127, 2004.

[17] C. V. Boys. *Soap-Bubbles: Their Colours and the Forces Which Mold Them*. Society for Promoting Christian Knowledge, London, 1912.

[18] A. Buka and P. Palffy-Muhoray. Stability of viscous fingering patterns in liquid crystals. *Physical Review A*, **36**:1527, 1987.

[19] A. Buka, P. Palffy-Muhoray, and Z. Rácz. Viscous fingering in liquid crystals. *Physical Review A*, **36**:3984, 1987.

[20] J. C. Burton, R. Waldrep, and P. Taborek. Scaling and instabilities in bubble pinch-off. *Physical Review Letters*, **94**:184502, 2005.

[21] B. Campbell. *Break-off of an air bubble within a thin oil layer*. Undergraduate Honors Thesis. University of Texas at Austin, May 2007.

[22] J. Casademunt. Viscous fingering as a paradigm of interfacial pattern formation: Recent results and new challenges. *Chaos*, **14**:809, 2004.

[23] S. C. Case and S. R. Nagel. Coalescence in low-viscosity liquids. page arXiv:0709.1496, 2007.

[24] M. Y. Cheung. The effect of the angle of incidence of an impinging Newtonian fluid jet on its ability to bounce off a moving bath of the same fluid. *(unpublished)*, United Nations International School in New York City, USA, 2007.

[25] A. Chhabra and R. V. Jensen. Direct determination of the $f(\alpha)$ singularity spectrum. *Physical Review Letters*, **62**:1327, 1989.

[26] S. Ciliberto and J. P. Gollub. Pattern competition leads to chaos. *Physical Review Letters*, **52**:922, 1984.

[27] I. Cohen, M. P. Brenner, J. Eggers, and S. R. Nagel. Two fluid drop snap-off problem: Experiments and theory. *Physical Review Letters*, **83**:1147, 1999.

[28] Y. Couder. Viscous fingering as an archetype for growth patterns. In G. K. Batchelor, H. K. Moffatt, and M. G. Worster, editors, *Perspectives in Fluid Dynamics*, page 53. Cambridge University Press, 2000.

[29] M. C. Cross and P. C. Hohenberg. Pattern-formation outside of equilibrium. *Review of Modern Physics*, **65**:851, 1993.

[30] D. G. Crowdy. A note on viscous sintering and quadrature identities. *European Journal of Applied Mathematics*, **10**:623, 1999.

[31] S. R. P. da Rocha, K. L. Harrison, and K. P. Johnston. Effect of surfactants on the interfacial tension and emulsion formation between water and carbon dioxide. *Langmuir*, **15**:419, 1999.

[32] G. Daccord. Chemical dissolution of a porous medium by a reactive fluid. *Physical Review Letters*, **58**:479, 1987.

[33] C. Domb and J. L. Lebowitz, editors. *Phase Transitions and Critical Phenomena*, volume 12, New York, 1988. Academic Press.

[34] S. Dorbolo, E. Reysaat, N. Vandewalle, and D. Quéré. Aging of an antibubble. *Europhysics Letters*, **69**:966, 2005.

[35] P. Doshi, I. Cohen, W. W. Zhang, M. Siegel, P. Howell, O. A. Basaran, and S. R. Nagel. Persistence of memory in drop breakup: The breakdown of universality. *Science*, **302**:1185–1188, 2003.

[36] U. Ebert, C. Montijn, T. M. P. Briels, W. Hundsdorfer, B. Meulenbroek, A. Rocco, and E. M. van Veldhuizen. The multiscale nature of streamers. *Plasma Sources Science Technology*, **15**:118, 2006.

[37] J. Eggers. Nonlinear dynamics and breakup of free-surface flows. *Review of Modern Physics*, **69**:865, 1997.

[38] J. Eggers. Coalescence of spheres by surface diffusion. *Physical Review Letters*, **80**:2634, 1998.

[39] J. Eggers. Air entrainment through free-surface cusps. *Physical Review Letters*, **86**:4290, 2001.

[40] J. Eggers, J. R. Lister, and H. A. Stone. Coalescence of liquid drops. *Journal of Fluid Mechanics*, **401**:293, 1999.

[41] W. T. Elam, S. A. Wolf, J. Sprague, D. U. Gubser, D. Van Vechten, G. L. Barz, and P. Meakin. Fractal aggregates in sputter-deposited $NbGe_2$ films. *Physical Review Letters*, **54**:701, 1985.

[42] P. Etingof and A. Varchenko. *Why the Droplet of fourth order remains to be of the fourth order?*, volume 18. American Mathematical Society, Providence RI, 1992.

[43] P. Fast and M. J. Shelley. Moore's law and the Saffman-Taylor instability. *Journal of Computational Physics*, **212**:1, 2006.

[44] C. Flament, G. Pacitto, J.-C. Bacri, I. Drikis, and A. Cebers. Viscous fingering in a magnetic fluid. I. Radial Hele-Shaw flow. *Physics of Fluids*, **10**:2464, 1998.

[45] H. Fujikawa and M. Matsushita. Fractal growth of *Bacillus subtilis* on agar plates. *Journal of the Physical Society of Japan*, **58**:3875, 1989.

[46] R. W. Giannetta and H. Ikezi. Nonlinear deformation of the electron-charged surface of liquid ^{4}He. *Physical Review Letters*, **47**:849, 1981.

[47] K. A. Gillow and S. D. Howison. A bibliography of free and moving boundary problems for Hele-Shaw and Stokes flow. `http://www.maths.ox.ac.uk/~howison/Hele-Shaw/` 1998.

[48] J. A. Glazier and A. Libchaber. Quasi-periodicity and dynamical systems: An experimentalist's view. *IEEE Transactions on Circuits and Systems*, **35**:790, 1988.

[49] J. P. Gollub and J. S. Langer. Pattern formation in nonequilibrium physics. *Reviews of Modern Physics*, **71**:S396, 1999.

[50] P. Grassberger, R. Badii, and A. Politi. Scaling laws for invariant measures on hyperbolic and non-hyperbolic attractors. *Journal of Statistical Physics*, **51**:135, 1988.

[51] A. Hallé and D. Quéré. Oblique impact of silicone onto silicone. *(unpublished)*, ESPCI (Paris), 2006.

[52] T. C. Halsey, M. H. Jensen, L. P. Kadanoff, I. Procaccia, and B. Shraimann. Fractal measures and their singularities: The characterization of strange sets. *Physical Review A*, **33**:1141, 1986.

[53] H. S. Hele-Shaw. On the motion of a viscous fluid between two parallel plates. *Transactions of the Royal Institute Naval Architects*, **40**:218, 1898.

[54] H. G. E. Hentschel and I. Procaccia. The infinite number of generalized dimensions of fractals and strange attractors. *Physica D*, **8**:435, 1983.

[55] A. Hernández-Machado, A. M. Lacasta, E. Mayoral, and E. Corvera Poiré. Phase-field model of Hele-Shaw flows in the high-viscosity contrast regime. *Physical Review E*, 68:046310, 2003.

[56] R. C. Hilborn. *Chaos and Nonlinear Dynamics*. Oxford University Press, second edition, 2003.

[57] G. M. Homsy. Viscous fingering in porous media. *Annual Review of Fluid Mechanics*, **19**:271, 1987.

[58] S. D. Howison. Cusp development in Hele-Shaw flow with a free surface. *SIAM Journal on Applied Mathematics*, **46**:20, 1986.

[59] R. Ishiguro, F. Graner, E. Rolley, and S. Balibar. Coalescence of crystalline drops. *Physical Review Letters*, **93**:235301, 2004.

[60] O. W. Jayaratne and B. J. Mason. The coalescence and bouncing of water drops at an air/water interface. *Proceedings of the Royal Society A*, **280**:545, 1964.

[61] M. H. Jensen, A. Levermann, J. Mathiesen, and I. Procaccia. Multifractal structure of the harmonic measure of diffusion-limited aggregates. *Physical Review E*, **65**:046109, 2002.

[62] W. Kang and U. Landman. Universality crossover of the pinch-off shape profiles of collapsing liquid nanobridges in vacuum and gaseous environments. *Physical Review Letters*, **98**:064504, 2007.

[63] M. Katalinić. Über die fl ussigkeitskügelchen, welche auf der oberfläche derselben flüssigkeit schwimmen. *Zeitschrift für Physik A*, 38:511, 1926.

[64] A. Kaye. A bouncing liquid stream. *Nature*, **197**:1001, 1963.

[65] N. C. Keim, P. Møller, W. W. Zhang, and S. R. Nagel. Breakup of air bubbles in water: Memory and breakdown of cylindrical symmetry. *Physical Review Letters*, **97**:144503, 2006.

[66] D. A. Kessler, J. Koplik, and H. Levine. Pattern selection in fingered growth phenomena. *Advances in Physics*, **37**:255, 1988.

[67] P. Kopczyński, W.-J. Rappel, and A. Karma. Cellular multiplets in directional solidification. *Physical Review E*, **55**:R1282, 1997.

[68] I. Krichever, M. Mineev-Weinstein, P. Wiegmann, and A. Zabrodin. Laplacian growth and Whitham equations of soliton theory. *Physica D*, **198**:1, 2004.

[69] A. Kuhn, F. Argoul, J. F. Muzy, and A. Arneodo. Structural analysis of electroless deposits in the diffusion-limited regime. *Physical Review Letters*, **73**:2998, Nov 1994.

[70] H. K. Kuiken. Viscous sintering: the surface-tension-driven flow of a liquid form under the influence of curvature gradients at its surface. *Journal of Fluid Mechanics*, **214**:503, 1990.

[71] L. W. Lake. *Enhanced Oil Recovery*. Prentice Hall, New Jersey, 1989.

[72] H. Lamb. *Hydrodynamics*. Cambridge University Press, 6th edition, 1932.

[73] L. Landau and B. Levich. Dragging of a liquid by a moving plate. *Acta Physicochimica U.R.S.S.*, **XVII**:42, 1942.

[74] J. S. Langer. Instabilities and pattern formation in crystal growth. *Reviews of Modern Physics*, **52**:1, 1980.

[75] J. S. Langer and H. Muller-Krumbhaar. Two-phase displacement in Hele Shaw Cells: Theory. *Acta Metallurgica*, 26:1681–1687, 1978.

[76] S.-Y. Lee, E. Bettelheim, and P. Wiegmann. Bubble break-off in Hele-Shaw flows: singularities and integrable structures. *Physica D*, **219**:22, 2006.

[77] R. Lenormand and C. Zarcone. Two-phase flow experiments in a two-dimensional permeable medium. *PhysicoChemical Hydrodynamics*, **6**:497, 1985.

[78] A. Lindner, D. Bonn, and J. Meunier. Viscous fingering in a shear-thinning fluid. *Physics of Fluids*, **12**:256, 2000.

[79] A. Lindner, D. Bonn, and J. Meunier. Viscous fingering in complex fluids. *Journal of Physics Condensed Matter*, **12**:477, 2000.

[80] M.-Q. Lòpez-Salvans, P. P. Trigueros, S. Vallmitjana, J. Claret, and F. Sagués. Fingerlike aggregates in thin-layer electrodeposition. *Physics Review Letters*, **76**:4062, 1996.

[81] É. Lorenceau, D. Quéré, and J. Eggers. Air entrainment by a viscous jet plunging into a bath. *Physical Review Letters*, **93**:254501, 2004.

[82] W. Losert, D. A. Stillman, H. Z. Cummins, P. Kopczyński, W.-J. Rappel, and A. Karma. Selection of doublet cellular patterns in directional solidification through spatially periodic perturbations. *Physical Review E*, **58**:7492, 1998.

[83] L. D. Mahajan. The effect of the surrounding medium on the life of floating drops. *Philosophical Magazine*, **10**:383, 1930.

[84] B. B. Mandelbrot. *The Fractal Geometry of Nature*. W. H. Freeman, New York, 1982.

[85] B. B. Mandelbrot and C. J. G. Evertsz. The potential distribution around growing clusters. *Nature*, **348**:143, 1990.

[86] J. Mathiesen, I. Procaccia, H. L. Swinney, and M. Thrasher. The universality class of diffusion limited aggregation and viscous fingering. *Europhysics Letters*, 72:257, 2006.

[87] K. V. McCloud and J. V. Maher. Experimental perturbations to Saffman-Taylor flow. *Physics Reports*, **260**:139, 1995.

[88] J. W. McLean and P. G. Saffman. The effect of surface tension on the shape of fingers in a Hele-Shaw cell. *Journal of Fluid Mechanics*, **102**:455, 1981.

[89] B. Meerson. Fluctuations provide strong selection in Ostwald ripening. *Physical Review E*, **60**:3072, 1999.

[90] B. Meulenbroek, U. Ebert, and L. Schafer. Regularization of moving boundaries in a Laplacian field by a mixed Dirichlet-Neumann boundary condition: Exact results. *Physical Review Letters*, **95**:195004, 2005.

[91] Y. Meyer and V. Salinger. *Wavelets and Operators*. Cambridge University Press, 2003.

[92] M. B. Mineev. Hele-Shaw flows with a free boundary produced by the injection of fluid into a narrow channel. *Physica D*, **43**:288, 1990.

[93] M. Mineev-Weinstein, P. Wiegmann, and A. Zabrodin. Integrable Structure of Interface Dynamics. *Physical Review Letters*, **84**:5106, 2000.

[94] M. B. Mineev-Weinstein. Multidimensional pattern formation has an infinite number of constants of motion. *Physical Review E*, **47**:2241, 1993.

[95] J. A. Miranda. Nonlinear effects due to gravity in a conical Hele-Shaw cell. *Physical Review E*, **65**:036310, 2002.

[96] M. G. Moore. *Unsteady Growth and Relaxation of Viscous Fingers*. Dissertation. The University of Texas at Austin, 2003.

[97] M. Murat. Dielectric breakdown between parallel plates. *Physical Review B*, **32**:8420, 1985.

[98] G. P. Neitzel and P. Dell'Aversana. Noncoalescence and nonwetting behavior of liquids. *Annual Review of Fluid Mechanics*, **34**:267, 2002.

[99] P. S. Novikoff. Two-phase displacement in Hele Shaw Cells: Theory. *Doklady Akademii Nauk USSR*, **18**:165, 1938.

[100] F. Parisio, F. Moraes, J. A. Miranda, and M. Widom. Saffman-Taylor problem on a sphere. *Physical Review E*, **63**:036307, 2001.

[101] C.-W. Park and G. M. Homsy. Two-phase displacement in Hele Shaw Cells: Theory. *Journal of Fluid Mechanics*, **139**:291, 1984.

[102] L. Paterson. Radial viscous fingering in a Hele Shaw cell. *Journal of Fluid Mechanics*, **113**:513, 1981.

[103] L. Paterson. The implications of fingering in underground hydrogen storage. *International Journal of Hydrogen Energy*, **8**:53, 1983.

[104] L. Paterson. Diffusion-limited aggregation and two-fluid displacements in porous media. *Physical Review Letters*, **52**:1621, 1984.

[105] L. Patrick, D. R. Hamilton, and W. J. Choyke. Growth, luminescence, selection rules, and lattice sums of SiC with Wurtzite structure. *Physical Review*, **143**:526, 1966.

[106] J. A. Pojman, C. Whitmore, M. L. T. Liveri, R. Lombardo, J. Marszalek, R. Parker, and B. Zoltowski. Evidence for the existence of an effective interfacial tension between miscible fluids: Isobutyric acid-water and 1-butanol-water in a spinning-drop tensiometer. *Langmuir*, **22**:2569, 2006.

[107] M.-N. Pons, E. M. Weisser, H. Vivier, and D. V. Boger. Characterization of viscous fingering in a radial Hele-Shaw cell by image analysis. *Experiments in Fluids*, **26**:153, 1999.

[108] O. Praud and H. L. Swinney. Fractal dimension and unscreened angles measured for radial viscous fingering. *Physical Review E*, **72**:011406, 2005.

[109] I. Procaccia. Personal communication, 2005.

[110] Lord Rayleigh. The influence of electricity on colliding water drops. *Proceedings of the Royal Society of London*, **28**:405, 1878-1879.

[111] Lord Rayleigh. Further observations upon liquid jets, in continuation of those recorded in the Royal Society's 'Proceedings' for March and May, 1879. *Proceedings of the Royal Society*, **34**, 1882-1883.

[112] Lord Rayleigh. Investigations in capillarity. *Philosophical Magazine*, **48**:321, 1899.

[113] O. Reynolds. On the floating of drops on the surface of water. *Proceedings of the Manchester Literary and Philosophical Society*, **21**, 1881-82.

[114] S. Richardson. Hele-Shaw flows with a free boundary produced by the injection of fluid into a narrow channel. *Journal of Fluid Mechanics*, **56**:609, 1972.

[115] S. Richardson. Hele-Shaw flows with free boundaries driven along infinite strips by a pressure difference. *European Journal of Applied Mathematics*, **7**:345, 1996.

[116] S. Richardson. Hele-Shaw flows with time-dependent free boundaries involving a concentric annulus. *Philosophical Transactions of the Royal Society of London A*, **354**:2513, 1996. Figure 8 used with permission in Sect. 5.4.

[117] L. Ristroph. *Fjord Geometry in Viscous Fingering.* Undergraduate Honors Thesis. The University of Texas at Austin, 2004.

[118] L. Ristroph, M. Thrasher, M. Mineev-Weinstein, and H. L. Swinney. Fjords in viscous fingering: selection of width and opening angle. *Physical Review E*, **74**:015201(R), 2006.

[119] K. J. Ruschak. *The Fluid Mechanics of Coating Flows.* Dissertation. University of Minnesota, 1974.

[120] P. G. Saffman. Viscous fingering in Hele-Shaw cells. *Journal of Fluid Mechanics*, **173**:73, 1986.

[121] P. G. Saffman and G. Taylor. The penetration of a fluid into a porous medium or Hele-Shaw cell containing a more viscous liquid. *Proceedings of the Royal Society of London. Series A*, **245**:312, 1958.

[122] J. J. Sakurai. *Modern Quantum Mechanics.* Addison Wesley (Boston, MA), 2nd edition, 1994.

[123] N. Samid-Merzel, S. G. Lipson, and D. S. Tannhauser. Pattern formation in drying water films. *Physica A*, **257**:413, 1998.

[124] S. K. Sarkar. Scaling dynamics of immiscible radial viscous fingering. *Physical Review Letters*, **65**:2680, 1990.

[125] Y. Sawada, A. Dougherty, and J. P. Gollub. Dendritic and fractal patterns in electrolytic metal deposits. *Physical Review Letters*, **56**:1260, 1986.

[126] H. Segur, S. Tanveer, and H. Levine, editors. *Asymptotics Beyond All Orders*, volume 284 of *NATO/ASI B: Physics*. NATO, Plenum Press, New York, 1991.

[127] B. K. Shivamoggi. *Theoretical Fluid Dynamics*. Wiley-Interscience, second edition, 1998.

[128] A. Sierou and J. R. Lister. Self-similar solutions for viscous capillary pinch-off. *Journal of Fluid Mechanics*, **497**:381, 2003.

[129] E. Somfai, R. C. Ball, J. P. DeVita, and L. M. Sander. Diffusion-limited aggregation in channel geometry. *Physical Review E*, **68**:020401, 2003.

[130] E. Somfai, L. M. Sander, and R. C. Ball. Scaling and crossovers in diffusion limited aggregation. *Physical Review Letters*, **83**:5523, 1999.

[131] P. Tabeling and A. Libchaber. Film draining and the Saffman-Taylor problem. *Physical Review A*, **33**:794, 1986.

[132] S. Tanveer. Surprises in viscous fingering. *Journal of Fluid Mechanics*, **409**:273, 2000.

[133] G. I. Taylor. Deposition of a viscous fluid on the wall of a tube. *Journal of Fluid Mechanics*, **10**:161, 1961.

[134] H. Thomé, M. Rabaud, V. Hakim, and Y. Couder. The Saffman-Taylor instability: From the linear to the circular geometry. *Physics of Fluids A*, **1**:224, 1989.

[135] M. Thrasher. *A Liquid Stream Bouncing off a Moving Liquid Bath*. Master's Thesis. The University of Texas at Austin, 2005.

[136] M. Thrasher, S. Jung, Y. K. Pang, C.-P. Chuu, and H. L. Swinney. Bouncing jet: A Newtonian liquid rebounding off a free surface. *Physical Review E*, 76, 2007.

[137] M. Thrasher, S. Jung, Y. K. Pang, and H. L. Swinney. Bouncing of a jet off a Newtonian liquid surface. *Physics of Fluids*, **19**:091110, 2007.

[138] B. Utter and E. Bodenschatz. Dynamics of low anisotropy morphologies in directional solidification. *Physical Review E*, **66**:051604, 2002. `http://link.aps.org/abstract/PRE/v66/e051604`.

[139] B. Utter, R. Ragnarsson, and E. Bodenschatz. Alternating tip splitting in directional solidification. *Physical Review Letters*, **86**:4604, 2001.

[140] D. Uy, M. Cordonnier, and T. Oka. Observation of ortho-para H_3^+ selection rules in plasma chemistry. *Physical Review Letters*, **78**:3844, 1997.

[141] V. K. Vanag and I. R. Epstein. Segmented spiral waves in a reaction-diffusion system. *Proceedings of the National Academy of Sciences*, **100**:14635, 2003.

[142] M. Versluis, C. Blom, D. van der Meer, K. van der Weele, and D. Lohse. Leaping shampoo and the stable Kaye effect. *Journal of Statistics Mechanics*, page P07007, 2006.

[143] M. R. Vetrano and P. Dell'Aversana. *Experiments on Air-Lubricated Liquids: Role of Vapor, Electrostatic Effects, and Heat Transmission across the Interface*, volume 628 of *Lecture Notes in Physics*. Springer Berlin, Heidelberg, 2003. online-only supplement.

[144] I. Visarath, L. Kocarev, T. L. Carroll, B. J. Gluckman, S. Boccaletti, and J. Kurths, editors. *Fluctuations and pinch-offs observed in viscous fingering*. Proceedings of the Seventh Experimental Chaos Conference 676, Springer-Verlag, 2003. also at cond-mat/0210307.

[145] J. R. Waggoner, V. J. Zapata, and L. W. Lake. Viscous mixing in unstable miscible displacements. *unpublished manuscript*.

[146] J. Wakita, I. Ráfols, H. Itoh, T. Matsuyama, and M. Matsushita. Experimental investigation on the formation of dense-branching-morphology-like colonies in bacteria. *Journal of the Physical Society of Japan*, **67**:3630, 1998.

[147] R. C. Weast, editor. *Handbook of Chemistry and Physics*. Chemical Rubber Co., Cleveland, Ohio, 1972-73.

[148] J. Wiggert and T. Maxworthy. Modal behavior observed in the evolution of immiscible interfaces within an injection-forced Hele-Shaw cell. *Physical Review E*, **47**:1931, 1993.

[149] T. A. Witten and L. Sander. Diffusion-limited aggregation, a kinetic critical phenomenon. *Physical Review Letters*, **47**:1400, 1981.

[150] C. Yeung and D. Jasnow. Dense-branching morphology and the radial Hele-Shaw cell driven at a constant flux. *Physical Review A*, **41**:891, 1990.

[151] M. Zeybek and Y. C. Yortsos. Parallel flow in Hele-Shaw cells. *Journal of Fluid Mechanics*, **241**:421, 1992.

[152] W. W. Zhang and J. R. Lister. Similarity solutions for capillary pinch-off in fluids of differing viscosity. *Physical Review Letters*, **83**:1151, 1999.

[153] H. Zhao and J. V. Maher. Associating-polymer effects in a Hele-Shaw experiment. *Physical Review E*, **47**:4278, 1993.

[154] O. Zik, Z. Olami, and E. Moses. Fingering instability in combustion. *Physical Review Letters*, **81**:3868, 1998.

[155] N. M. Zubarev. Exact solutions of the equations of motion of liquid helium with a charged free surface. *Journal of Experimental and Theoretical Physics*, **94**:534, 2002.

Vita

Matthew Evan Thrasher was born in Tulsa, Oklahoma on March 13, 1981, the second son of Thomas Stephen Thrasher and Cheryl Lea Thrasher. He attended school in Bartlesville, Oklahoma and at the Oklahoma School of Science and Mathematics in Oklahoma City. In June 2003, he earned the degree of Bachelor of Arts in Physics from Harvard College and started graduate studies at the University of Texas at Austin. In August 2005, he completed a Master of Arts degree in Physics with a thesis entitled "A Liquid Stream Bouncing off a Moving Liquid Bath."

Permanent address: 1640 W 6th St, Apt B, Austin, Texas 78703.
thrash@post.harvard.edu

This dissertation was typeset with LaTeX[†] by the author.

[†]LaTeX is a document preparation system developed by Leslie Lamport as a special version of Donald Knuth's TeX Program.